Energy Harvesting of Random Wide-band Vibrations with Applications to an Electro-Magnetic Rotational Energy Harvester

by

A Zachary Trimble

A.S., Weber State University (2001)
B.S., University of Utah (2005)
M.S., Massachusetts Institute of Technology (2007)

Submitted to the Department of Mechanical Engineering
in partial fulfillment of the requirements for the degree of

Doctor of Philosophy in Mechanical Engineering

at the

MASSACHUSETTS INSTITUTE OF TECHNOLOGY

June 2011

Author .....
Department of Mechanical Engineering
15 May 2011

Certified by .....
Alexander H. Slocum
Professor of Mechanical Engineering
Thesis Supervisor

Accepted by .....
David E. Hardt
Chairman, Department Committee on Graduate Theses

Energy Harvesting of Random Wide-band Vibrations with Applications to an Electro-Magnetic Rotational Energy Harvester

by

A Zachary Trimble

Submitted to the Department of Mechanical Engineering
on 15 May 2011, in partial fulfillment of the
requirements for the degree of
Doctor of Philosophy in Mechanical Engineering

Abstract

In general, vibration energy harvesting is the scavenging of ambient vibration by transduction of mechanical kinetic energy into electrical energy. Many mechanical or electro-mechanical systems produce mechanical vibrations. The kinetic energy associated with these mechanical vibrations represents a potential source of energy for sensors and other electronics. In fact, as the energy requirements for electronics and wireless communications systems has reduced, harvested energy from vibrations has been successfully used to power several wireless sensors. However, these sensors are implemented on systems with harmonic vibration sources. Most ambient vibrations are noisy, wide-band, and/or stochastic. As such, a resonant tuned-mass damper, with a narrow band-width, filters and discards much of the energy in the vibration spectrum, or worse, resonant harvesters will not resonate in stochastic environments.

Several solutions are commonly proposed for harvesting energy from wide-band excitations; multiple resonators tuned to different frequencies (farm systems), non-linear systems, input excitation rectification, and frequency tuning are the most common. This thesis addresses some of the wide-band and/or stochastic challenges to vibration energy harvesting by investigating vibration energy harvesting as a power source for sensors and communications in a down-hole environment. This thesis shows that regardless of the transducer, a single resonant harvester tuned to the frequency with the maximum displacement times frequency cubed produces more power than a farm of resonant harvesters tuned to a range of frequencies. Additionally, this thesis shows that an electromagnetic harvester can be passively tuned to increase the power in a non-stationary system with a peak frequency that is a function of time. Finally, this thesis presents a new resonant, rotational architecture, which has the advantage of simultaneously maximizing the coupling inertia and displacement.

Thesis Supervisor: Alexander H. Slocum
Title: Professor of Mechanical Engineering

Acknowledgments

Many people have been instrumental in the completion of this thesis and I would be remiss if I neglect to mention them. I would like to start by thanking Alexander Slocum, my thesis chair, advisor and mentor. Alex helped me find direction during my thesis work. He helped me find funding and helped direct me toward a suitable topic. He offered encouragement and respite when needed. Thank you Alex for your guidance and mentorship.

I am also grateful for my thesis committee who helped to guide me academically. I am especially grateful for the time and ideas provided by Jeff Lang. He met with me nearly every week advising me on many topics, particularly electrical engineering aspects of the thesis. Jahir Pabon also met with me nearly weekly and I am grateful for his ideas and insights. I would also like to thank my fellow PERG lab members for being there to bounce ideas off and for the mutual support.

I am also greatly indebted to the technical staff in Pappalardo and Edgerton Student shops. I really like to make things, and the guidance provided by Mark, Ken, Steve, Steve, (yes two Steves) and Gery were invaluable. Similarly, the administrative staff that helped me with all the paperwork and administrative tasks that are necessary to finish an project. Thank you Leslie, Joan, Deborah, and Maureen.

I am also immensely grateful for the support of my family. My parents who have always been supportive and encouraging. My children who have sacrificed a significant amount of time with there father so I could finish an experiment or paper. My wife has been a great support to me and has willingly encouraged me to endlessly continue on. Thank you to all!

Contents

1 Introduction **19**

1.1 Motivation 21

1.2 Functional Requirements 22

1.2.1 Form Factor/Geometric Constraints 23

1.2.2 Environmental Constraints 23

1.2.3 Acceleration Inputs 24

2 Background and Modeling **33**

2.1 Physical Model 33

2.2 Formulation of Governing Equation of Motion 34

2.3 Frequency Analysis 37

2.4 Transduction Types 43

3 Harvesting Architectures **45**

3.1 Resonant Harvester 46

3.1.1 Spring-Mass-Damper Solution 46

3.1.2 Power 49

3.1.3 Damping 53

3.1.4 Conclusions 56

3.2 Farm Systems 58

3.2.1 Baseline 58

3.2.2 Two frequency input 61

3.2.3 Both Move 64

3.3 Active Control 67
3.3.1 Statement of the General Optimal Control Problem[4] 70
3.3.2 Formulation of General Vibration Energy Harvesting Problem as an Optimal Control Problem 71
3.3.3 Application of the Solution to Analytically Solvable Problem . 76
3.3.4 Harvester Model 78
3.3.5 Analysis of Roundy Model 79
3.3.6 Equivalent Mechanical Components Model 81
3.3.7 Current Controlled Electro-magnetic Transducer 89
3.3.8 Conversion of Electrical to Mechanical Components 96
3.3.9 Comparison 102
3.3.10 Torque Constant 104
3.3.11 Impedance matching 105
3.3.12 Aside for general solution of K_e and b_e 108
3.4 Inertial 110
3.4.1 Spring Mass Damper Model 110
3.4.2 Inertial Model 112
3.4.3 Ratchet Model 113
3.4.4 Results 114

4 Rotational Prototype **123**
4.1 Spring Constant 126
4.2 Internal Damping 126
4.3 Electro-magnetics 126
4.3.1 Modeling 126
4.3.2 Results 130
4.3.3 Solution of $\lambda_B = 0$ for $s \neq p$ 132
4.3.4 Modeling 132
4.3.5 Results 136
4.3.6 Modeling 136

4.3.7 Results 145
4.3.8 Coils 152

A Matlab Codes **159**

A.0.9 Calculation of EMF 159
A.0.10 Calculation of EMF 161
A.0.11 Calculation of Induced Voltage for Constant Angular Velocity Input 163
A.0.12 Calculation of Induced Voltage for Oscillating Angular Input . 165
A.0.13 Symbolic Solution of Potential Constants 169
A.0.14 Numerical visualization of the convergence of the infinite series solutions 170
A.0.15 Calculation and visualization of the vector flux density ($\tilde{\mathbf{B}}$) . . 172
A.1 Matlab Data Reader Script 178
A.2 Matlab Rotation Script 183
A.3 Matlab Fourier Transform Script 187

B Test Setup **189**

B.1 Actuator Torque Analysis 189
B.2 Nomenclature 194

C Additional Acceleration Information **197**

C.1 Raw Data 197
C.2 Rotation of raw data to standard cylindrical coordinates 202

List of Figures

1-1 Form Factor 23
1-2 Accelerometers 25
1-3 x_1 accel. vs. time 26
1-4 x_2 accel. vs. time 26
1-5 y accel. vs. time 27
1-6 z accel. vs. time 27
1-7 Raw Gyro data 28
1-8 Gyro data cross-correlation 29
1-9 Time shifted Gyro data 30
1-10 Time shifted Gyro Data (zoomed) 31

2-1 Two-damper model 34
2-2 FBD 35
2-3 x_1 accel. vs. freq 40
2-4 $x2$ accel. vs. freq 41
2-5 y accel. vs. freq 41
2-6 z accel. vs. freq 42
2-7 Tangential Acceleration (Zoom) 42
2-8 Spectrogram 43

3-1 Standard Base Excitation Model 46
3-2 Free Body Diagram of the vibrating mass 47
3-3 Magnitude and phase of $G_{\ddot{y}^2|P}$ 51
3-4 Model of System Damping 54

3-5 Proportional Power vs. b_e/b_i 55
3-6 $P \cdot (\omega_n/mQ_i)$ vs. A_n. 56
3-7 Assumed Sinusoidal Amplitude as a function of Frequency 57
3-8 Estimated Maximum Power as a function of Frequency 57
3-9 Maximum power vs natural frequency 63
3-10 Both move 65
3-11 Both Move power high K_c 68
3-12 Both Move power high K_c (wide-band) 68
3-13 Both move - multiple values of K_c 69
3-14 Reference Model 72
3-15 Force Body Diagram 72
3-16 Lumped Parameter Model 76
3-17 Harvester Model 79
3-18 Comparison of Roundy Model 80
3-19 Instantaneous Power 84
3-20 Average Power 87
3-21 Torque 89
3-22 Electrical Model 93
3-23 Passively Conrolled 95
3-24 Passive Power 97
3-25 Equivalent Mechanical Model 98
3-26 Inductance 100
3-27 Resistance 101
3-28 Tuning vs. x 102
3-29 Tuning vs. r 103
3-30 Torque Constant 104
3-31 Inductor Resistance 106
3-32 Inductance vs. x 107
3-33 Inductance vs. r 107
3-34 Capacitance vs. r 108

3-35 SMD model 111
3-36 Inertial Model 112
3-37 Ratchet Model 113
3-38 Internal Damping 115
3-39 Simulations (separate optimization) 116
3-40 Simulations (global optimiztation) 116
3-41 Comparisons 117
3-42 46th trace 118
3-43 Predicted Power 119
3-44 Power sensitivity 120
3-45 Displacement and Velocity 121

4-1 Volume Limited 124
4-2 Numerical Solution - Volume Limted 125
4-3 Schematic model of the current distribution 127
4-4 Induced voltage ($\phi = \omega t$) 131
4-5 Induced voltage ($\phi = \phi_A \sin(\omega t) + \phi_0$) 131
4-6 Equivalent circuit 133
4-7 End-turn Length 135
4-8 Representative axial cross-section of electric machine (open-circuit) . 137
4-9 Radial flux density (B_r) at $r = r_{oc}$ — Relative error as a function of k 147
4-10 Vector plot of the flux density ($\tilde{\mathbf{B}}$) 148
4-11 *Radially directed magnetic fields passing through the copper bars create circulating currents* 148
4-12 *Faraday's law is used to calculate the electric field around a closed loop through which a time varying magnetic field passes.* 149
4-13 *Magnetic field evaluated at the core back iron across one magnetic pole pair. The red indicates the worst possible expected oscillation of value of magnetic field through a bar.* 150
4-14 *Illustration of the surface wound coil design.* 152

4-15 *Copper cylinders with geometry cut out of using Omax MicroWater Jet (Patent Pending).* 153
4-16 *The top cylinders are oxidized in an attempt to create an insulaiton layer. However, the oxide layer was flaky and unreliable as an insulation. The bottom picture is a Paralyene coated cylinder.* 154
4-17 *Flexible hone used to de-burr the interior surface or the outer cylinder* 155
4-18 *Ideally, the insulated inner cylinder can be inserted into the insulated outer cylinder. However, if necessary the outer cylinder can be split along one of the slits to create more clearance.* 155
4-19 *Assembled cylinders are placed in a mold and potted in epoxy to affix the cylinders and provide additional structure.* 156
4-20 *The support rings created by the extra long cylinders being cut off.* . . 156
4-21 *The end turns are created by dip soldering.* 157
4-22 *Completed Coil* 157

B-1 *Torque analysis of the test setup. The rotary solenoid provides an actuation torque that is resisted by the inertia of the coupling and harvester casing. Additionally, the forces on the rotor inside the harvester apply a reaction torque to the base.* 189
B-2 *Plot of an example acceleration input. The data is measured with a velocity gyro and numerically differentiated in Matlab to obtain the acceleration. The data is collected over approximately 900s. The top plot is a small window of the rotational acceleration $\ddot{\alpha}$ as a function of time. The bottom plot is a DFFT in Matlab of the entire data run.* . . 192
B-3 *Torque components* 192
B-4 *Solid model of the test setup with the inertial ring.* 193
B-5 *Torque components with added inertia* 194

C-1 198
C-2 198
C-3 199

C-4 200
C-5 200
C-6 201
C-7 203

List of Tables

3.1 Units Analysis 83
3.2 *Numerical values used for inductor and resistor calculations* 101

4.1 Numerical Values used for EMF calculations 130
4.2 Numerical Values used in fields graphics 145
4.3 Values of the constants in the current prototype 151

B.1 Nomenclature 195

Chapter 1

Introduction

Many mechanical or electro-mechanical systems produce mechanical vibrations. The kinetic energy associated with these mechanical vibrations represents a potential source of energy for sensors and other electronics. In general, *vibration energy harvesting* is the process of scavenging the kinetic energy in these ambient vibrations by converting the mechanical kinetic energy into electrical energy, which is easier to store and transmit.

Many methods exist to transduce mechanical kinetic energy to electrical energy, but regardless of the transduction method, the majority of devices described in the literature rely on an inertial proof mass connected to the vibrating environment [18]. Common forms of transduction include active materials, such as piezoelectrics; and various forms of electromagnetic transduction, such as induction[3, 21, 20]. Active materials transduce the energy by using a inertial reference to convert the kinetic energy into strain energy and then converting the strain energy into electric energy [2, 26, 5, 28, 29]. Conversely, electromagnetic transducers utilize the relative motion between the vibrating source and some form of inertial reference to convert the kinetic energy into electric energy.

Usually, ambient vibrations are considered parasitic and thus great care is taken to reduce their amplitude. To effectively harvest the energy of these vibrations, the vibration amplitude should be amplified. Commonly, the amplitude is amplified by coupling the inertial proof mass to the vibrations source with a conservative spring.

The inertial mass, coupling spring, and energy extraction by energy harvesting comprises a common spring-mass-damper system nearly identical to tuned-mass dampers that are found in most vibration text books (and many buildings) [14, 13, 30]. In fact, as was originally shown by Williams and Yates [30], especially for low frequency sources, both of the common transduction methodologies mentioned above can be reasonably modeled as equivalent viscous dampers resulting in a model for energy harvesting that is identical to tuned-mass-dampers.

Assuming the input vibration to the harvester is harmonic and invariant, the tuned-mass-damper model provides an analytical upper bound for the power that can be harvested as a function of the vibration input characteristics and system parameters. Additionally, if the vibration is a sum of harmonic functions, then similarly, standard transfer function methods can be used to solve for the maximum power that can be extracted by the equivalent viscous damper. However, when the vibration amplitude is spread over many frequencies, the amplitude of vibration at an one frequency is typically less since physical constraints usually limit the total vibration. Thus, in a wide band input, the energy is spread across multiple frequencies leaving less energy at the resonant frequency of the tuned-mass-damper. Also, the if the input is stochastic, then the spring-mass system does not resonate. One of the primary accomplishments of this thesis is the analysis of several methods to address these problems, namely farms, inertial dampers (no spring), ratchet-type rectifying systems, and frequency tracking. The thesis shows that a single resonator actually harvests more energy than a farm of resonators, and that for the input parameters and functional requirements of down-hole energy harvesting a frequency tuned resonant harvester is the better than an inertial or ratchet harvester.

As with most real designs, the energy harvesting device must fit within a prescribed volume. As such, the size and displacement of inertial proof mass are not independent in linear energy harvesters. However, as proposed by [31], since the size of the proof mass is independent of the proof mass's rotation in harvesting architectures based on a rotating proof masses, rotating architectures provide potential advantages over linear architectures. Additionally, for energy density and tempera-

ture reasons, the rotational prototype energy harvester presented in this thesis uses electro-magnetic induction as the damping element/transducer. As shown by [?] when using electro-magnetic transduction as the method for energy harvesting a shearing magnetic circuit is more magnetically efficient than an axial or plunging circuit. A rotating proof mass naturally provides a shearing air gap taking advantage of the higher efficiency shearing magnetic circuit, which further increases the advantages of a rotational architecture. The second major accomplishment of this thesis is the development of design tools to design resonant-rotational energy harvesting devices.

The contribution of this thesis to the field is the development of a design methodology and a set of design tools to support that design methodology. Given a prescribed form factor and vibration input, the design tools aid a designer to choose an appropriate architecture for energy harvesting.

The remainder of this chapter is devoted to explaining the motivation and functional requirements for this research. Chapter 2 develops the general theory and background of energy harvesting. Chapter 3 explains the analysis of wide-band energy harvesting strategies. Chapter 4 explains the use of the design tools by describing the design of a resonant-rotational energy harvester.

1.1 Motivation

Oil, natural gas, and other similar natural resources are becoming harder to access. Resources are now being utilized that are deeper and/or in more difficult formations than ever before. Accessing these resources requires more sensors to measure the drilling process. Additional sensors placed at the bottom of an oil well can potentially be used to improve real time control of the drilling process and to improve understanding of the drilling process (especially as it pertains to new rock strata). Better control and understanding can improve the efficiency of drilling, allowing access to even more difficult to reach resources. Just as important is communication. Telemetry and real time control of the drilling process require reliable communication back-and-forth between the bottom of the well and the surface.

Supplying power to the sensor, telemetry and communication systems and providing a reliable communication channel to the surface is challenging. Modern oil wells are 30,000 ft or longer in approximately 30-90 ft sections. Thus, imbedding a wire in the drill string has significant technological challenges. Even if the efficiency and reliability of each joint is 99% a 30,000ft well will have a minimum of 300 joints and thus the overall efficiency and reliability will only be about 4%. However, the process of drilling an oil well produces a significant amount of vibration. If the kinetic energy associated with these vibrations could be utilized to power downhole sensors, the efficiency of drilling could be increased. The efficiency is increased directly by reducing the power that must be sent down-hole to power sensors and communications. Also, adding additional sensors will allow researchers to better understand drilling and increase efficiency. Even more importantly, vibration energy is available along the length of the pipe. Harvesting this energy to power wireless communication systems can drastically increase the communication band-width between the bottom-hole-assembly and the surface. With increased communication comes the possibility of faster telemetry data for better locational control, which will increase the utilization of the resources within a well. Thus, harvesting ambient vibration energy in a drill sting can increase the efficiency and accuracy of drilling allowing us to access and utilize much needed but more complicated and difficult to reach resources.

1.2 Functional Requirements

Although this thesis addresses many general issues associated with energy harvesting of wide-bandwidth vibrations, since the prototype device is intended as a first prototype down-hole energy harvester, it is important to understand the functional requirements associated with down-hole energy harvesting. Some of the decisions made pertaining to the design are dependent on the prescribed form-factor and vibration input. In fact, the design rules associated with realizing that "non-laboratory" energy harvesters must fit within a prescribed volume is part of the advancement of the thesis.

The functional requirements are arraigned in 3 general areas: Geometric Constraints, Environmental Constraints, and Expected Acceleration Inputs.

1.2.1 Form Factor/Geometric Constraints

In order to integrate into existing tools, the prototype device must fit into the provided size allocation and is to be located in the center of the tool/pipe (Fig. 1-1). The device

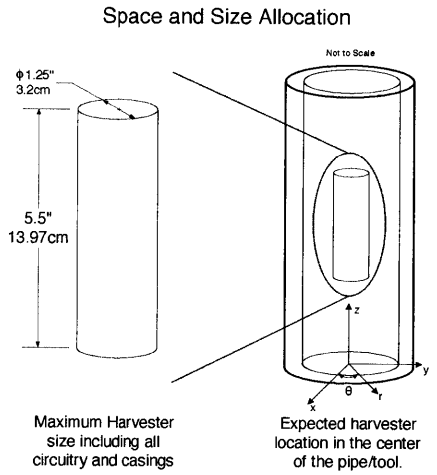

Figure 1-1: *Space and size allocation for harvester device*

is expected to be a 5.5in tall, 1.25in diameter cylinder. The entire device including harvesting, casing (pressure compensation), and electronics is expected to fit in this cylinder. The harvester device does not float in the center of the tool as Fig. 1-1 might suggest. The figure is simply to show the location. The device fits within other instrumentation and is rigidly attached to this instrumentation, which is rigidly attached attached to the pipe.

1.2.2 Environmental Constraints

The bottom of an oil well is an extreme environment. As such some of the requirements to certify a tool guide the design. The two requirements that are of the most interest in this thesis are 300°F external temperature and 250 g shock loads. Since

there is a not cold sink to provide cooling, the prototype device must be capable of operating at a temperature of 300°F. This puts a restriction on the materials that can be used in the design. In particular, active materials, which are commonly used as a transduction method in energy harvesting devices, have a breakdown temperature that is less than 300°F. Thus, this thesis focuses primarily on electro-magnetic induction as the transduction method. Neodymium Boron magnets are the preferred permanent magnets for high performance electric machines due there superior magnetic remenance. However, Neodymium Boron magnets have magnetic relaxation temperatures below 300°F. Thus, down-hole ready devices must use Sumarium Cobalt magnets.

Although the harvester is not expected to regularly encounter 250 g accelerations, the harvester must be able to survive and continue to operate after such shock loads. Many harvester components must be designed with the shock requirements in mind, but as detailed later, the prototype harvester uses a torsion rod as a spring element. The torsion rod is most effected by the shock load requirement, and is made from super-elastic material (Nitinol^{TM}) to withstand the load.

Environmental considerations also govern the materials that can be used down-hole. In particular, stainless steel components are used throughout the harvester. Unfortunately, stainless steel has low magnetic permeability and saturates easily. Low saturation requires the rotor and stator "back iron" to be thicker than magnetic steels. Thicker back iron increases the thickness of the outer casing, which in turn reduces the size of the rotor reducing the inertia.

1.2.3 Acceleration Inputs

Again, many lessons learned in this thesis can be applied broadly to the general energy harvesting problem. However, like form factor, the expected accelerations in a down-hole environment govern the design. The remainder of this section describes a set of example vibration data measured with accelerometers and a set of example vibration data measured with a gyroscope.

Accelerometer Data

Starting with the acceleration data, Fig. 1-2 is an illustration of the accelerometers used to measure the vibration on two different down-hole tools: BAF and DBSEIS. Four accelerometers were used to measure the vibration: two accelerometers are ar-

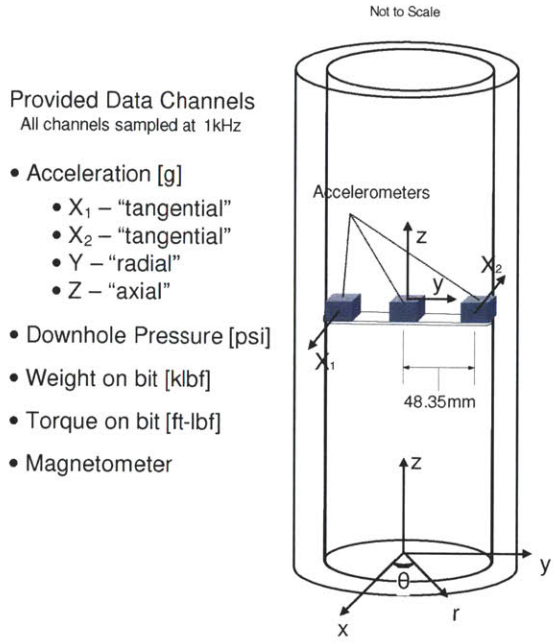

Figure 1-2: *Illustration of provided data*

ranged in the plus and minus x direction and located on radially opposed ends of the pipe 48.35 mm from the centerline, an accelerometer in the center of the pipe directed in the y direction, and an accelerometer in the center of the pipe directed in the z direction. The accelerometers are digitally sampled at 1kHz and several data sets of about 300 s are provided for each tools. The acceleration data is shown in Figs. 1-3 through 2-6. The harvester is expected to make the maximum power possible when excited by acceleration inputs similar to those provided.

Gyroscopic Velocity Data

In addition to acceleration data, more direct rotational velocity data is also provided by a set of two gyroscopes located in the center of the pipe. The provided velocity

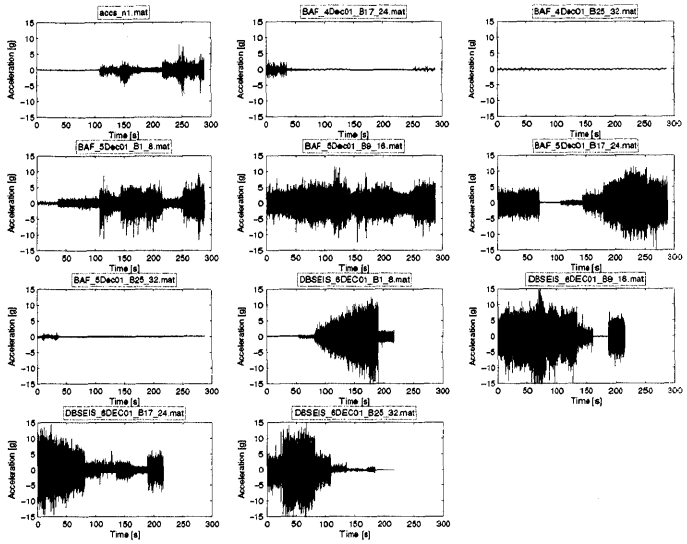

Figure 1-3: *Plot of the y acceleration as a function of time*

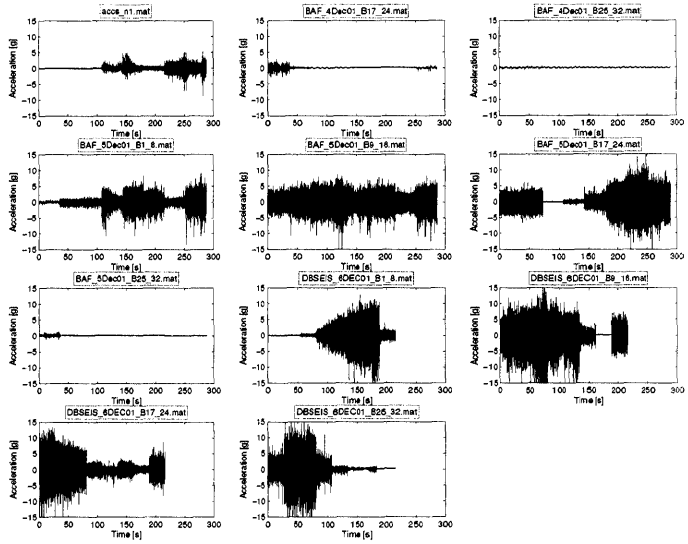

Figure 1-4: *Plot of the y acceleration as a function of time*

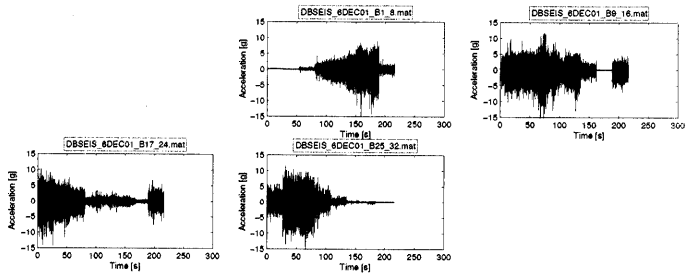

Figure 1-5: *Plot of the y acceleration as a function of time*

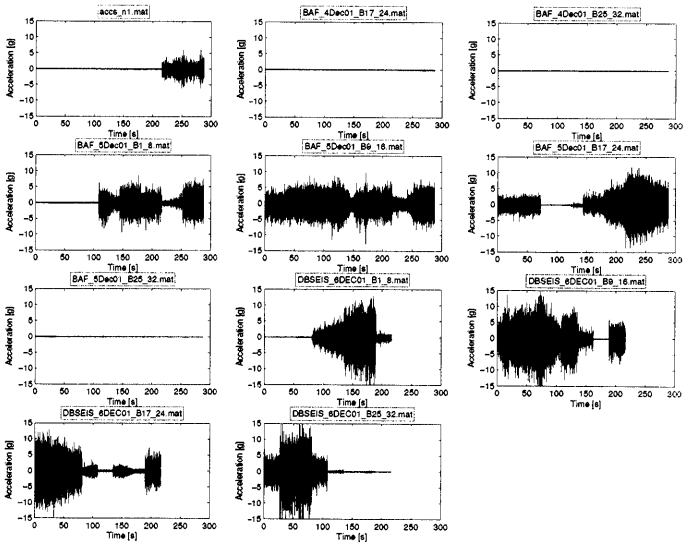

Figure 1-6: *Plot of the z acceleration as a function of time*

data is in the from of 8 arrays sampled at 1024 Hz for 1000 s. The raw data is plotted in Fig. 1-7. Based on the naming scheme for the data arrays (gyro1, gyro12, gyro2,

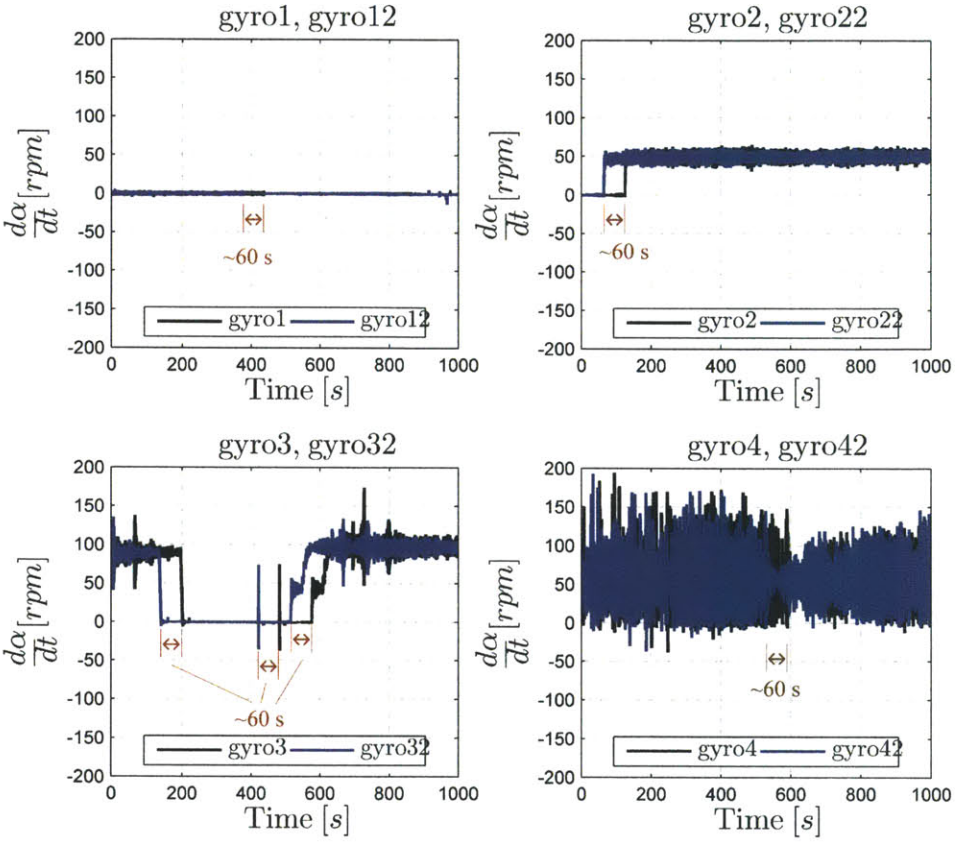

Figure 1-7: *Measured velocity data provided by the Stonehouse facility to be used as an example expected input to the harvester. Similarly named data appears to be identical with an approximately 60 s time shift.*

gyro22,...) the data is plotted in 4 subplots with similarly named data plotted on the same axes.

Although it is not exactly known how the velocity data was taken, it is clear from visual inspection of the plotted data that the similarly named data sets are related. Closer inspection of the upper-right axis shows a step from zero mean velocity to approximately 50 rpm mean velocity in both gyro2 and gyro22 data sets. However, the gyro22 data set shows this step approximately 60 s before the gyro2 data set. A

similar time delay is seen in all the major steps and impulses. Cross-correlation of the similar data sets by use of Matlab's xcorr(x,y) function shows a maximum cross-correlation between sets of approximately 60 s in all 4 cases (Fig. 1-8). In Fig. 1-9 the

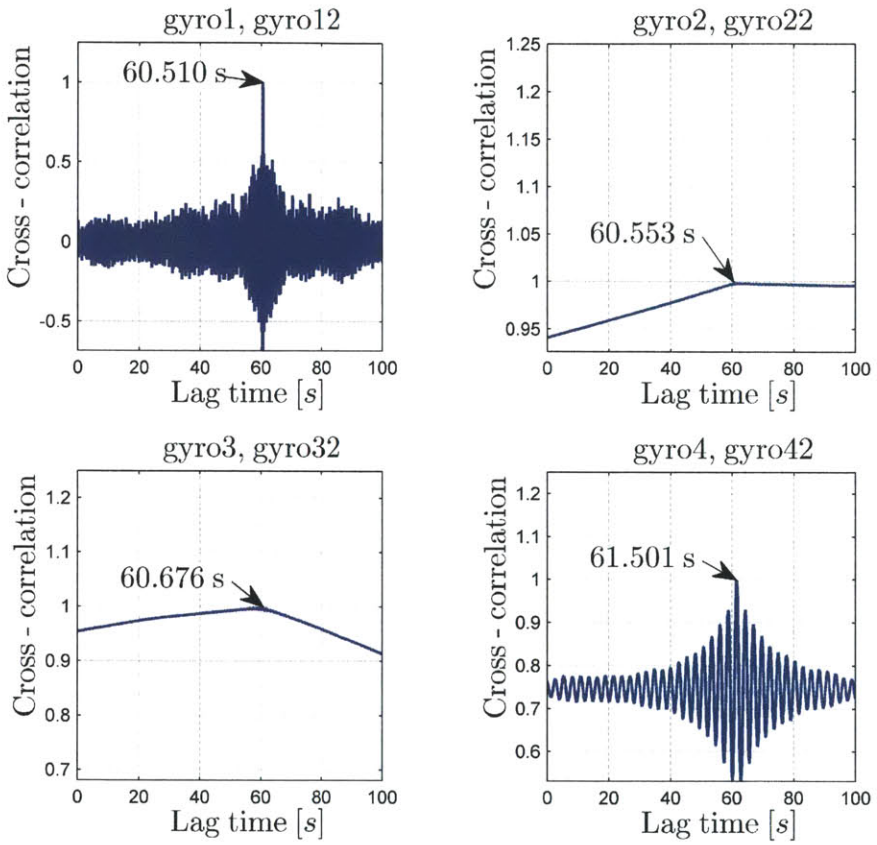

Figure 1-8: *Cross-correlation of similar data sets using Matlab's xcorr(x,y) function.*

velocity data is replotted with each of the gyro$i$2 arrays time delayed by the values in Fig. 1-8. The distinctive steps and impulses now align, however, as can bee seen most clearly in the top right and bottom left subplots, the measured velocities are not identical. Figure 1-10 is a plot of the shifted velocity data zoomed in to look at a single second of time. Both signals capture the same general features, but contain high frequency noise.

Assuming the sensors that took the two different velocity traces can be modeled

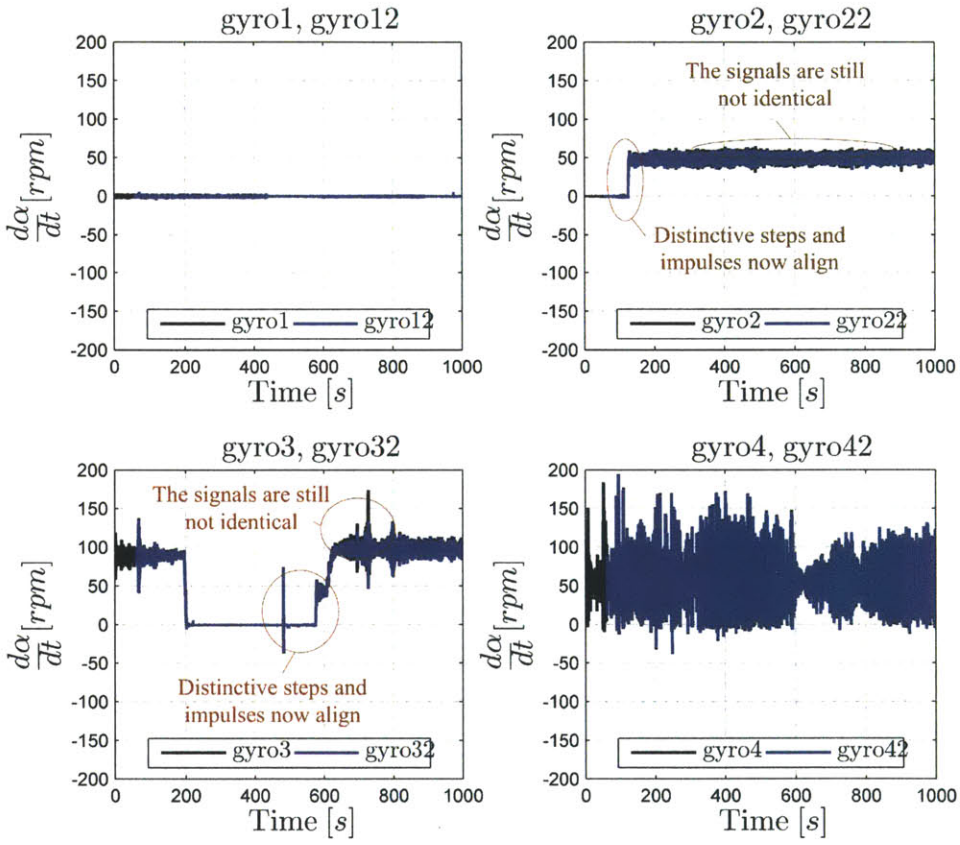

Figure 1-9: *Measured velocity with the time shifts shown in Fig. 1-8 applied to the gyroi2 data sets. All the distinctive features now match; however, some differences in the signals still exist.*

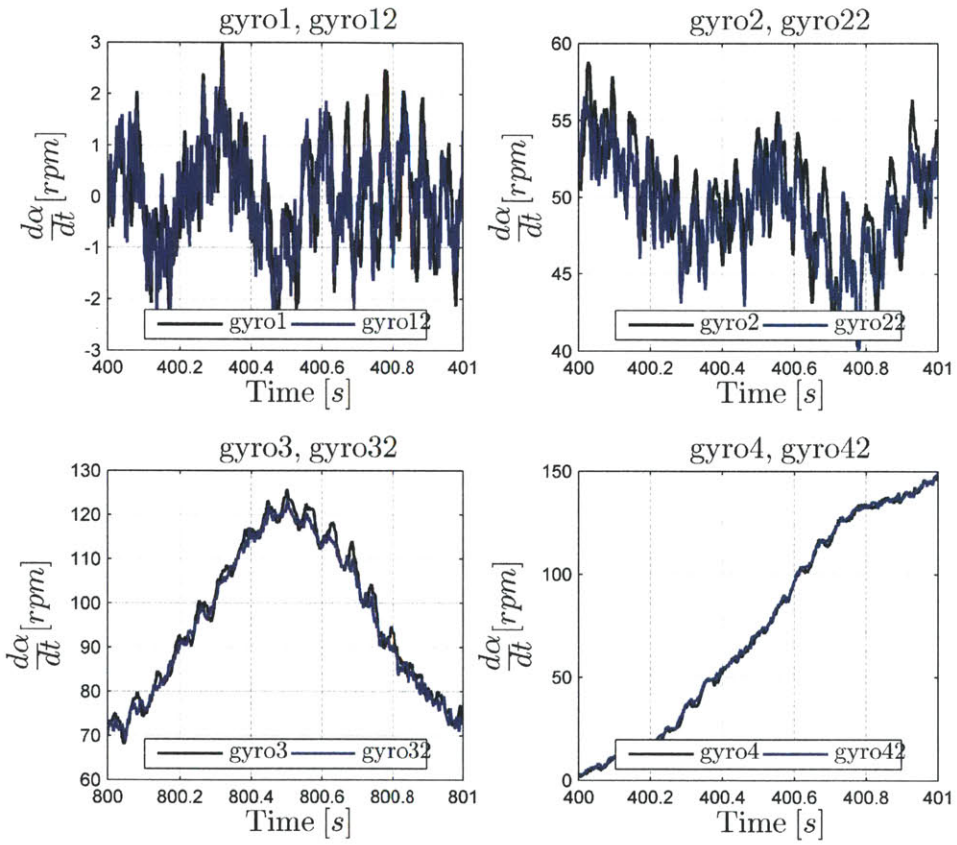

Figure 1-10: *Zoomed in view of the shifted velocity data.*

as,

$$\frac{d\alpha}{dt}_1 = V(t) + w_1(t) \tag{1.1}$$

$$\frac{d\alpha}{dt}_2 = V(t) + w_2(t) \tag{1.2}$$

where $\frac{d\alpha}{dt}_i$ is the measured velocity of sensor i, $V(t)$ is the actual velocity of the system, and $w_i(t)$ is the noise for sensor i. Under this assumption, the difference in the time shifted velocity signals results in a model for the difference of the noise in the signal.

Although both acceleration and velocity data are important to the general cases that are examined. The gyro data is the most important for the prototype. Additional example acceleration measured at the drill head was also provided an is given in appendix C.

Chapter 2

Background and Modeling

Most energy harvesting devices can be described with a mass-spring-damper model as originally proposed by Williams and Yeats [30]. This model needs some adjustment. Specifically, the Williams and Yeats model extracts energy out of a single damper. However, in actuality, internal energy losses are unavoidable and must be included in the model. This chapter develops the two damper resonant harvester model that can also be used as the basis for resonant, farm, non-linear, and optimal control architectures.

Due to the temperature related functional requirements this thesis deals exclusively with electro-magnetic energy harvesters, but electro-magnetics are not the only way to transduce the kinetic energy into electric energy. A brief discussion of the other conversion methods is provided at the end of this chapter.

2.1 Physical Model

Figure 2-1 is a lumped parameter model of energy harvesting as a tuned mass damper. The model consists of an inertial proof mass connected to the vibrating source by a spring and a pair of equivalent viscous dampers. The spring and mass can be considered linear constant coefficient, making the system a simple resonator, or can be some combination of non-linear components, making the system non-linear or controllable. The dampers represent the energy lost to the environment and the

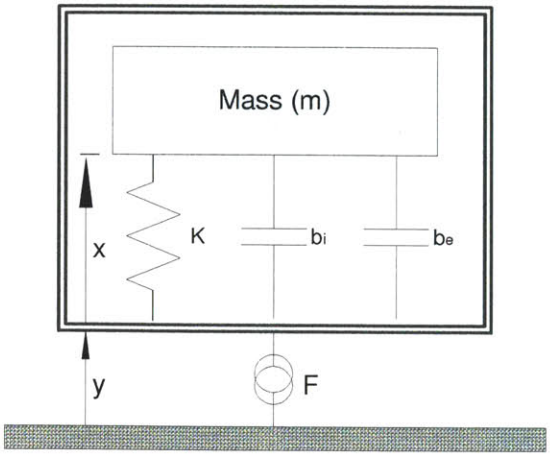

Figure 2-1: *Physical model used to make the 1st order power predictions. The system consists of a spring mass damper system excited by a known acceleration. The energy loss terms are lumped into internal mechanical losses, and electrical losses. The extracted power is a portion of the electrical losses.*

energy harvested from the vibration. For stationary inputs, the spring and damper are tuned to the frequency component with the most energy. Under these assumptions the model is solvable analytically, and the analytical solution to a harmonic input represents the upper bound of power that can be harvested from a given vibration. For non-stationary inputs or non-linear components, the equations must be solved numerically.

2.2 Formulation of Governing Equation of Motion

Generating the governing differential equations for the model in Fig. 2-1 requires a few assumptions:

- The force transducer is of infinite power. Thus, the input displacement (y), velocity ($\dot{y}$), and acceleration ($\ddot{y}$) are invariant. For down-hole drilling, this is a perfectly reasonable assumption since the inertia of the pipe is many orders of magnitude more than the inertia of the proof mass and thus, the reaction force of the device on the vibrating device is small and does not appreciably change the vibration parameters.

- The electrical damping can be modeled as and equivalent viscous damper (i.e. $F_e = b_e\dot{x}$). Based on the work done by Arnold [3], Anton et. al [2], Roundy et. al [21, 20], and Meninger et. al [17], both active material and electrodynamic methods for converting the energy can be modeled as equivalent viscous dampers in many regimes. Thus, this is also not much of a limiting assumption.

Under these assumptions, the governing equations of motion are formulate by the summing the dynamic forces on the proof mass (Fig. 2-2).

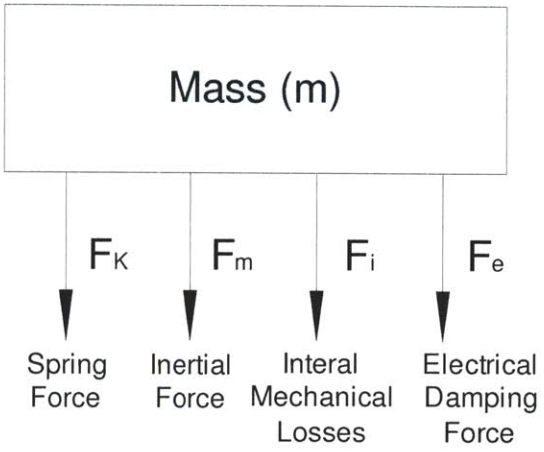

Figure 2-2: *Force Body Diagram of the system mass used to formulate the governing equation of motion.*

$$\sum F = 0 \tag{2.1}$$

$$F_k + F_m + F_i + F_e = 0 \tag{2.2}$$

$$Kx + m\frac{d^2}{dt^2}(x+y) + b_i\dot{x} + b_e\dot{x} = 0 \tag{2.3}$$

$$m\ddot{x} + (b_i + b_e)\dot{x} + Kx = -m\ddot{y} \tag{2.4}$$

$$\ddot{x} + \frac{b_i + b_e}{m}\dot{(x)} + \frac{K}{m}x = -\ddot{y} \tag{2.5}$$

To simplify the numerical solution of the governing equation of motion, formulate the system as a set of first order equations.

$$\dot{x} = \dot{x} \tag{2.6}$$

$$\ddot{x} = -\frac{K}{m}x - \frac{b_i + b_e}{m}\dot{x} - \ddot{y} \tag{2.7}$$

Or in matrix form,

$$\begin{Bmatrix} \dot{x} \\ \ddot{x} \end{Bmatrix} = \begin{bmatrix} 0 & 1 \\ -\frac{K}{m} & -\frac{b_i+b_e}{m} \end{bmatrix} \begin{Bmatrix} x \\ \dot{x} \end{Bmatrix} + \begin{Bmatrix} 0 \\ -\ddot{y} \end{Bmatrix} \tag{2.8}$$

$$\dot{\mathbf{x}} = \mathbf{A}\mathbf{x} + \mathbf{B} \tag{2.9}$$

Where, as in the diagram x is the relative displacement between the proof mass and the source, K is the spring constant and could be a function of x, m is the mass of the inertial proof mass and is always assumed constant, b_i is the equivalent viscous damping coefficient of the system losses, b_e is the equivalent viscous damping coefficient of the harvested energy, and y is the input displacement. The instantaneous power extracted by the harvester is a the product of the force and velocity in the damper, and the time average power is given as,

$$P = \frac{\alpha}{T}\int_0^T b_e \dot{x}^2 dt \tag{2.10}$$

Where, α is an electrical loss coefficient which is a function of the conversion efficiency, internal electrical losses, and rectification efficiency.

In some specialized cases, the equations can be solved analytically (see Chap. 3). However, most general cases must be solved numerically. The various specific analytical solutions are left to the special cases in in Chap. 3, and the simple euler method

is presented here for completeness [7].

$$\mathbf{u}_{n+1} = \mathbf{x}_n + \frac{1}{f_s}\left[\mathbf{A}\mathbf{x}_n + \mathbf{B}_n\right] \tag{2.11}$$

$$\mathbf{x}_{n+1} = \mathbf{x}_n + \frac{1}{2f_s}\left[\mathbf{A}\mathbf{x}_n + \mathbf{B}_n + \mathbf{A}\mathbf{u}_{n+1} + \mathbf{B}_{n+1}\right] \tag{2.12}$$

$$= \mathbf{x}_n + \frac{1}{2f_s}\left[\mathbf{A}\left(\mathbf{x}_n + \mathbf{u}_{n+1}\right) + \left(\mathbf{B}_n + \mathbf{B}_{n+1}\right)\right] \tag{2.13}$$

2.3 Frequency Analysis

Frequency analysis is important to identify the type of harvester that should be used for given input. Two analyses are necessary to determine the frequency characteristics. First it must be shown that the input vibration is stationary. If the system is stationary, a Fourier analysis can be used to determine the frequency components. If the vibration is not stationary, then a spectrogram, which is a Fourier analysis of small subsets of the data shifted in time, can be used to determine if the vibration is contains a sharp frequency peak wandering in time. This thesis will address to some extent each of these cases.

If the input is stationary, then Fourier analysis is used to represent the amplitude of acceleration as a function of frequency. Frequency domain representation of the data allows the designer to identify the amplitude of vibration as a function of frequency for first order power estimates, and to identify the frequency of vibration at which the harvesting device should be tuned to maximize resonance (and power). Again for completeness the general theory is given. What is of importance to the designer is and understanding of the frequency resolution.

The acceleration is represented by a sum of harmonic functions, where ultimately, the goal is to obtain the harmonic acceleration amplitude function as a function of frequency ($A(\omega)$).

$$A(t) = \sum_{\omega} A(\omega)\sin\left(2\pi\omega t + \delta(\omega)\right) \tag{2.14}$$

Matlab's Fast-Fourier Transform function (FFT) is utilized to facilitate the transformation, thus the harmonic representation of the acceleration is rearranged to better

match the discrete form used by Matlab. Start by applying the complex exponential definition of sine, $\sin(\theta) = 1/2j\left(e^{j\theta} - e^{-j\theta}\right)$ [?],

$$\begin{aligned} A(t) &= \sum_{\omega=0}^{\infty} A(\omega)\left(\frac{e^{j(2\pi\omega t+\delta(\omega))} - e^{-j(2\pi\omega t+\delta(\omega))}}{2j}\right) \\ &= \sum_{\omega=0}^{\infty} A(\omega)\left(\frac{e^{j2\pi\omega t}e^{j\delta(\omega)} - e^{-j2\pi\omega t}e^{-j\delta(\omega)}}{2j}\right) \\ &= \sum_{\omega=0}^{\infty} \frac{A(\omega)}{2} j\left(-e^{j\delta(\omega)}e^{j2\pi\omega t} + e^{-j\delta(\omega)}e^{-j2\pi\omega t}\right) \end{aligned} \tag{2.15}$$

Defining $C(\omega) = -e^{j\delta(\omega)}$, and recalling that $\text{CONJUGATE}\left[e^{z}\right] = e^{\text{CONJUGATE}[z]}$[?], then,

$$\begin{aligned} -e^{j\delta(\omega)} &= C(\omega) \\ e^{-j\delta(\omega)} &= C^{*}(\omega) \end{aligned}$$

where * is used to denote the complex conjugate. Then the limits of the summation can be changed to simplify the harmonic expression of the acceleration.

$$A(t) = \sum_{\omega=-\infty}^{\infty} \frac{A(\omega)}{2} jZ(\omega)e^{j2\pi\omega t} \tag{2.16}$$

where,

$$Z(\omega) = \begin{cases} C(\omega) & \omega \geq 0 \\ -C^{*}(\mid \omega \mid) & \omega < 0 \end{cases} \tag{2.17}$$

Now introducing Matlab's discreet definitions[?],

$$X(k) = \sum_{n=1}^{N} x(n)e^{-j2\pi(k-1)\left(\frac{n-1}{N}\right)} \tag{2.18}$$

$$x(n) = \frac{1}{N}\sum_{k=1}^{N} X(k)e^{j2\pi(k-1)\left(\frac{n-1}{N}\right)} \tag{2.19}$$

To equate these expressions, recognize that in the discrete domain time is represented as,

$$t = \frac{n-1}{f_s} \tag{2.20}$$

where f_s is the sampling frequency. Thus the discrete acceleration is given as,

$$A(n) = \sum_{\omega=-\infty}^{\infty} \frac{A(\omega)}{2} jZ(\omega) e^{j2\pi\omega\frac{n-1}{f_s}} \tag{2.21}$$

Comparing the complex amplitude of equations 2.21 and 2.19 results in an expression for the acceleration amplitude as a function of frequency.

$$\text{ABS}\left[\frac{X(k)}{N}\right] = \text{ABS}\left[\frac{A(\omega)jZ(\omega)}{2}\right] \tag{2.22}$$

Recalling the definition of $Z(\omega)$ (equation 2.17) the complex amplitude can be evaluated as,

$$\begin{aligned}
\frac{1}{N}\text{ABS}\left[X(k)\right] &= \frac{A(\omega)}{2}\text{ABS}\left[\sin\left(\delta(\omega)\right) \mp j\cos\left(\delta(\omega)\right)\right] \\
\frac{1}{N}\text{ABS}\left[X(k)\right] &= \frac{A(\omega)}{2}\sqrt{\sin^2(\delta(\omega)) + \cos^2(\delta(\omega))} \\
\frac{1}{N}\text{ABS}\left[X(k)\right] &= \frac{A(\omega)}{2} \\
A(\omega) &= \frac{2}{N}\text{ABS}\left[X(k)\right]
\end{aligned} \tag{2.23}$$

Finally, comparison of equations 2.21 and 2.19 also yields the discrete definition of the frequency vector (measured in Hz) associated with Matlab's FFT definition of $X(k)$,

$$\omega = \frac{(k-1)f_s}{N} \tag{2.24}$$

The frequency resolution can then be defined as,

$$\begin{aligned}
\triangle\omega &= \omega_{k+1} - \omega_k \\
&= f_s\frac{(k+1)-1}{N} - f_s\frac{(k)-1}{N} \\
&= f_s\frac{k-k+1}{N} \\
&= \frac{f_s}{N}
\end{aligned} \tag{2.25}$$

Since the sampling frequency must often be very large to avoid aliasing, the length of

the measured data must also be very long to produce sufficient frequency resolution to properly identify the frequency of maximum associated with the vibration.

Using Matlab, and the definition of acceleration amplitude as function of frequency provided in equation 2.23, Figs. 2-3 through 2-6 are plots of the amplitude of acceleration as a function of frequency of the raw data given in the previous section (Figs. ?? through ??). The Matlab script used to calculate the Discrete Fourier Transform and create the following frequency based plots is provided in appendix A.3.

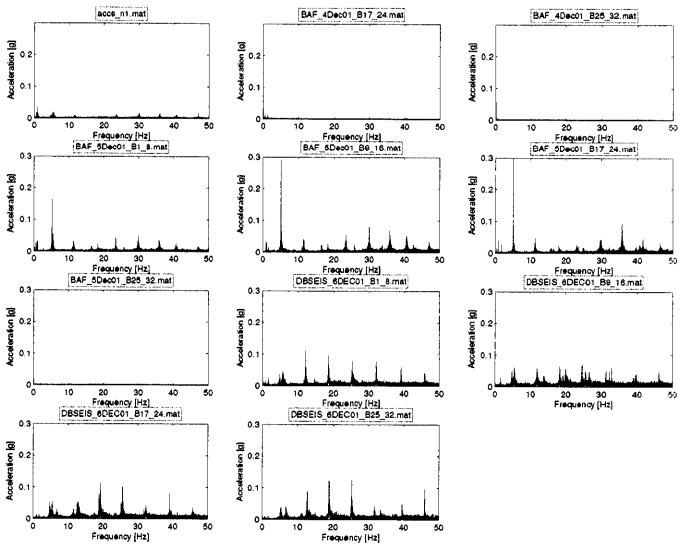

Figure 2-3: *Plot of the y acceleration as a function of time*

Several important observations should be noted. First, although the amplitude of acceleration in the time domain is relatively high, the component of acceleration amplitude at any given frequency is at least an order of magnitude lower. Since the power output of inertial based energy harvesters scales linearly with the harmonic amplitude of acceleration [14, 31, 25], the expected power is at least an order of magnitude less than the amplitude of acceleration in the time domain would suggest [10].

Second, the acceleration is distributed over a relatively large bandwidth. Figure 2-7 is an enlarged plot of the average of the Fourier transforms of the tangential acceleration data. The important features that a designer should be aware of are the

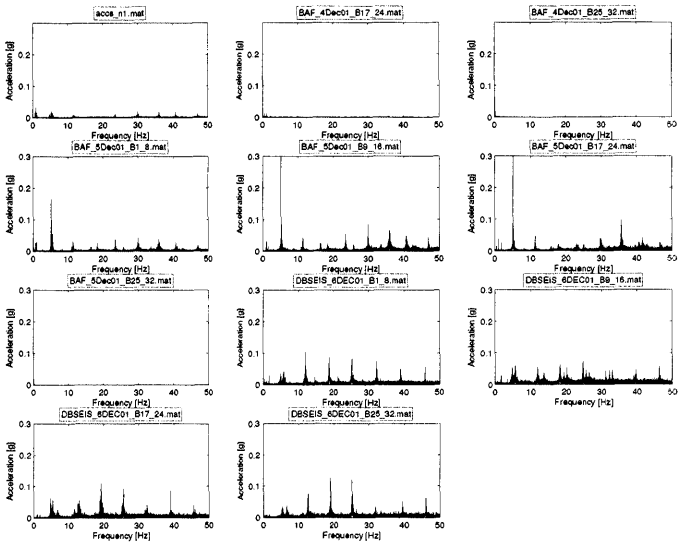

Figure 2-4: *Plot of the z acceleration as a function of time*

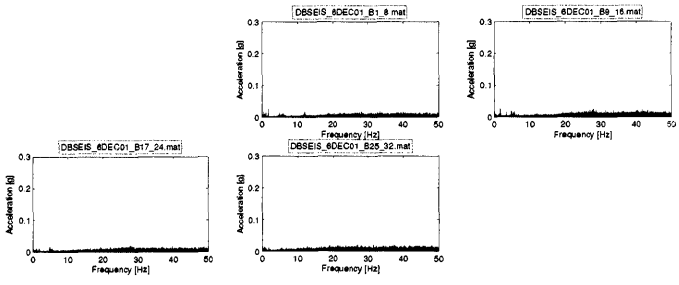

Figure 2-5: *Plot of the y acceleration as a function of time*

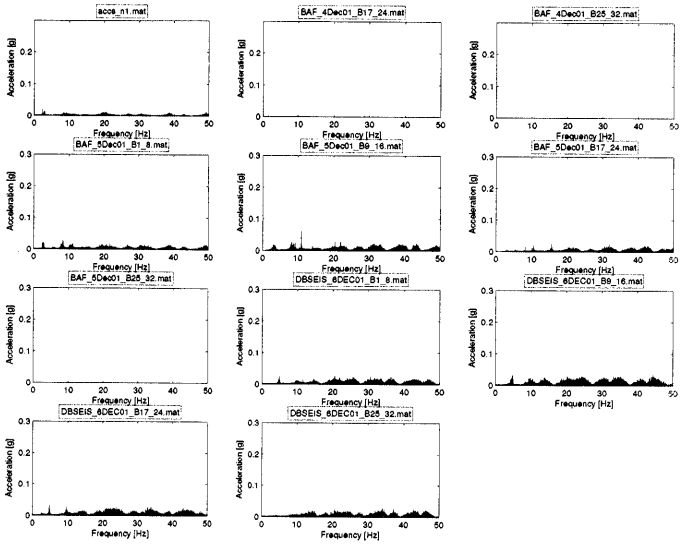

Figure 2-6: *Plot of the z acceleration as a function of time*

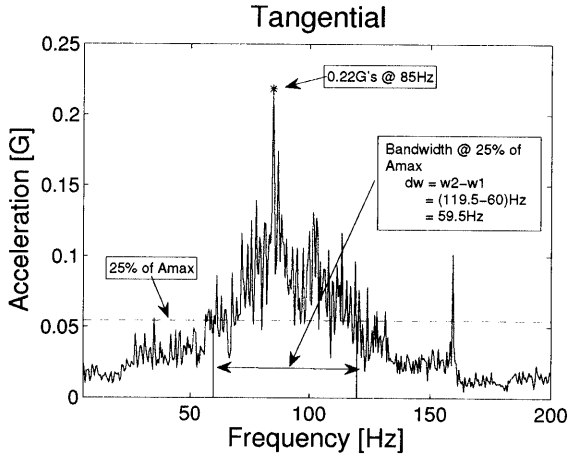

Figure 2-7: *Tangential Acceleration as a function of frequency. The plot is produced by Fourier transforming all five trials and then averaging the transforms. The frequency based acceleration does show a significant acceleration peak of 0.22 G's at a frequency of 85Hz; however, the acceleration amplitude is also relatively broad-band. The dotted red line illustrates that the band-width of acceleration that is greater than 25% of the maximum amplitude is approximately 60Hz.*

maximum frequency and bandwidth.

If the input vibration is not stationary, then the frequency components obtained from a Fourier transform of the entire data set are not accurate. In this instance the input vibration might be entirely random, or it is possible the input is harmonic but that the frequency of vibration wanders in time. In order to determine this, a spectrogram is used. A spectrogram is a plot of the Fourier transform of a windowed and zero padded section of the data where the widow is slid in time. Thus, the spectrogram shows the change in frequency components as a function of time. A non-stationary harmonic vibration will have a spectrogram like that shown in Fig. 2-8

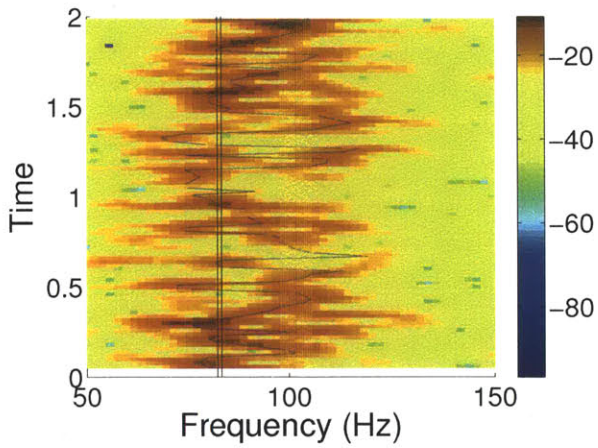

Figure 2-8: *Spectrogram of the gyroscopic data show in Fig. 1-7*

2.4 Transduction Types

Several methods exist to transduce kinetic energy into electric energy. The methodologies broadly fit into one of two categories, active materials or electro-dynamics. Active materials convert the kinetic energy into strain energy, and the strain in the active material produce an electric potential. Both piezo-electric materials and magneto-strictive materials produce this effect and both have been used in energy harvesters [2, 18, 5, 29]. In addition to the functional requirements on temperature, Arnold [3]

and Mitcheson et. al [19] have both shown that for active materials have higher energy densities for small micro-scale devices, but for macro-scale devices electro-dynamic harvesters have larger energy densities. Since the prototype harvester presented in this thesis is macro scale, and the temperatures do not support active materials, this thesis focuses on Electro-dynamic harvesters.

Electro-dynamic harvesters use the relative displacement between the inertial proof mass to and the vibrating source to produce changes in either electric or magnetic fields. The harvesting methodologies can broadly be classified as either velocity-damped (magnetic field), or coulomb-damped (electric field)[18]. Due to the relative magnitude of electric and magnetic fields, electro-static [17] harvesters are better suited to micro scale devices, and electromagnetic [3] harvesters are better suited to macro devices. Again, since the functional requirements for form factor for this work are macro scale, this thesis focuses on electro-magnetic conversion methods.

Chapter 3

Harvesting Architectures

The true challenge to wide scale success of vibration energy harvesting is harvesting from wide-band vibrations. [11]. Most ambient vibrations are not harmonic and thus the energy in the vibration is spread across many frequencies or is completely random without frequency content [9]. Efficiently harvesting energy from these vibrations is difficult [10, 11].

Several architectures are proposed as possible solutions to harvesting energy from wide-band width vibration sources. First, a resonant harvester is explained and it performance when excited by wide-band vibration inputs is analytically evaluated. The wide-band harvester is used as a baseline for evaluating different architectures. Second, "Farm" systems, which consist of an array of resonant harvester tuned to a series of different resonant frequencies, is evaluated and compared against a resonant harvester. Third, optimal control theory is used to evaluate the effectiveness of adding a control loop to increase the harvesting efficiency of resonant harvesters. Fourth, alternate non-resonant architectures designed to rectify the vibration input are evaluated. In general, rectifiers are typically coupled with a resonant harvester and are designed to condition the vibration input for the resonant harvester, which can potentially increase resonant amplification of the vibration input and thus the energy harvested.

3.1 Resonant Harvester

Extracting energy from a given vibration is the same as damping the vibration. One well known method of damping a vibration is by attaching a spring-mass-damper system to the vibrating surface. Some of the kinetic energy of the vibrating surface is dissipated by the damper and is thus extracted from the vibrating surface. This section presents a method for examining the maximum amount of power that can be extracted from an input vibration. The estimate is independent of the method of extracting energy, but does require the system elements to be estimable as linear.

3.1.1 Spring-Mass-Damper Solution

As a first order estimation of the extractable power in a given vibration, consider a simple spring-mass-damper system, with linear elements, subjected to base excitation (Fig. 3-1). The governing differential equation for this type of system is derived by

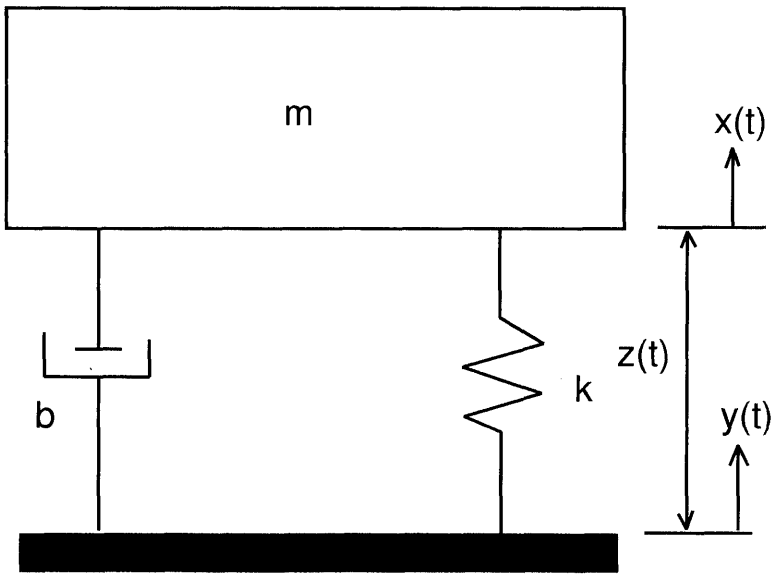

Figure 3-1: *Standard Base Excitation Model*

equating forces acting on the vibrating mass (figure 3-15). Summation of forces in the vertical direction results in equation 3.1.1,

$$F_a(t) + F_b(t) + F_k(t) = 0$$

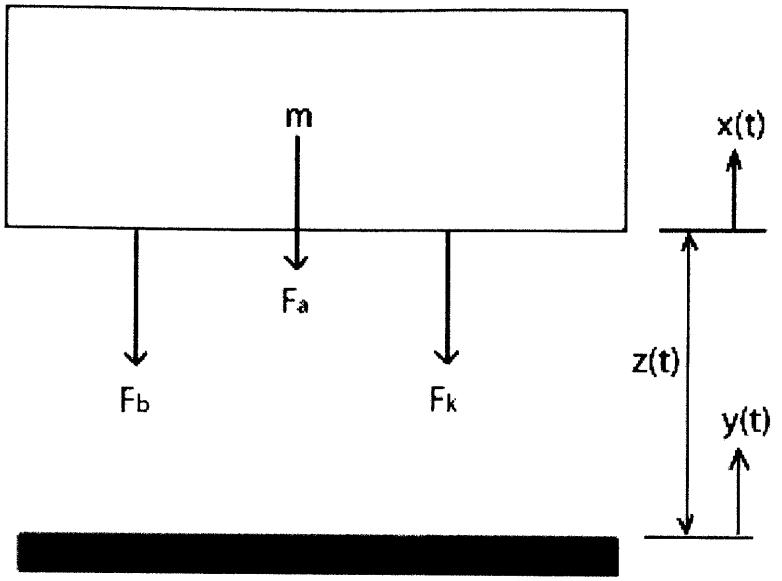

Figure 3-2: *Free Body Diagram of the vibrating mass associated with the simple spring-mass-damper system. Where* $F_a = m\ddot{x}$, $F_b = b(\dot{x} - \dot{y})$, *and* $F_k = k(x - y)$

To obtain a *solvable* differential equation that characterizes the motion of the moving mass, each of the elements is assumed to be *linear* and *proportional* to either the relative displacement or relative velocity of the moving mass,

$$\begin{aligned} F_k(t) &= k\,(x(t) - y(t)) \\ F_b(t) &= b\,(\dot{x}(t) - \dot{y}(t)) \end{aligned}$$

Substitution of the given force relationships into equation 3.1.1 results in the governing differential equation for the spring-mass-damper system[?],

$$m\ddot{x} + b(\dot{x} - \dot{y}) + k(x - y) = 0$$

By noticing that the relative displacement, z, can be represented as the difference between absolute displacements of the mass and the vibrating surface, $z = x - y$, equation 3.1.1 can be represented in terms of relative displacement as,

$$m\ddot{z} + b\dot{z} + kz = -m\ddot{y}$$

Performing the Laplace transform on equation 3.1.1 (assuming $z(t)$ and $y(t)$ are both 0 for $t < 0$) yields,

$$(ms^2 + bs + k)Z(s) = -ms^2Y(s)$$

from which can be seen the transfer function $H(s)$,

$$H(s) = \frac{Z(s)}{Y(s)} = \frac{-ms^2}{ms^2 + bs + k} \tag{3.1}$$

and substituting $s = j\omega$ to return to the frequency domain yields,

$$H(\omega) = \frac{m\omega^2}{(k - m\omega^2) + b\omega j} \tag{3.2}$$

Dividing through by the mass, and substituting the common relationships,

$$\begin{cases} \omega_n^2 = k/m \\ \zeta = b/2m\omega_n \end{cases}$$

The transfer function can be written as,

$$H(\omega) = \frac{\omega^2}{(\omega_n^2 - \omega^2) + 2\zeta\omega_n\omega j}$$

Finally, dividing through by the natural frequency and introducing the *frequency ratio*, $r = \omega/\omega_n$, the transfer function can be written as a function of two variables, r and ζ,

$$H(r, \zeta) = \frac{r^2}{(1 - r^2) + 2\zeta r j} \tag{3.3}$$

Thus, the steady state solution to the differential equation governing relative displacement, $z(t)$, as a function of base excitation, $y(t)$, (equation 3.1.1) can be written as,

$$z(t) = H(r, \zeta)y(t) \tag{3.4}$$

Since $H(r,\zeta)$ is time invariant, the same solution applies to time derivatives of $z(t)$ and $y(t)$,

$$\dot{z}(t) = H(r,\zeta)\dot{y}(t) \tag{3.5}$$

$$\ddot{z}(t) = H(r,\zeta)\ddot{y}(t) \tag{3.6}$$

This solution method is only applicable if $y(t)$ is a harmonic function. However, if an arbitrary input is decomposed in the frequency domain and represented as a fourier series of harmonic functions, then the solution can be extended to any arbitrary input.

3.1.2 Power

Inspection of figure 3-1 shows that the only dissipative element in the system is the damper. Thus, the extractable power in the system is related to the power dissipated by the damper. The instantaneous power dissipated by the damper can be represented as,

$$P(t) = F(t)V(t)$$

In the derivation of the governing differential equation (figure 3-15), the force exerted by the damper was assumed to be linearly proportional to the relative velocity, $F_b = b\dot{z}$. Thus the power can be represented as,

$$P(t) = b\dot{z}^2(t) \tag{3.7}$$

By combining the steady state solutions of the governing differential equation (equations 3.4 through 3.6) and the above expression for power (equation 3.7), the instantaneous expression for power can be represented as a function of a variety of inputs. Since the input provided as a design parameter is the amplitude of acceleration as a function of frequency, the power equation is represented in terms of the base acceleration, $\ddot{y}(t)$ (transformation to different known inputs will simply involve powers of $s = j\omega$). To represent the power as a function of $\ddot{y}(t)$, perform the Inverse Laplace transform on $\dot{z}(t)$, substitute the resulting expression for $\ddot{z}(t)$ into equation 3.6, and

substitute the subsequent equation into equation 3.7. The resulting expression for power is,

$$P(t) = \frac{-b}{\omega^2} H^2(r,\zeta)\ddot{y}^2(t) \tag{3.8}$$

To simplify algebraic manipulations, $H(r,\zeta)$ can be represented in exponential form,

$$\begin{aligned} H(r,\zeta) &= \frac{r^2}{\sqrt{(1-r^2)^2+(2\zeta r)^2}} e^{-j\phi} \\ \text{where } \phi &= \arctan\frac{2\zeta r}{1-r^2} \end{aligned} \tag{3.9}$$

Substituting this expression for $H(r,\zeta)$ and the relation $\omega = \omega_n r$ into equation 3.8, the dissipated power can be written as,

$$P(t) = \frac{-br^2}{\omega_n^2[(1-r^2)^2+(2\zeta r)^2]} e^{-j2\phi}\ddot{y}^2(t) \tag{3.10}$$

Examination of equation 3.10 shows that the instantaneous power dissipated by the damper can be represented by a transfer function relating the base acceleration squared to power, $G_{\ddot{y}^2|P}$.

$$\begin{aligned} G_{\ddot{y}^2|P} &= \frac{-br^2}{\omega_n^2[(1-r^2)^2+(2\zeta r)^2]} e^{-j2\phi} \\ &= \frac{br^2}{\omega_n^2[(1-r^2)^2+(2\zeta r)^2]} e^{-j2(\phi+\pi/2)} \end{aligned} \tag{3.11}$$

The average power dissipated by the damper over a given time frame $(0 \rightarrow T)$ is the time average of the instantaneous power over that same time frame,

$$\begin{aligned} P_{avg} &= \frac{1}{T}\int_0^T P(t)dt \\ &= \frac{1}{T}\int_0^T G_{\ddot{y}^2|P}\ddot{y}^2(t)dt \end{aligned}$$

Since $G_{\ddot{y}^2|P}$ is time invariant, the average power can be simplified to,

$$P_{avg} = G_{\ddot{y}^2|P}\frac{1}{T}\int_0^T \ddot{y}^2(t)dt \tag{3.12}$$

Recall that the use of a frequency-based transfer function solution requires the input acceleration as a function of time be represented as a sum of harmonic functions over the entire frequency range,

$$\ddot{y}(t) = \sum_{i=0}^{\infty} A_i \sin(\omega_i t - \alpha_i)$$

Performing an integration of the square of a series of sines is possible in discrete numerical simulations, but difficult to reduce into a closed form. To further refine the first order estimate of the maximum average output power, begin by examining the transfer function $G_{\ddot{y}^2|P}$. Figure 3-3 is a plot of the magnitude and phase of $\omega_n^2/b|G_{\ddot{y}^2|P}|$ as a function of r for various ζ. As can be seen, $G_{\ddot{y}^2|P}$ acts like a narrow band-pass

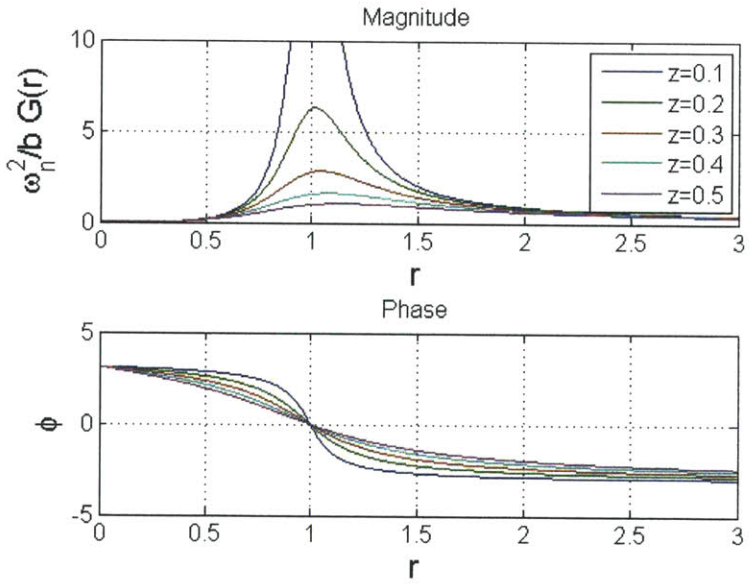

Figure 3-3: *Magnitude and phase of* $G_{\ddot{y}^2|P}$

filter. Thus, only components of vibration that are within the narrow band-pass frequency range contribute significantly to the power. A conservative estimate of the maximum average output power is obtained by using this band-pass property. By considering only the value of acceleration at the frequency which corresponds to the

maximum value of $|G_{\ddot{y}^2|P}|$, $\ddot{y}(t)$ can be simplified to,

$$\ddot{y}(t) = A_G \sin \omega_G t$$

where the subscript G represents the spectral values at the frequency corresponding to the peak value of $|G_{\ddot{y}^2|P}|$. Given this simplification, the time average of the input acceleration squared is simply the time average of a single harmonic function squared, which is 1/2 the amplitude squared, thus a conservative average power can be estimated as,

$$P_{avg\ max} = \left|G_{\ddot{y}^2|P}\right| \frac{A_G^2}{2} \tag{3.13}$$

Assuming that the input base acceleration is known and unchangeable, equation 3.13 indicates that the maximum power is obtained by maximizing the transfer function $|G_{\ddot{y}^2|P}|$. Figure 3-3 shows that $|G_{\ddot{y}^2|P}|$ has a definite maximum in the vicinity of $r = 1$. The exact location of the maximum is determined by differentiating $|G_{\ddot{y}^2|P}|$ with respect to r and setting the result equal to 0,

$$\frac{\partial \left|G_{\ddot{y}^2|P}\right|}{\partial r} = \frac{-2br(r^4 - 1)}{\omega_n^2 \left(1 - 2r^2 + r^4 + (2\zeta r)^2\right)^2} = 0$$

Which has solutions, $r = 0, \pm 1, \pm j$. Since r must be real and positive, $r = 0$ and $r = 1$ are the only valid solutions. Figure 3-3 shows that $r = 0$ is a minimum, thus $|G_{\ddot{y}^2|P}|_{max}$ occurs at r=1 and can be simplified to,

$$\left|G_{\ddot{y}^2|P}\right|_{max} = \frac{b}{4\omega_n^2 \zeta^2} \tag{3.14}$$

Substituting in $\zeta = b/2m\omega_n$, equation 3.14 can be further reduced to,

$$\left|G_{\ddot{y}^2|P}\right|_{max} = \frac{m^2}{b} \tag{3.15}$$

The maximum power dissipated can then be represented by,

$$P_{max} = \frac{m^2 A_n^2}{2b} \tag{3.16}$$

Harmonic Excitation

As a sanity check, assume the base excitation is a pure harmonic input of the form,

$$\begin{aligned} y(t) &= y_0 \sin \omega t \\ \dot{y}(t) &= y_0 \omega \cos \omega t \\ \ddot{y}(t) &= -y_0 \omega^2 \sin \omega t \end{aligned}$$

Thus, substituting into equation 3.12 and integrating over one cycle, the maximum power can be written as,

$$\begin{aligned} P_{max} &= \left|G_{\ddot{y}^2|P}\right| \frac{1}{T} \int_0^T \left(-y_0 \omega^2 \sin\left(\omega_n t\right)\right)^2 dt \\ &= \frac{b r^2 \left(y_0 \omega^2\right)^2}{2\omega_n^2 [(1-r^2)^2 + (2\zeta r)^2]} \end{aligned} \tag{3.17}$$

Since equation 3.17 agrees with the expression for dissipated power of a harmonically excited spring-mass-damper system presented by Kausel and Roësset[?], the solution is collaborated to some extent. Additionally, if the input frequency is assumed to equal the natural frequency of the spring and mass, $r = 1$, then equation 3.17 reduces to,

$$P_{max} = \frac{m^2 \left(y_0 \omega^2\right)^2}{2b} = \frac{m^2 A_n^2}{2b} \tag{3.18}$$

which matches equation 3.16.

3.1.3 Damping

Figure 3-1 represents the damping in the system as a single dashpot. However, as mentioned, the damping coefficient is a linear combination of the inherent mechanical damping of the spring element and the external damping caused by extraction of energy. Each damping element acts independently on the mass and thus the total composite dashpot is modeled as two separate dashpots in parallel (figure 3-4). The

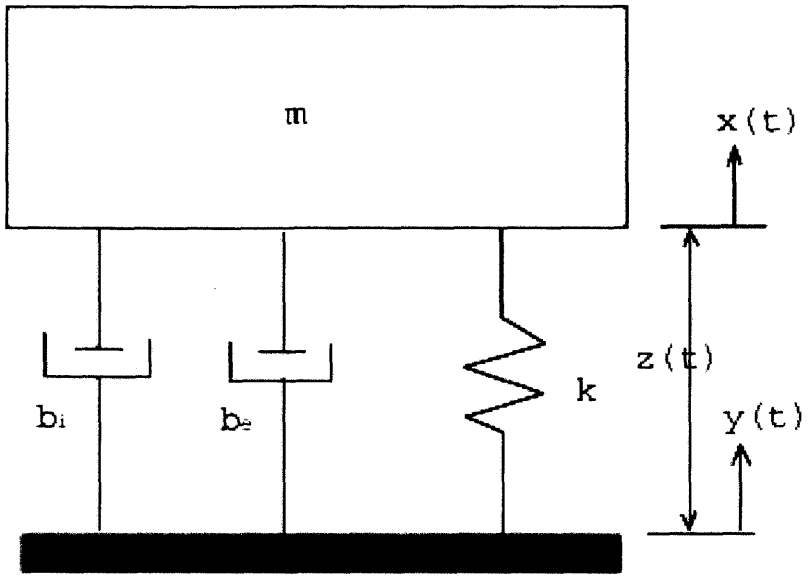

Figure 3-4: *Model of System Damping*

total damping coefficient is therefore the sum of the component damping coefficients,

$$b = b_{internal} + b_{external}$$

Thus the total power dissipated at resonance is,

$$P = \frac{m^2}{b_i + b_e} \frac{A_n^2}{2} \tag{3.19}$$

However, only the power dissipated in the external damper b_e is harvested. To determine the power dissipated in the external damper, substitute $\zeta = (b_i + b_e)/(2m\omega_n)$ into equation 3.14,

$$P_e = \frac{m^2 b_e A_n^2}{(b_i + b_e)^2} \tag{3.20}$$

Figure 3-5 is a plot of the proportional power as a function of b_e/b_i. Notice that the power definitely peaks in the vicinity of $b_e = b_i$. To determine the exact relationship between external and internal damping that maximizes the useful extracted power,

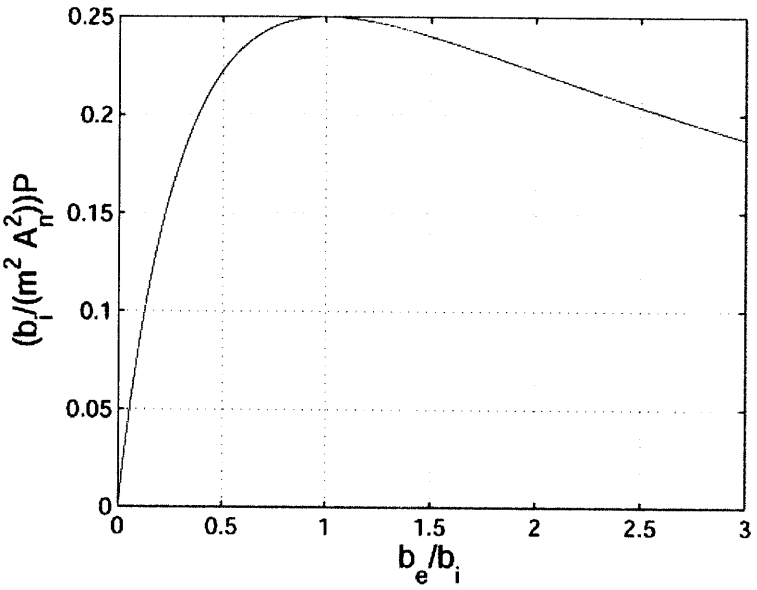

Figure 3-5: *Proportional Power vs.* b_e/b_i

differentiate equation 3.20 with respect to b_e and set the result equal to 0.

$$\frac{dP_e}{db_e} = m^2 A_n^2 \frac{b_i - b_e}{(b_i + b_e)^3} = 0 \tag{3.21}$$

Neither the mass nor the time average of the acceleration is zero so the solution is $b_e = b_i$, and the maximum power is,

$$P_{e\ max} = \frac{m^2 A_n^2}{4b_i} \tag{3.22}$$

Thus, the maximum amount of power that can be extracted out of a linear external damping element given a fixed base acceleration input is proportional to the square of the mass and inversely proportional to the internal damping in the system.

3.1.4 Conclusions

One simple method to characterize the internal damping in a spring-mass system is through an amplification factor, Q, defined as $Q_i = 1/2\zeta_i$. The maximum power estimate can be represented in terms of the internal amplification factor by replacing b_i with $2\zeta_i\omega_n m$ in equation 3.22.

$$P_{e\ max} = \frac{mQ_iA_n^2}{4\omega_n} \tag{3.23}$$

Thus, the power will scale linearly with mass and amplification factor, and inversely with natural frequency. Figure 3-13 is a plot of $P \cdot (\omega_n/mQ_i)$ vs. A_n.

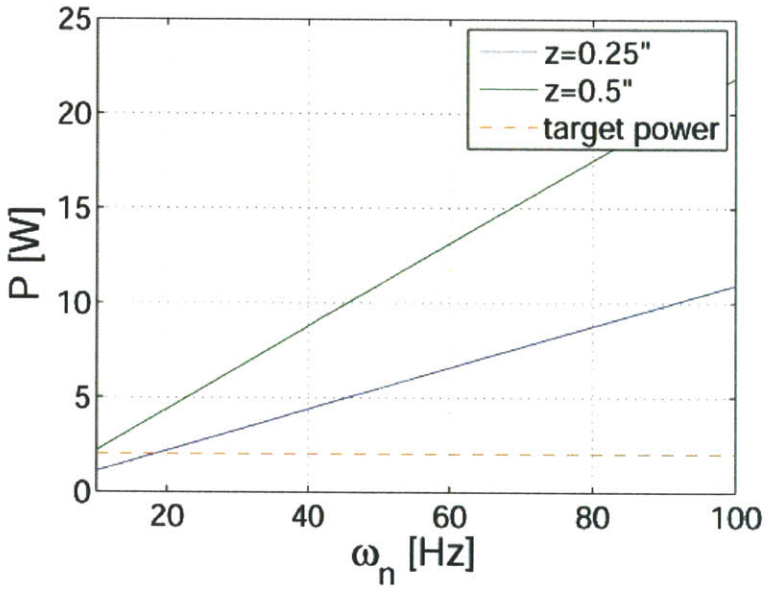

Figure 3-6: $P \cdot (\omega_n/mQ_i)$ *vs.* A_n.

The magnitude of acceleration is assumed known and the spectral representation of the assumed acceleration values is shown in figure 3-7. Based on the assumed values of $A(\omega)$ and an assumed amplification factor of 100, figure 3-8 predicts the maximum output power as a function of frequency. For the given assumptions, the maximum extractable power is $\approx 9W/kg_{of\ moving\ mass}$.

It seems counter intuitive for power to scale inversely with natural frequency.

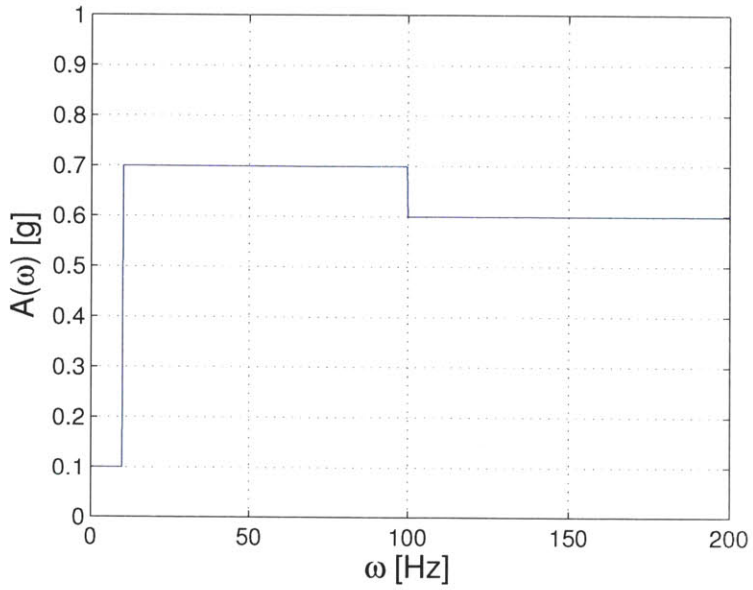

Figure 3-7: *Assumed Sinusoidal Amplitude, $A(\omega)$ as a function of Frequency, ω.*

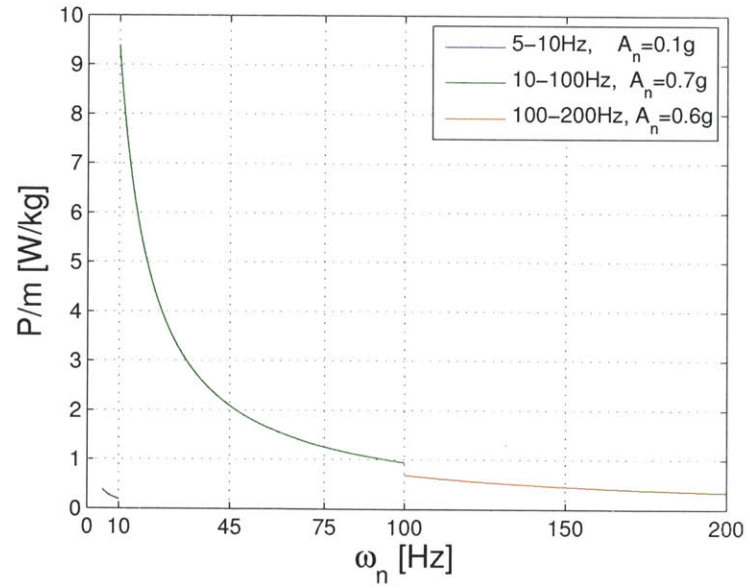

Figure 3-8: *Estimated Maximum Power (P) as a function of Frequency (ω)*

However, recall that the invariant input is assumed to be acceleration. Thus, for the same acceleration, a lower natural frequency will equate to a larger displacement input or equivalently a larger velocity in the damper and thus more power.

Additionally, the derivation assumes the base acceleration is invariant. As long as the inertia of the base is significantly higher than the inertia of the mass, then the forces transmitted to the base will not affect the accelerations of the base. If the device is connected to a drill string, then any amount of mass that would fit in the given size envelope will not significantly change the vibration of the pipe.

3.2 Farm Systems

An array of resonant harvester each tuned to a slightly different frequency and covering the frequency spectrum is often proposed as a solution to wide band excitation [27, ?]. However, there are two problems with this approach. First, if the input is stochastic then the signal actually does not contain pure frequency components and none of the harvesters will resonant. Thus, none of the harvesters will produce energy. Second, even if the input is stationary, a device must fit within a fixed volume. Thus, the total amount of inertial mass is limited and must be distributed amongst the harvesters. The following section shows that in a stationary input, limited mass case, it is best to put all the mass at the frequency component with the greatest energy.

3.2.1 Baseline

Consider the standard 2nd-order spring-mass-damper base excitation model,

$$\ddot{x} + \frac{b_i + b_e}{m}\dot{x} + \frac{K}{m}x = -\ddot{y} \tag{3.24}$$

Starting with a single harmonic input,

$$\ddot{y} = A_1 \cos\left(\omega_1 t - \phi_1\right) = \Re\left[A_1 e^{j(\omega_1 t - \phi_1)}\right] \tag{3.25}$$

Focusing on the particular or steady-state solution x_p, assume

$$\begin{aligned} x_p(t) &= \Re\left[Be^{j(\omega_1 t-\phi_1)}\right] && (3.26)\\ \dot{x}_p(t) &= \Re\left[B\omega_1 je^{j(\omega_1 t-\phi_1)}\right] && (3.27)\\ \ddot{x}_p(t) &= \Re\left[-B\omega_1^2 e^{j(\omega_1 t-\phi_1)}\right] && (3.28) \end{aligned}$$

Plugging into the differential equation

$$-B\omega_1^2 e^{j(\omega_1 t-\phi_1)} + \frac{b_i+b_e}{m}B\omega_1 je^{j(\omega_1 t-\phi_1)} + \frac{K}{m}Be^{j(\omega_1 t-\phi_1)} = -A_1 e^{j(\omega_1 t-\phi_1)} \quad (3.29)$$

And solving for B results in the particular solution,

$$\begin{aligned} x_p(t) &= \Re\left[\frac{-A_1}{\left(\frac{K}{m}-\omega_1^2\right)+\left(\frac{b_i+b_e}{m}\right)\omega_1 i}e^{j(\omega_1 t-\phi_1)}\right]\\ &= \Re\left[\frac{-A_1}{\sqrt{\left(\frac{K}{m}-\omega_1^2\right)^2+\left(\frac{b_i+b_e}{m}\right)^2\omega_1^2}}e^{j(\omega_1 t-\phi_1-\psi)}\right]\\ &= \frac{-A_1}{\sqrt{\left(\frac{K}{m}-\omega_1^2\right)^2+\left(\frac{b_i+b_e}{m}\right)^2\omega_1^2}}\cos\left(\omega_1 t-\phi_1-\psi\right) && (3.30) \end{aligned}$$

Where,

$$\psi = \tan^{-1}\left(\frac{\left(\frac{b_i+b_e}{m}\right)\omega_1}{\frac{K}{m}-\omega_1^2}\right) \quad (3.31)$$

The power is then,

$$\begin{aligned} P &= \left(b_e\dot{x}\right)\dot{x}\\ &= b_e\dot{x}^2\\ &= b_e\left[\frac{A_1\omega_1}{\sqrt{\left(\frac{K}{m}-\omega_1^2\right)^2+\left(\frac{b_i+b_e}{m}\right)^2\omega_1^2}}\sin\left(\omega_1 t-\phi_1-\psi\right)\right]^2\\ &= \frac{b_e A_1^2\omega_1^2}{\left(\frac{K}{m}-\omega_1^2\right)^2+\left(\frac{b_i+b_e}{m}\right)^2\omega_1^2}\sin^2\left(\omega_1 t-\phi_1-\psi\right) && (3.32) \end{aligned}$$

Averageing power over an infinite time horizon,

$$\begin{aligned}
\bar{P} &= \lim_{T\to\infty}\left[\frac{1}{T}\int_{t=0}^{T} \frac{b_e A_1^2\omega_1^2}{\left(\frac{K}{m}-\omega_1^2\right)^2+\left(\frac{b_i+b_e}{m}\right)^2\omega_1^2}\sin^2\left(\omega_1 t-\phi_1-\psi\right)\quad dt\right] \\
&= \frac{b_e A_1^2\omega_1^2}{\left(\frac{K}{m}-\omega_1^2\right)^2+\left(\frac{b_i+b_e}{m}\right)^2\omega_1^2}\quad \lim_{T\to\infty}\left[\frac{1}{T}\int_{t=0}^{T} \sin^2\left(\omega_1 t-\phi_1-\psi\right)\quad dt\right] \\
&= \frac{b_e A_1^2\omega_1^2}{\left(\frac{K}{m}-\omega_1^2\right)^2+\left(\frac{b_i+b_e}{m}\right)^2\omega_1^2}\quad \left(\frac{1}{2}\right) \\
&= \frac{b_e A_1^2\omega_1^2}{2\left[\left(\frac{K}{m}-\omega_1^2\right)^2+\left(\frac{b_i+b_e}{m}\right)^2\omega_1^2\right]} \\
&= \frac{b_e A_1^2}{2\left[\left(\frac{K}{m\omega_1}-\omega_1\right)^2+\left(\frac{b_i+b_e}{m}\right)^2\right]}
\end{aligned} \tag{3.33}$$

Since all the terms in the denominator are squared and thus positive, the maximum of $\bar{P}(k)$ occurs when,

$$\left(\frac{K}{m\omega_1}-\omega_1\right)=0\rightarrow\frac{K}{m}=\omega_1^2 \tag{3.34}$$

Which is the same as saying the natural frequency of the system should be matched to the forcing frequency. The maximum average power is then,

$$\bar{P}_{max}=\frac{b_e A_1^2}{2\left(\frac{b_i+b_e}{m}\right)^2} \tag{3.35}$$

Differentiating with respect to b_e and setting equal to zero as done previously reveals that to maximize $\bar{P}$; $\quad b_e=b_i$. Thus,

$$\bar{P}_{max}=\frac{b_i A_1^2}{2\left(\frac{2b_i}{m}\right)^2}=\frac{m^2A_1^2}{8b_i} \tag{3.36}$$

If we imagine a farm system where each device and input is completely independent, but the total mass m must be split among the devices into a percentage p of the total mass allocated to maximize power from the frequency ω_1, and the remaining mass $(1-p)\,m$ allocated to optimize power from the frequency ω_2, then the maximum

average power is,

$$\bar{P}_{max_{iid}} = \frac{1}{8b_i}\left((pm)^2 A_1^2 + ((1-p)m)^2 A_2^2\right) \tag{3.37}$$

To determine the best allocation, we maximize with respect to p

$$\frac{d\bar{P}_{max_{iid}}}{dp} = 2pm^2 A_1^2 - 2(1-p)m^2 A_2^2 = 0 \tag{3.38}$$

Thus the maximum is one of,

$$\left[\bar{P}_{max_{iid}}\right]_{max_p} = \begin{cases} \frac{m^2 A_1^2}{8b_i} & p = 1 \\ \frac{m^2}{8b_i}\frac{A_1^2 A_2^2}{A_1^2 + A_2^2} & p = \frac{A_2^2}{A_1^2 + A_2^2} \\ \frac{m^2 A_2^2}{8b_i} & p = 0 \end{cases} \tag{3.39}$$

The maximum is one of the end points. Assuming $A_1 > A_2$, clearly $p = 1$ is better than $p = 0$, thus, under these simplifying assumptions it is better to provide all the mass to the frequency with highest acceleration amplitude.

3.2.2 Two frequency input

In the first estimate, we ignored the fact that off resonance frequency signals would affect the velocity and thus the power. If we now let $\ddot{y}$ be a harmonic input of 2 different frequencies,

$$\ddot{y} = A_1 \cos(\omega_1 t - \phi_1) + A_2 \cos(\omega_2 t - \phi_2) = \Re\left[A_1 e^{j(\omega_1 t - \phi_1)}\right] + \Re\left[A_2 e^{j(\omega_2 t - \phi_2)}\right] \tag{3.40}$$

Applying superpostion,

$$x_p(t) = -\acute{A}_1 \cos(\omega_1 t - \phi_1 - \psi_1) - \acute{A}_2 \cos(\omega_2 t - \phi_2 - \psi_2) \tag{3.41}$$

Where,

$$\acute{A}_1 = \frac{A_1}{\sqrt{\left(\frac{K}{m}-\omega_1^2\right)^2+\left(\frac{b_i+b_e}{m}\omega_1\right)^2}} \tag{3.42}$$

$$\acute{A}_2 = \frac{A_2}{\sqrt{\left(\frac{K}{m}-\omega_2^2\right)^2+\left(\frac{b_i+b_e}{m}\omega_2\right)^2}} \tag{3.43}$$

$$\psi_1 = \tan^{-1}\left(\frac{\left(\frac{b_i+b_e}{m}\right)\omega_1}{\frac{K}{m}-\omega_1^2}\right) \tag{3.44}$$

$$\psi_2 = \tan^{-1}\left(\frac{\left(\frac{b_i+b_e}{m}\right)\omega_2}{\frac{K}{m}-\omega_2^2}\right) \tag{3.45}$$

Once again calculating the power,

$$\begin{aligned} P &= b_e\left(\acute{A}_1\omega_1\sin\left(\omega_1 t-\phi_1-\psi_1\right)+\acute{A}_2\omega_2\sin\left(\omega_2 t-\phi_2-\psi_2\right)\right)^2 \\ &= b_e\Big(\acute{A}_1{}^2\omega_1^2\sin^2\left(\omega_1 t-\phi_1-\psi_1\right) \\ &\quad +2\acute{A}_1\omega_1\acute{A}_2\omega_2\sin\left(\omega_1 t-\phi_1-\psi_1\right)\sin\left(\omega_2 t-\phi_2-\psi_2\right) \\ &\quad +\acute{A}_2{}^2\omega_2^2\sin^2\left(\omega_2 t-\phi_2-\psi_2\right)\Big) \end{aligned} \tag{3.46}$$

Again we average this over the infinite time horizon.

$$\begin{aligned} \bar{P} &= \lim_{T\to\infty}\left[\frac{1}{T}\int_{t=0}^{T} b_e\Big(\acute{A}_1{}^2\omega_1^2\sin^2\left(\omega_1 t-\phi_1-\psi_1\right)\right. \\ &\quad +2\acute{A}_1\omega_1\acute{A}_2\omega_2\sin\left(\omega_1 t-\phi_1-\psi_1\right)\sin\left(\omega_2 t-\phi_2-\psi_2\right) \\ &\quad \left.+\acute{A}_2{}^2\omega_2^2\sin^2\left(\omega_2 t-\phi_2-\psi_2\right)\Big)\quad dt\right] \\ &= \frac{b_e}{2}\left(\acute{A}_1^2\omega_1^2+\acute{A}_2^2\omega_2^2\right) \\ &= \frac{b_e}{2}\left(\frac{A_1^2\omega_1^2}{\left(\frac{K}{m}-\omega_1^2\right)^2+\left(\frac{b_i+b_e}{m}\omega_1\right)^2}+\frac{A_2^2\omega_2^2}{\left(\frac{K}{m}-\omega_2^2\right)^2+\left(\frac{b_i+b_e}{m}\omega_2\right)^2}\right) \\ &= \frac{b_e}{2}\left(\frac{A_1^2}{\left(\frac{K}{m\omega_1}-\omega_1\right)^2+\left(\frac{b_i+b_e}{m}\right)^2}+\frac{A_2^2}{\left(\frac{K}{m\omega_2}-\omega_2\right)^2+\left(\frac{b_i+b_e}{m}\right)^2}\right) \end{aligned} \tag{3.47}$$

One Device

To determine the optimal set of parameters to optimize power output for one device, assume that mass if fixed and start by optimizing over K,

$$\frac{d\bar{P}}{dK} = 0 \quad = \quad -\frac{b_e}{m}\left(\frac{A_1^2\left(\frac{K}{m\omega_1}-\omega_1\right)}{\omega_1\left(\left(\frac{K}{m\omega_1}-\omega_1\right)^2+\left(\frac{b_i+b_e}{m}\right)^2\right)^2}+\frac{A_2^2\left(\frac{K}{m\omega_2}-\omega_2\right)}{\omega_2\left(\left(\frac{K}{m\omega_2}-\omega_2\right)^2+\left(\frac{b_i+b_e}{m}\right)^2\right)^2}\right) \tag{3.48}$$

This is not solvable analytically. For reasonable numerical values, graphically we see that the natural frequency of the system should match one of the input frequencies for some minimum spread between the frequencies and should be some intermediate value for spreads lesser spreads (figure 3-9). Dealing first with the case where the

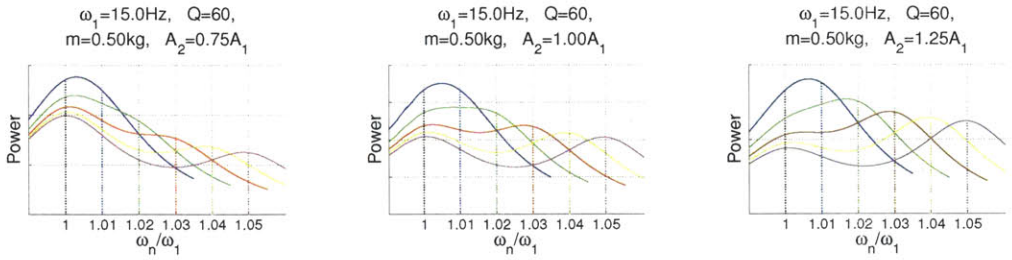

(a) (b) (c)

Figure 3-9: *Maximum power vs natural frequency*

spread in the frequencies is large enough that the maximum occurs at one of the input frequencies.

$$\bar{P}_{max} \quad = \quad \max\left[\begin{array}{ll} \frac{b_e}{2}\left(\frac{A_1^2\omega_1^2}{\left(\frac{b_i+b_e}{m}\omega_1\right)^2}+\frac{A_2^2\omega_2^2}{\left(\omega_1^2-\omega_2^2\right)^2+\left(\frac{b_i+b_e}{m}\omega_2\right)^2}\right) & , \quad \frac{K}{m}=\omega_1^2 \\ \\ \frac{b_e}{2}\left(\frac{A_1^2\omega_1^2}{\left(\omega_1^2-\omega_2^2\right)^2+\left(\frac{b_i+b_e}{m}\omega_1\right)^2}+\frac{A_2^2\omega_2^2}{\left(\frac{b_i+b_e}{m}\omega_2\right)^2}\right) & , \quad \frac{K}{m}=\omega_2^2 \end{array}\right] \tag{3.49}$$

Solving the first for A_1^2 and the second for A_2^2

$$A_1^2 = \frac{b_i + b_e}{m}\left[\frac{2\bar{P}_1}{b_e} - \frac{A_2^2\omega_2^2}{\left(\omega_1^2 - \omega_2^2\right)^2 + \left(\frac{b_i+b_e}{m}\omega_2\right)^2}\right] \tag{3.50}$$

$$A_2^2 = \frac{b_i + b_e}{m}\left[\frac{2\bar{P}_2}{b_e} - \frac{A_1^2\omega_1^2}{\left(\omega_1^2 - \omega_2^2\right)^2 + \left(\frac{b_i+b_e}{m}\omega_1\right)^2}\right] \tag{3.51}$$

Assuming $A_1 > A_2$,

$$\begin{aligned}
A_1 &\geq A_2 \\
A_1^2 &\geq A_2^2 \qquad (3.52)\\
\frac{b}{m}\left[\frac{2\bar{P}_1}{b_e} - \frac{A_2^2\omega_2^2}{\left(\omega_1^2 - \omega_2^2\right)^2 + \left(\frac{b}{m}\omega_2\right)^2}\right] &\geq \frac{b}{m}\left[\frac{2\bar{P}_2}{b_e} - \frac{A_1^2\omega_1^2}{\left(\omega_1^2 - \omega_2^2\right)^2 + \left(\frac{b}{m}\omega_1\right)^2}\right] \\
\frac{2\bar{P}_1}{b_e} - \frac{A_2^2\omega_2^2}{\left(\omega_1^2 - \omega_2^2\right)^2 + \left(\frac{b}{m}\omega_2\right)^2} &\geq \frac{2\bar{P}_2}{b_e} - \frac{A_1^2\omega_1^2}{\left(\omega_1^2 - \omega_2^2\right)^2 + \left(\frac{b}{m}\omega_1\right)^2} \\
\frac{2}{b_e}\left(\bar{P}_1 - \bar{P}_2\right) &\geq \frac{A_2^2\omega_2^2}{\left(\omega_1^2 - \omega_2^2\right)^2 + \left(\frac{b}{m}\omega_2\right)^2} - \frac{A_1^2\omega_1^2}{\left(\omega_1^2 - \omega_2^2\right)^2 + \left(\frac{b}{m}\omega_1\right)^2} \qquad (3.53)
\end{aligned}$$

If the power harvested when the harvester is tuned to the first resonant frequency is greater than the power harvested when tuned to the second resonant frequency, which shows that all the mass should be placed on the peak with the most energy.

3.2.3 Both Move

A variant of the farm idea is to have both the magnets and the coils move; both as independent tuned-mass dampers where the harvested energy is extracted with respect to relative motion between the magnets (mass) and coils (Fig. 3-10). The variables need to describe the motion and the power in this system are:

- COORDINATES

  x_m = absolute displacement of the magnets

  x_c = absolute displacement of the coils

  y = absolute displacement of the ground input

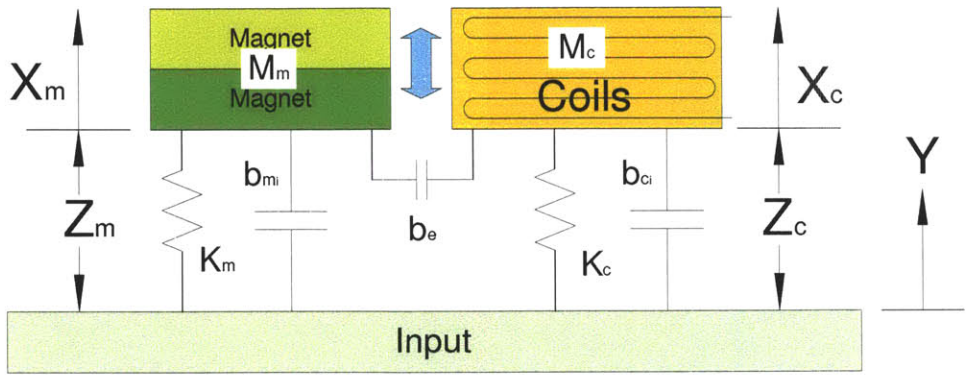

Figure 3-10: *Schematic semi-lumped parameter model of planar 2-dof induction harvester. This is meant to model an induction harvester where the magnets and coils are allowed to move separately in plane but are constrained to move in a single plane.*

$z_m = x_m - y$ = relative displacement of magnets with respect to ground input

$z_c = x_c - y$ = relative displacement of coils with respect to ground input

- PARAMETERS

  M_m = Mass of magnets (and "sprung" structure)

  M_c = Mass of coils (and "sprung" structure)

  K_m = Spring constant of spring connecting magnets to ground

  K_c = Spring constant of spring connecting coils to ground

  b_m = Internal mechanical damping (friction/material losses/etc.) in magnet system

  b_c = Internal mechanical damping (friction/material losses/etc.) in coil system

  b_e = Electrical damping coefficient relating the electrical damping force to the relative velocity between the magnets and coils.

The governing equation of the vibrating magnet system is found by equating the forces on the magnets

$$\sum F = -\left(F_s + F_{m_i} + F_e\right) = M_m a_m = M_m \ddot{x_m}$$

Substituting in for the forces,

$$\begin{aligned} M_m\ddot{x}_m + b_{m_i}\dot{z}_m + b_e\left(\dot{x}_m - \dot{x}_c\right) + K_m z_m &= 0 \\ M_m\left(\ddot{z}_m + \ddot{y}\right) + b_{m_i}\dot{z}_m + b_e\left(\dot{z}_m - \dot{z}_c\right) + K_m z_m &= 0 \\ M_m\ddot{z}_m + \left(b_{m_i} + b_e\right)\dot{z}_m + K_m z_m &= b_e\dot{z}_c - M_m\ddot{y} \end{aligned} \tag{3.54}$$

Similarly, the governing equation for the coil system is given by,

$$M_c\ddot{z}_c + \left(b_{c_i} + b_e\right)\dot{z}_c + K_c z_c = b_e\dot{z}_m - M_c\ddot{y} \tag{3.55}$$

The useful power is given by,

$$P = b_e\left(\dot{x}_m - \dot{x}_c\right)^2 = b_e\left(\dot{z}_m - \dot{z}_c\right)^2 = b_e\dot{z}_r^2 \tag{3.56}$$

Thus, by setting the output variable to be $\dot{z}_r$, then the state space model of the system is given as,

$$\begin{aligned} \dot{\mathbf{z}} &= \mathbf{A}\mathbf{z} + \mathbf{B}\ddot{y} \\ \dot{z}_r &= \mathbf{C}\mathbf{z} + \mathbf{D}\ddot{y} \end{aligned} \tag{3.57}$$

where,

$$\mathbf{A} = \begin{pmatrix} 0 & 1 & 0 & 0 \\ -\frac{K_m}{M_m} & -\left(\frac{b_m}{M_m}+\frac{b_e}{M_m}\right) & 0 & \frac{b_e}{M_m} \\ 0 & 0 & 0 & 1 \\ 0 & \frac{b_e}{M_c} & -\frac{K_c}{M_c} & -\left(\frac{b_c}{M_c}+\frac{b_e}{M_c}\right) \end{pmatrix} \tag{3.58}$$

$$\mathbf{B} = \begin{pmatrix} 0 \\ -1 \\ 0 \\ -1 \end{pmatrix} \tag{3.59}$$

$$\mathbf{C} = \begin{pmatrix} 0 & 1 & 0 & -1 \end{pmatrix} \tag{3.60}$$

$$\mathbf{D} = (0) \tag{3.61}$$

To verify the model, the value of K_c is set at least 6 orders of magnitude greater than the value of K_m. This should represent a system where the coils are mounted solidly with respect to the magnets and be the same as the resonant system presented earlier (Fig. 3-11). Figure 3-12 is a plot of the calculated response to a filtered white noise input compared to the experimental data for a flexural prototype.

With the model verified in the limit as $K_c \to \infty$, the response of this system to a wide-band input for different values of K_c is plotted in Fig. 3-13. As can be seen the power amplitude is greater, but still falls off exponentially for increasing band-width input, and the magnitude is greater for decreasing frequency difference between the resonant systems. Thus, although the amplitude is slightly larger the exponential fall off still exists and therefore this is not a viable solution for wide-band harvesting.

3.3 Active Control

In general, vibration energy harvesting involves extracting the maximum amount of power possible from a vibrating environment. Typical a proof mass is connected to the vibrating environment and power is extracted from the relative motion between

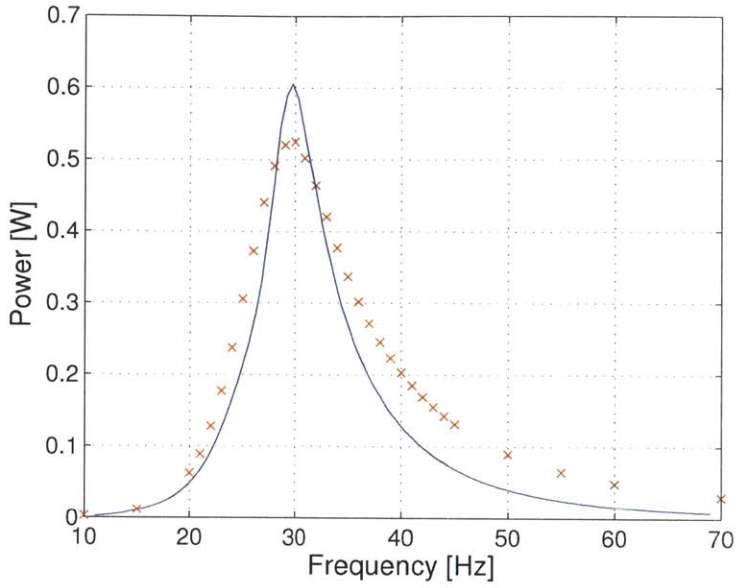

Figure 3-11: *Plot of the power as a function of harmonic input frequency for a very large value of K_c. The plot is compared to experimental data collected from a flexural prototype.*

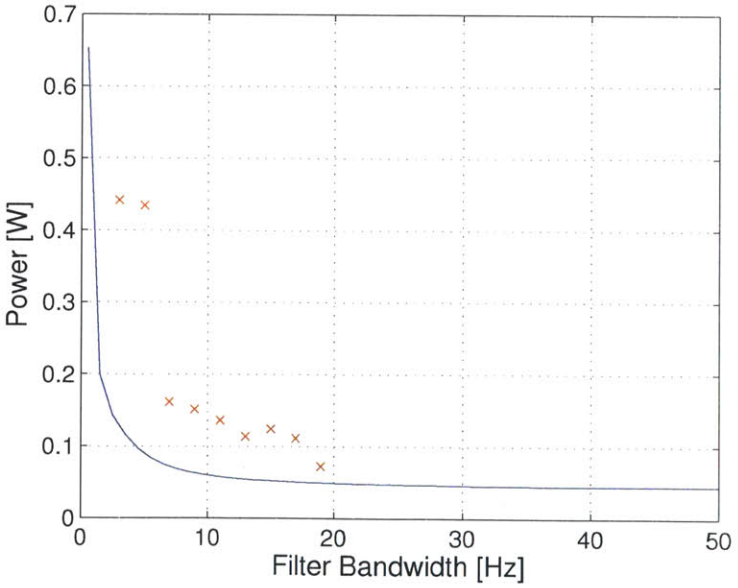

Figure 3-12: *Plot of the calculated response (with $K_c \to \infty$)to a filtered white noise input of varying bandwidth compared to the experimental data for the existing prototype. This plot is again used to verify the model.*

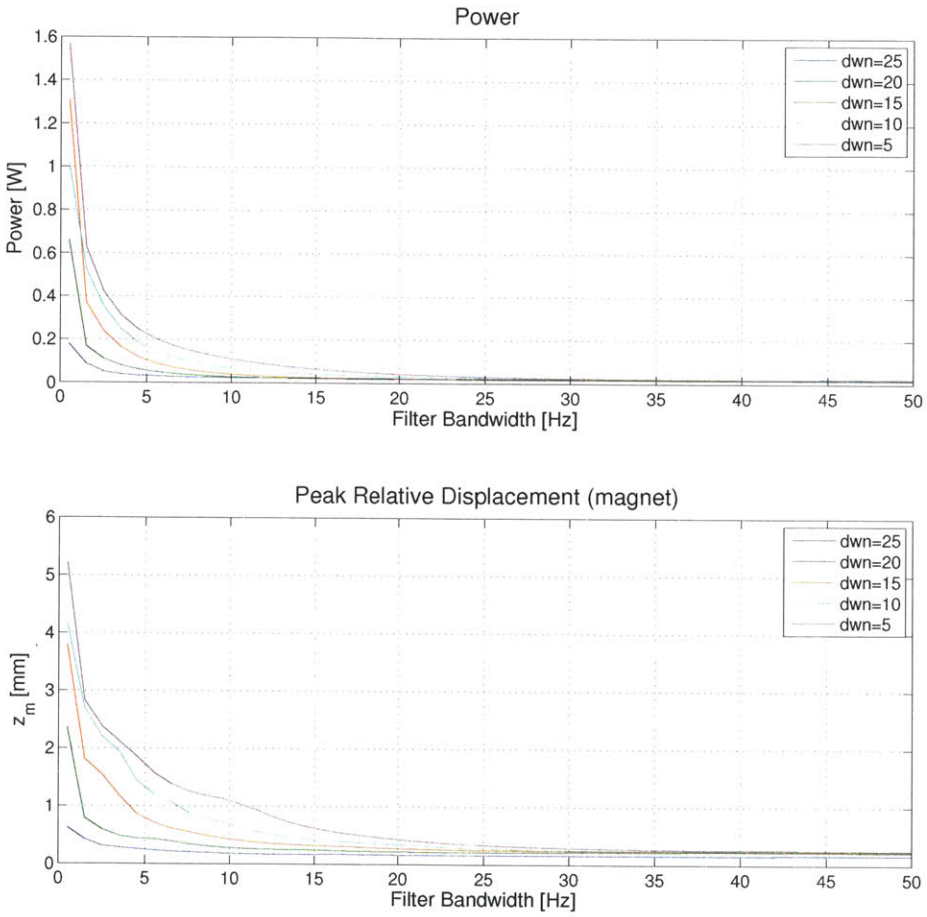

Figure 3-13: *Plot of the expect power as a function of the filter bandwidth. Included for reference is the relative displacement of the magnets.*

the environment and proof mass[3, 9, 18, 31]. However, due to the typical random nature of most vibrations, standard resonant based architectures fail to resonante [8], so various forms of rectification are used from "magnetic plucking" to "elastic storage"[15, 24, 23, 12]. Each new architecture is evaluated against previous designs, but without a maximum estimate the question still remains whether the design is the best. By using optimal control theory, an estimate of the maximum possible energy that can be extracted from a vibrating environment through the use of a proof mass can be determined independent of the extraction method, thus providing a benchmark for evaluation of future designs.

3.3.1 Statement of the General Optimal Control Problem[4]

The classic formulation of the optimal control problem involves optimizing (minimizing or maximizing) a performance functional $J(\mathbf{u})$ by controlling a trajectory $\mathbf{x}$ with an optimized control input $\mathbf{u}$. Given a system governed by the equation,

$$\dot{\mathbf{x}} = f(\mathbf{x}, \mathbf{u}, t) \tag{3.62}$$

with performance functional,

$$J(\mathbf{u}) = K\left[\mathbf{x}(t_1)\right] + \int_{t_0}^{t_1} L\left[\mathbf{x}(t), \mathbf{u}(t), t\right] dt \tag{3.63}$$

and Hamiltonian,

$$H(\mathbf{x}, \mathbf{p}, \mathbf{u}, t) = L(\mathbf{x}, \mathbf{u}, t) + \langle \mathbf{p}, f(\mathbf{x}, \mathbf{u}, t) \rangle \tag{3.64}$$

where $\mathbf{p}$ is the costate vector of the governing state equation (equation 3.62). Then, $\mathbf{u}^*(t)$ is the control input that will maximize $J(\mathbf{u})$ provided that,

1. The system of differential equations,

$$\dot{\mathbf{x}}^*(t) = \frac{\partial H}{\partial \mathbf{p}}\left[\mathbf{x}^*(t), \mathbf{p}^*(t), \mathbf{u}^*(t), t\right] \tag{3.65}$$

$$\dot{\mathbf{p}}^*(t) = -\frac{\partial H}{\partial \mathbf{x}}\left[\mathbf{x}^*(t), \mathbf{p}^*(t), \mathbf{u}^*(t), t\right] \tag{3.66}$$

with boundary conditions,

$$\mathbf{x}^*(t_0) = \mathbf{x}_0 \tag{3.67}$$

$$\mathbf{p}^*(t_1) = \frac{\partial K}{\partial \mathbf{x}}\left[\mathbf{x}^*(t_1)\right] \tag{3.68}$$

is satisfied.

2.

$$\left.\frac{\partial H}{\partial \mathbf{u}}\right|_* = 0 \tag{3.69}$$

3.

$$\left.\frac{\partial^2 H}{\partial \mathbf{u}^2}\right|_* \quad \text{is negative definite} \tag{3.70}$$

The solution can be verified by Pontryagin's minimum principle[4],

$$H(v^*, p^*, F^*, t) \geq H(v^*, p^*, F, t) \tag{3.71}$$

3.3.2 Formulation of General Vibration Energy Harvesting Problem as an Optimal Control Problem

Figure 3-14 shows the lumped parameter model that is used to formulate the control problem. A known, although typically random, acceleration is applied to a vibrating reference frame. Comparing the motion to absolute ground, the measured acceleration can be represented in terms of the absolute displacement, $\ddot{y}$. To extract energy, a proof mass is attached to the reference frame by two forces. One force, F_i, represents unavoidable losses in the system (e.g. bearing friction). The other force, F, represents the force applied to the proof mass as a result of energy extraction from the system.

The sum of the forces acting on the proof mass is used to obtain the governing equation of the system (figure 3-15).

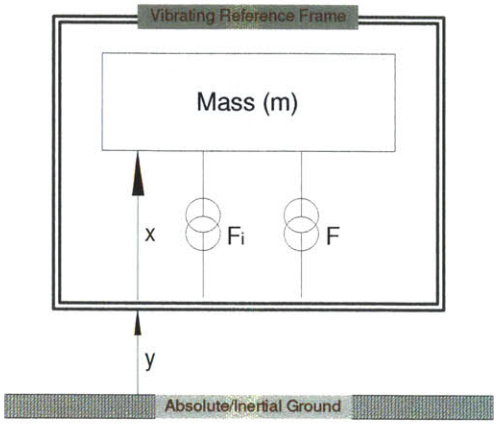

Figure 3-14: *Lumped parameter model of a general energy harvesting system. A proof mass is attached to the vibrating reference frame by two general forces. One force represents unavoidable losses in the system F_i. The other force F is the control input used to control the trajectory of the proof mass x.*

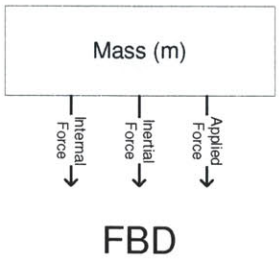

Figure 3-15: *Force body diagram applied to the assumed proof mass used to determine the system's governing equation.*

$$
\begin{aligned}
0 &= F_{inertial} + F_{internal} + F \\
0 &= m\frac{d^2}{dt^2}(x+y) + F_i + F \\
\frac{d^2x}{dt^2} &= -\frac{1}{m}(F_i + F) - \frac{d^2y}{dt^2} \\
(\dot{x}) &= -\frac{1}{m}(F_i + F) - \ddot{y} \\
\dot{v} &= -\frac{1}{m}(F_i + F) - a
\end{aligned} \tag{3.72}
$$

Where, $v \equiv \dot{x}$ and $a \equiv \ddot{y}$. Letting the relative velocity between the proof mass and the reference frame be the state variable, then equation 3.72 is of the same form as the governing equation in the general formulation (equation 3.62).

Note, some generality is lost at this point since the derived governing equation assumes a zero impedance source and thus any applied force will not affect the motion of the reference frame. For many applications of energy harvesting the device size is relatively small compared to the vibrating reference frame and the zero impedance assumption is valid. If the impedance is non-zero, the coupled state equations can be substituted in as vectors and the analysis process is identical.

Power is extracted from the system by the applied force, F, and the average power extracted over a fixed time $0 \rightarrow T$ is given as,

$$
Power_{avg} = \frac{1}{T}\int_0^T Fvdt = \int_0^T \frac{Fv}{T}dt \tag{3.73}
$$

To maximize the total power extracted by the force, we let $Power_{avg}$ represent the performance functional of the system, thus,

$$
K\left[v(T)\right] \equiv 0 \tag{3.74}
$$

and,

$$
L\left[v(t), F(t), t\right] \equiv \frac{Fv}{T} \tag{3.75}
$$

The Hamiltonian is then given as,

$$H(v,p,F,t) = \frac{Fv}{T} + p\left[-\frac{1}{m}(F_i + F) - a\right] \tag{3.76}$$

$$= \left(\frac{v}{T} - \frac{p}{m}\right)F - p\left(\frac{F_i}{m} + a\right) \tag{3.77}$$

To maximize the power, we apply the 3 conditions presented earlier.

1. The first equation is satisfied by definition,

$$\dot{v}^* = \frac{\partial H}{\partial p}(v^*, p^*, F^*, t)$$

$$= -\frac{1}{m}(F_i + F^*) - a \tag{3.78}$$

Which is identical to the governing differential equation (equation 3.72), and thus must be satisfied by the physical system.

The second equation provides the physical definition of the costate for the system,

$$\dot{p}^* = -\frac{\partial H}{\partial v}(v^*, p^*, F^*, t)$$

$$= -\left[\frac{F^*}{T} - \frac{p^*}{m}\frac{\partial F_i}{\partial v}\right]$$

$$= \frac{p^*}{m}\frac{\partial F_i}{\partial v} - \frac{F^*}{T} \tag{3.79}$$

or,

$$\dot{p}^* - \frac{1}{m}\frac{\partial F_i}{\partial v}p^* = -\frac{F^*}{T} \tag{3.80}$$

Indicating that dimensionally, the costate is physically force.

2. Notice that for the chosen performance functional the Hamiltonian is linear with respect to the control input F. Thus, the control input differential of the Hamiltonian is independent of F,

$$\left.\frac{\partial H}{\partial F}\right|_* = \frac{v^*}{T} - \frac{p^*}{m} \tag{3.81}$$

Since the Hamiltonian is linear with respect to the control force, the maximum of the performance functional must occur at a limit or boundary on F, and conditions 2 and 3 cannot be satisfied by any control force.

Knowing that the maximum of the Hamiltonian occurs at a boundary value of F, we can use Pontryagin's minimum principle (equation 3.71) to verify which boundary value of F maximizes the Hamiltonian.

$$\begin{aligned}
H(v^*, p^*, F^*, t) &\geq H(v^*, p^*, F, t) \\
\left(\frac{v^*}{T} - \frac{p^*}{m}\right) F^* & \\
-p^*\left(\frac{F_i}{m} + a\right) &\geq \left(\frac{v^*}{T} - \frac{p^*}{m}\right) F \\
& \quad -p^*\left(\frac{F_i}{m} + a\right) \\
\left(\frac{v^*}{T} - \frac{p^*}{m}\right) F^* &\geq \left(\frac{v^*}{T} - \frac{p^*}{m}\right) F
\end{aligned} \tag{3.82}$$

Thus, the optimal control input, F^*, is to apply the maximum possible force in a direction defined by SIGNUM $\left[\frac{v^*}{T} - \frac{p^*}{m}\right]$.

To evaluate the SIGNUM term start by differentiating with respect to time,

$$\begin{aligned}
\frac{\partial}{\partial t}\left(\frac{v^*}{T} - \frac{p^*}{m}\right) &= \frac{1}{T}\frac{\partial v^*}{\partial t} - \frac{1}{m}\frac{\partial p^*}{\partial t} \\
&= \frac{1}{T}\dot{v}^* - \frac{1}{m}\dot{p}^* \\
&= \frac{1}{T}\left[-\frac{1}{m}\left(F_i + F^*\right) - a\right] \\
&\quad -\frac{1}{m}\left[\frac{p^*}{m}\frac{\partial F_i}{\partial v} - \frac{F^*}{T}\right] \\
&= -\frac{p^*}{m^2}\frac{\partial F_i}{\partial v} - \frac{F_i}{mT} - \frac{a}{T}
\end{aligned} \tag{3.83}$$

3.3.3 Application of the Solution to Analytically Solvable Problem

To test the optimal control solution, we apply the solution strategy to an analytically solvable problem for comparison. First, the mechanical losses are modeled as an equivalent viscous damper ($F_i \rightarrow b_i v$), and second, we assume in all cases a harmonic reference acceleration, $\ddot{y} = a = \hbar(t)\text{RE}\left[Ae^{j\omega t}\right]$, where $\hbar$ is the Heavyside step function.

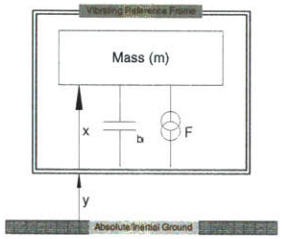

Figure 3-16: *Lumped parameter model of system with viscous internal damping*

Applying the previous optimal control theory to the simple problem with internal damping, equation 3.83 becomes,

$$\frac{\partial}{\partial t}\left(\frac{v^*}{T} - \frac{p^*}{m}\right) = -\frac{p^* b_i}{m^2} - \frac{b_i v^*}{mT} - \frac{a}{T} \tag{3.84}$$

For visual simplicity, define the SIGNUM term as $q \equiv \frac{v^*}{T} - \frac{p^*}{T}$. Then, adding and subtracting $\pm\frac{b_i v^*}{mT}$,

$$\begin{aligned}\frac{\partial q}{\partial t} &= \frac{b_i}{m}\left(\frac{v^*}{T} - \frac{p}{m}\right) - \frac{b_i v^*}{mT} - \frac{b_i v^*}{mT} - \frac{a}{T} \\ &= \frac{b_i}{m}q - \frac{2b_i v^*}{mT} - \frac{a}{T} \end{aligned} \tag{3.85}$$

$$\frac{\partial q}{\partial t} - \frac{b_i}{m}q = -\frac{2b_i v^*}{mT} - \frac{a}{T} \tag{3.86}$$

Multiplying this equation by an integration factor $e^{-\frac{b_i}{m}t}$ results in,

$$\begin{aligned} e^{-\frac{b_i}{m}t}\frac{\partial q}{\partial t} - e^{-\frac{b_i}{m}t}\frac{b_i}{m}q &= e^{-\frac{b_i}{m}t}\left(-\frac{2b_i v^*}{mT} - \frac{a}{T}\right) \\ \frac{\partial}{\partial t}\left(e^{-\frac{b_i}{m}t}q\right) &= e^{-\frac{b_i}{m}t}\left(-\frac{2b_i v^*}{mT} - \frac{a}{T}\right) \end{aligned} \tag{3.87}$$

Integrating both sides,

$$e^{-\frac{b_i}{m}t}q(t) = \int_0^t e^{-\frac{b_i}{m}s}\left(-\frac{2b_i v^*(s)}{mT} - \frac{a(s)}{T}\right)ds + q_0 \tag{3.88}$$

$$q(t) = e^{\frac{b_i}{m}t}\left(\int_0^t e^{-\frac{b_i}{m}s}\left(-\frac{2b_i v^*(s)}{mT} - \frac{a(s)}{T}\right)ds + q_0\right) \tag{3.89}$$

where s is a dummy integration variable.

Mechanically lossless ($F_i \to 0$)

With no internal forces, equation ?? becomes,

$$\frac{v^*}{T} - \frac{p^*}{m} = \int_0^t a dt + C \tag{3.90}$$

Where,

$$C = \frac{v^*(0)}{T} - \frac{p^*(0)}{m} \tag{3.91}$$

Physically, equation 3.90 agrees with intuition. The control force direction is opposite the direction of relative motion (proof mass velocity). Mathematical evaluating the integration constant, the first term is the initial state of the system which is assumed to be known ($v^*(0) \equiv v_0$), and the second term is the initial costate which can be evaluated from the costate equation (equation 3.80),

$$\begin{aligned} \dot{p}^* &= -\frac{F^*}{T} \\ p^* &= -\int_0^t \frac{F^*}{T}dt + p^*(0) \end{aligned} \tag{3.92}$$

From the boundary conditions,

$$p^*(T) = 0 \tag{3.93}$$

so,

$$\begin{aligned} p^*(T) = 0 &= -\int_0^T \frac{F^*}{T} dt + p^*(0) \\ p^*(0) &= \int_0^T \frac{F^*}{T} dt \end{aligned} \tag{3.94}$$

Since most energy harvesters are resonant based and low damping, the power harvested falls off very rapidly as the input frequency differs from the system's natural frequency. Thus, it seems reasonable that a tuning system which alters the system's effective stiffness to match the system's natural frequency to the input frequency would increase the power output of the harvester. According to [22], actively tuning the natural frequency will never result in a net power gain. The analysis in [22] is based on the sinusoidal *amplitudes* of power. However, a torque that is linearly proportional to displacement is conservative and has a *zero time average.* Thus, any active torque that can be truly be modeled as an equivalent spring should have a net zero activation power and thus should result in a net gain in harvested power.

3.3.4 Harvester Model

As originally suggested by [30] regardless of transducer type, energy harvesters can be reasonably represented by a second order mechanical system as shown in Fig. (3-17). From the free body diagram of the torques (or forces for a linear model) on the proof mass, the governing equation of the relative motion of the proof mass can be written as,

$$\begin{aligned} J\ddot{\phi} + b_i\dot{\phi} + K\phi + T_e &= -J\ddot{\alpha} \\ \ddot{\phi} + \frac{b_i}{J}\dot{\phi} + \frac{K}{J}\phi + \frac{1}{J}T_e &= -\ddot{\alpha} \end{aligned} \tag{3.95}$$

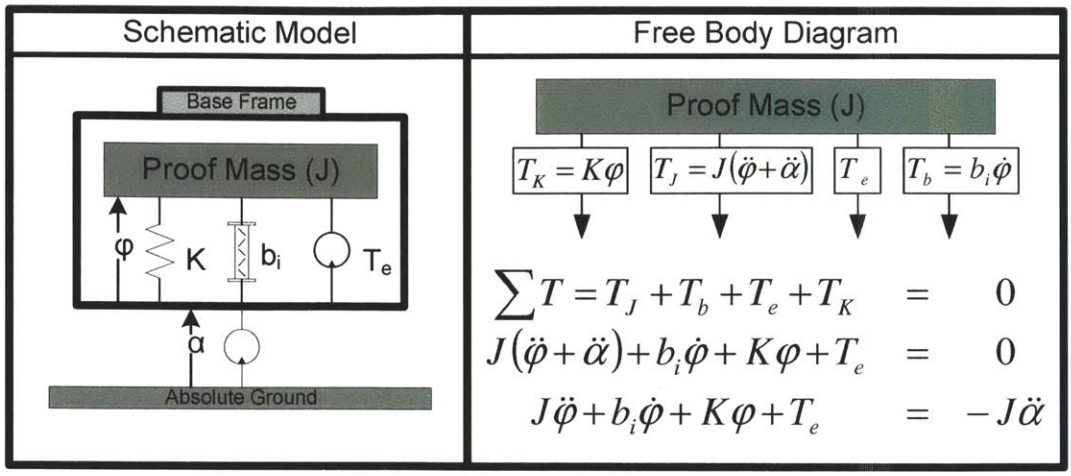

Figure 3-17: *Schematic representation of second-order lumped parameter model of a typical vibration energy harvester*

Where with reference to Fig. (3-17), ϕ is the relative displacement of the proof mass, b_i is the internal damping coefficient which represents the unavoidable (primarily mechanical) losses in the system that can not be recovered or converted into electric energy, J is the inertia of the proof mass (in linear system J=m in a rotational system J is the polar moment of inertial about the center of rotation), K is the mechanical spring constant, T_e is the electrical torque associated with the transducer, and $\ddot{\alpha}$ is the acceleration of the reference frame with respect to absolute ground. For this model, the reference frame motion is considered to be a 0 impedance source.

3.3.5 Analysis of Roundy Model

As mention previously, according to [22] "active" tuning of the resonant frequency will never result in a net power gain. In the model suggested by [22], the electrical transducer torque is modeled as an equivalent viscous damper (which according to both [22, 30] is a reasonable model for the "important aspects" of all three major electrical transduction methods: electro-magnetic, electro-static, and piezoelectric) in parallel with an "actuator" torque that is used to tune the effective natural frequency of the system, Fig. (3-18). As explained by [22], tuning the effective natural frequency

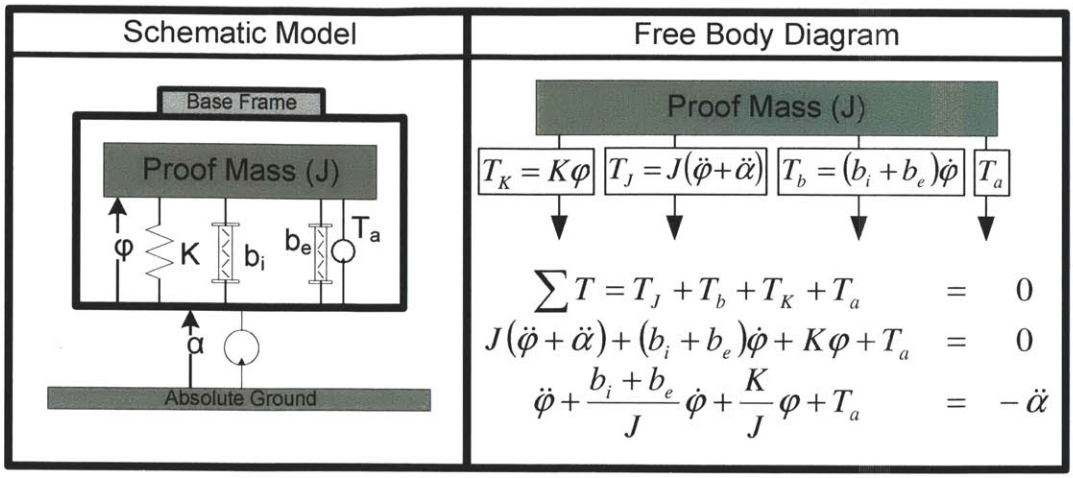

Figure 3-18: *Schematic representation of equivalent second-order lumped parameter energy harvesting model with electrical transducer modeled as an equivalent viscous damper in parallel with an actuator torque used to tune the natural frequency of the system*

of the system is the equivalent of providing an actuation torque (T_a in Fig. (3-18)) that is linearly proportional to the relative displacement or relative acceleration of the proof mass which will change the effective stiffness or effective mass of the system respectively. In addition, [22] shows that, as expected, the result of providing an effective stiffness or effective mass are identical. Thus, for simplicity, focusing only on changing the effective stiffness, the actuator torque is, $T_a = K_a\phi$, and the power required by the actuator is then given by,

$$P_a(t) = T_a\dot{\phi}(t) = K_a\phi(t)\dot{\phi}(t) \tag{3.96}$$

Which, following a similar procedure as outlined in the following section, for a harmonic input acceleration of frequency ω can be written as,

$$P_a(t) = \frac{J\left(r^2 - 1\right)A^2}{8\xi^2 r^2 \omega}\sin\left(2\omega\right) \tag{3.97}$$

Where $r = \omega/\omega_{n_m}$ is a non-dimensional frequency ratio comparing the mechanical natural frequency (ω_{n_m}) to the tuned natural frequency (ω_n), A is the amplitude of

the harmonic input acceleration, and $\xi = b/2m\omega_n$ is the non-dimensional damping ratio. According to [22] the amplitude of this power is always greater than the gain in amplitude from tuning the frequency resulting in a net power loss from tuning. This is true if the assumption is made that the actuator power must always be supplied (as in [22] for the case of a piezoelectric actuator where the power supplied to the piezoelectric material is supplied separately of the energy harvesting module). However, this is a very limiting definition of "active" tuning. A tuning torque that is linearly proportional to displacement is still actively changing the natural frequency, but is nothing more than an equivalent spring which is conservative. This is verified mathematically by noticing that the time average of the actuation torque in Eq. (3.97) over n periods of oscillation is identically zero. Thus, an "active" torque that is proportional to displacement and capable of utilizing the conservative nature of the torque dependency should have a zero time average power and thus the net gain in harvested time average power of the tuned system will be positive. Admittedly, some efficiency losses may be associated with the actuation torque but as explored and verified later in the current controlled electro-magnetic transducer section, these losses would not be expected to be on the same order of magnitude as the actuation torque amplitude presented and can be included in the model as additional internal losses.

3.3.6 Equivalent Mechanical Components Model

Assuming a tuning actuator can be built to take advantage of the conservative nature of the tuning torque, then tuning the natural frequency to the input frequency will result in an increase in harvested power. To evaluate this claim, the transducer torque of Fig. (3-17) is assumed to be a linear combination of torques which are linearly proportional to displacement and velocity and thus represent an equivalent mechanical spring in parallel with an equivalent mechanical viscous damper.

$$T_e = K_e\phi + b_e\dot{\phi} \tag{3.98}$$

The instantaneous power required by the electrical transducer can then be written as,

$$P_e(t) = T_e(t)\dot{\phi}(t) = \left(K_e\phi(t) + b_e\dot{\phi}(t)\right)\dot{\phi} \tag{3.99}$$

In order to evaluate the power, substitute T_e into the general governing equation (Eq. (3.95)) which results in the equivalent mechanical components model for energy harvesting,

$$\ddot{\phi} + \frac{b_i + b_e}{J}\dot{\phi} + \frac{K + K_e}{J} = -\ddot{\alpha} \tag{3.100}$$

From this, the transfer function relating input acceleration to relative displacement can be written as,

$$\begin{aligned} \frac{\phi}{\ddot{\alpha}} = H_{\ddot{\alpha}\to\phi} &= \frac{-1}{\left(\frac{K+K_e}{J} - \omega^2\right) + \left(\frac{b_i+b_e}{J}\omega\right)j} \\ &= he^{-j\theta} \end{aligned} \tag{3.101}$$

Where,

$$h = \frac{-1}{\sqrt{\left(\frac{K+K_e}{J} - \omega^2\right)^2 + \left(\frac{b_i+b_e}{J}\omega\right)^2}} \tag{3.102}$$

$$\theta = \arctan\left(\frac{\frac{b_i+b_e}{J}\omega}{\frac{K+K_e}{J} - \omega^2}\right) \tag{3.103}$$

Harmonic Input Acceleration

At this point, for simplicity some level of generality is lost by assuming the input acceleration is purely harmonic. Rarely is a real world signal purely harmonic, but for the class of input signals for which the spectral density exhibits a sharp frequency peak and the surrounding noise is some small percentage of the total acceleration amplitude, the analysis will be approximately correct. More importantly by assuming a harmonic input an analytical solution can be found which can be used to understand the governing aspects of the system. Thus, assuming,

$$\ddot{\alpha} = \Re\left[Ae^{j\omega t}\right] \tag{3.104}$$

and using the transfer function of Eq. (3.101), the relative displacement and velocity are,

$$\phi = hA\cos(\omega t - \theta) \tag{3.105}$$

$$\dot{\phi} = -hA\omega\sin(\omega t - \theta) \tag{3.106}$$

Plugging these relationships into the power equation (Eq. (3.99)), the instantaneous power becomes,

$$\begin{aligned} P_e(t) &= -K_e h^2 A^2 \omega \cos(\omega t - \theta)\sin(\omega t - \theta) + b_e h^2 A^2 \omega^2 \sin^2(\omega t - \theta) \\ &= h^2 A^2 \omega^2 b_e \left\{ \underbrace{-\frac{K_e}{2b_e\omega}\sin\left[2(\omega t - \theta)\right]}_{1} + \underbrace{\sin^2(\omega t - \theta)}_{2} \right\} \end{aligned} \tag{3.107}$$

As a rudimentary check of Eq. (3.107) the units are examined in Table (3.3.6) and found to be correctly units of power. The 1^{st} part is the power associated with the

Base Variables				Combined Variables	
Variable	Units	Variable	Units	Variable	Units
K, K_e	$N \cdot m$	ω	$\frac{1}{s}$	$h(K, K_e, b_i, b_e, J, \omega)$	s^2
b_i, b_e	$N \cdot m \cdot s$	A	$\frac{rad}{s^2}$	$\frac{K_e}{2b_e\omega}$	$\cdot$
J	$N \cdot m \cdot s^2$			$h^2A^2\omega^2b_e$	$\frac{N \cdot m}{s}$
Power					
$P_e = h^2A^2\omega^2b_e = \left[\frac{N \cdot m}{s}\right] = [W]$					

Table 3.1: *Unit analysis of instantaneous power equation (Eq. (3.107)) derived from the equivalent mechanical model with harmonic base excitation*

equivalent spring which is equally positive and negative thus requiring and providing power with a zero time average. The 2^{nd} part is the power associated with equivalent damping and is always positive indicating that the damper always extracts energy from the system. Figure (3-19) is a plot of the instantaneous power as a function of time. As the ratio of equivalent spring constant to equivalent damping coefficient increases it can be seen that the amplitude of the oscillations increases, but due to

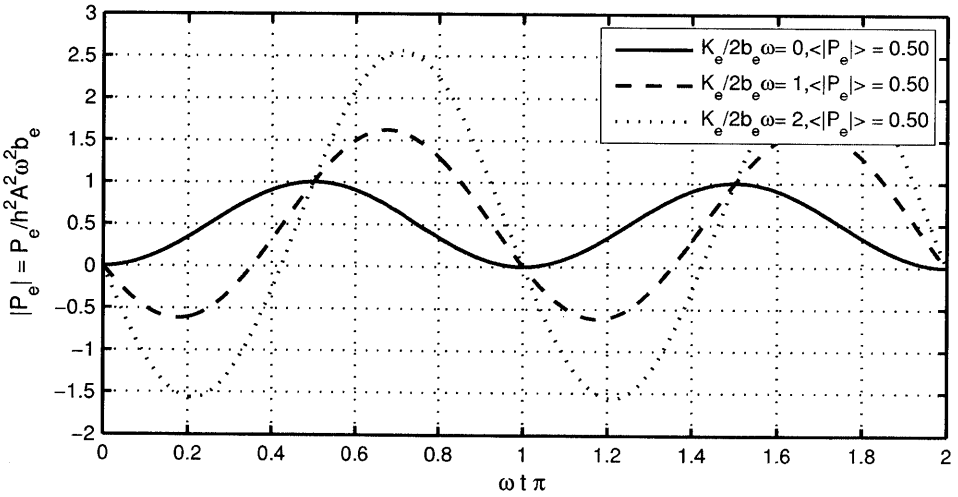

Figure 3-19: *Plot of the normalized instantaneous power as a function of normalized time for one period of oscillation. Notice that as expected, although larger values of spring constant do produce larger power amplitudes, due to the conservative nature of the tuning force the time average of the normalized output power is always 0.5.*

the conservative nature of the equivalent spring the average is always 0.5. This can be verify mathematically by taking the time average of Eq. (3.107),

$$\begin{aligned}\langle P_e \rangle &= \frac{\omega}{2\pi} \int_{t=0}^{\frac{2\pi}{\omega}} h^2 A^2 \omega^2 b_e \left\{ \sin^2(\omega t - \theta) - \frac{K_e}{2b_e\omega} \sin\left[2(\omega t - \theta)\right] \right\} dt \\ &= h^2 A^2 \omega^2 b_e \left\{ \frac{1}{2} - 0 \right\} \\ &= \frac{1}{2} h^2 A^2 \omega^2 b_e \end{aligned} \tag{3.108}$$

To determine the maximum time average power, substitute for the definition of h,

$$\langle P_e \rangle = \frac{A^2 \omega^2 b_e}{2\left[\left(\frac{K+Ke}{J} - \omega^2\right)^2 + \left(\frac{b_i+b_e}{J}\omega\right)^2\right]} \tag{3.109}$$

and differentiate with respect to the natural frequency ($\omega_n^2 = (K + K_e)/J$),

$$\frac{\partial \langle P_e \rangle}{\partial \omega_n} = -\frac{2A^2 b_e \omega^2 \omega_n \left(\omega_n^2 - \omega^2\right)}{\left[\left(\omega_n^2 - \omega^2\right)^2 + \left(\frac{b_i + b_e}{J}\omega\right)^2\right]^2} = 0 \tag{3.110}$$

Which indicates that the maximum power occurs at $\omega_n = \omega$ or that the resonant frequency should be tuned to the input frequency to maximize the output power which is the same as originally suspected. Plugging this value into the time average power equation,

$$\langle P_e \rangle|_{\omega_n = \omega} = \frac{1}{2}\frac{b_e}{\left(b_i + b_e\right)^2} A^2 J^2 \tag{3.111}$$

and optimizing with respect to the electrical damping,

$$\frac{\partial \langle P_e \rangle|_{\omega_n = \omega}}{\partial b_e} = A^2 J^2 \left(\frac{1}{2\left(b_i + b_e\right)^2} - \frac{b_e}{\left(b_i + b_e\right)^2}\right) = 0 \tag{3.112}$$

the optimal damping is $b_e = b_i$ as expected. Thus, by setting the force coefficients of the transducer to,

$$K_e = J\left(\omega^2 - \omega_{n_m}^2\right) \tag{3.113}$$

$$b_e = b_i \tag{3.114}$$

The power harvested is maximized and given by,

$$\langle P_e \rangle \Big|_{\substack{\omega_n = \omega \\ b_e = b_i}} = \frac{A^2 J^2}{8 b_i} = \frac{J A^2 Q_i}{8 \omega_{n_m}} \tag{3.115}$$

Examination of Eq. (3.115) shows that the maximum power is dependent on the input acceleration amplitude, proof mass inertia, and internal mechanical losses. Notably, the power is not dependent on the frequency, or amplitude of the equivalent spring coefficient (K_e), since a torque linearly proportional to displacement is inherently conservative, in the time average no power is lost by this force.

For comparison consider a case where the actuator spring constant is zero ($K_e = 0$

- no frequency tuning), but the actuator damping coefficient is allowed to be tuned to the optimal value. Starting with Eq. (3.109) and setting $K_e = 0$, $\omega_{n_m} = K/J$, and $r = \omega/\omega_{n_m}$ results in,

$$\langle P_e \rangle|_{K_e=0} = \frac{1}{2}\left(\frac{AQ_i}{\omega_{n_m}}\right)^2 \frac{b_e}{x^2 + \left(1 + \frac{Q_i b_e}{J\omega_{n_m}}\right)^2} \quad \text{Where,} \quad x = Q_i \frac{1 - r^2}{r} \tag{3.116}$$

Optimizing this with respect to the electrical damping,

$$\frac{\partial \langle P_e \rangle|_{K_e=0}}{\partial b_e} = \frac{1}{2}\left(\frac{AQ_i}{\omega_{n_m}}\right)^2 \left[\frac{1}{x^2 + \left(1 + \frac{Q_i b_e}{J\omega_{n_m}}\right)^2} - \frac{2b_e\left(1 + \frac{Q_i b_e}{J\omega_{n_m}}\right)Q_i}{\left(x^2 + \left(1 + \frac{Q_i b_e}{J\omega_{n_m}}\right)^2\right)^2 J\omega_{n_m}}\right] = 0 \tag{3.117}$$

For which the optimal electrical damping coefficient is,

$$b_e = b_{e_{max}} = \frac{J\omega_{n_m}}{Q_i}\sqrt{1 + x^2} = b_i\sqrt{1 + x^2} \tag{3.118}$$

Notice that as the frequency coefficient (r) goes to one, the optimal electrical damping coefficient goes to the mechanical damping coefficient. Substituting this result into the power equation,

$$\langle P_e \rangle|_{\substack{K_e = 0 \\ b_e = b_{e_{max}}}} = \frac{JA^2Q_i}{4\omega_{n_m}}\left(\frac{1}{1 + \sqrt{1 + x^2}}\right) \tag{3.119}$$

For comparison, normalize the un-tuned power by the tuned power,

$$\rho_{e_{\text{un-tuned}}} = \frac{\langle P_e \rangle \Big|_{\substack{K_e = 0 \\ b_e = b_{e_{max}}}}}{\langle P_e \rangle \Big|_{\substack{\omega_n = \omega \\ b_e = b_i}}} = \frac{2}{1 + \sqrt{1 + x^2}}$$

$$\text{Where,} \qquad x = Q_i \frac{1 - r^2}{r} = Q_i \frac{\omega_{n_m}^2 - \omega^2}{\omega_{n_m} \omega} \tag{3.120}$$

Equation (3.120) is plotted in Fig. (3-20) as a function x. As can be seen, the normal-

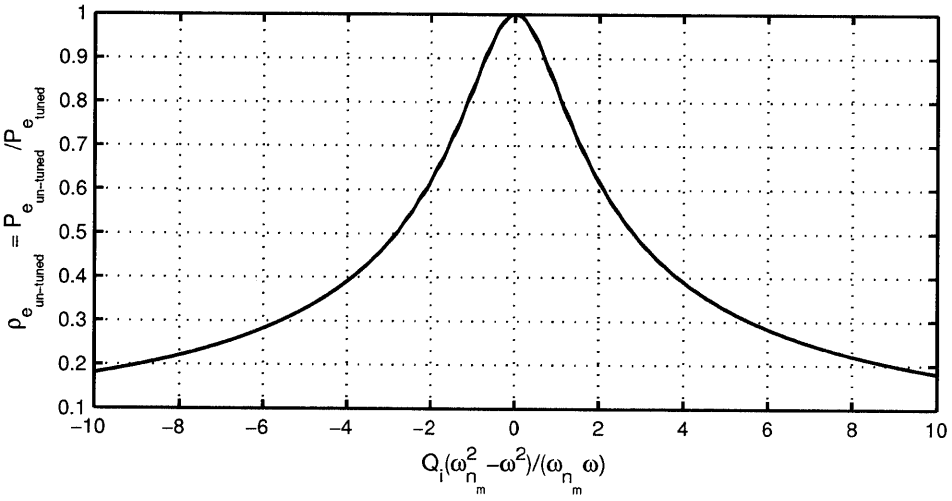

Figure 3-20: *Net time-average, un-tuned power dissipated by the electrical transducer normalized by the net time-average, tuned power dissipated by the electrical transducer. When the mechanical natural frequency matches the input frequency the un-tuned and tuned powers are equal. For all other values of x, the normalized, un-tuned power is* less than one, *indicating that the net time-average power for a tuned harvester will always be greater than the net time-average power for an un-tuned harvester. Also note that tuning is more advantageous for larger internal quality factors.*

ized, net, time-average, un-tuned power is always less than or equal to one indicating that an electrical transducer that includes an equivalent spring type tuning actuator

will always produce the same or greater power than an un-tuned electrical transducer. For example, when $x = 2$ the un-tuned transducer will harvest approximately 60% as much energy as the tuned harvester where corresponds to a Thus, for the proposed model, the electrical transducer *should* include a tuning component. value of As should be expected, tuning is increasingly advantageous for larger values of internal quality factor. This is seen in Fig. (3-20) by noticing that larger values of Q_i result in larger values of x. Intuitively, as the mechanical quality factor increases the response spectra gets narrower and thus more advantage is gained by bringing the system back to the peak of the spectra.

Equation (3.120) suggests that tuning the system is always advantageous regardless of frequency ratio; however, tuning does have limits. Although power is not effected by increasing the spring coefficient, the total torque that must be provided by the transducer is. The actuator torque is found for both the tuned and un-tuned cases by substituting the respective optimal values for K_e and b_e into (Eq. (3.98)).

$$\begin{aligned} T_e &= K_e\phi + b_e\dot{\phi} \\ &= hA\left[K_e\cos(\omega t - \theta) - b_e\omega\sin(\omega t - \theta)\right] \end{aligned} \tag{3.121}$$

Un-Tuned

$$JA\frac{\sqrt{1+x^2}}{\sqrt{x^2+\left(1+\sqrt{1+x^2}\right)^2}}\sin(\omega t - \theta)$$

Tuned

$$\frac{JA}{2}\sqrt{1+x^2}\sin(\omega t - \theta + \beta) \tag{3.122}$$

Where, $\beta = \arctan(x))$

Similarly to the power, the un-tuned torque amplitude is normalized by the tuned torque amplitude,

$$\begin{aligned} \tau_{e_{\text{un-tuned}}} &= \frac{T_{e_{\text{un-tuned}}}}{T_{e_{\text{tuned}}}} \\ &= \frac{2}{\sqrt{x^2+\left(1+\sqrt{1+x^2}\right)^2}} \end{aligned} \tag{3.123}$$

Normalized torque is plotted in Fig. (3-21). As expected, the tuning actuator will

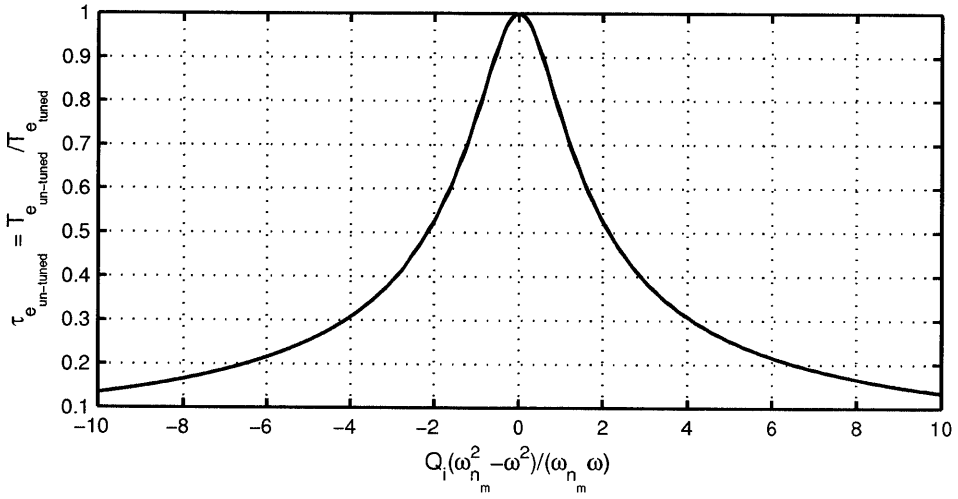

Figure 3-21: *Un-tuned torque amplitude normalized by tuned torque amplitude*

require more torque amplitude. It might be expected that some losses will occur for large torque amplitudes.

3.3.7 Current Controlled Electro-magnetic Transducer

No losses

Assuming an electro-magnetic transducer whose torque can be modeled as linearly proportional to current,

$$T_e = \kappa i \tag{3.124}$$

then the governing equation becomes,

$$\ddot{\phi} + \frac{b_i}{J}\dot{\phi} + \frac{K}{J}\phi + \frac{\kappa}{J}i = -\ddot{\alpha} \tag{3.125}$$

Again assuming $\ddot{\alpha}$ is harmonic,

$$\ddot{\alpha} = \Re\left[Ae^{j\omega t}\right] \tag{3.126}$$

Additionally, assuming i is of the form,

$$i = \Re\left[Ie^{j\omega t}\right] \tag{3.127}$$

Then the solution becomes,

$$\begin{aligned} \phi &= -\frac{Q_i}{r\omega_{nm}^2\left(1+x^2\right)}\Re\left[(x-j)\left(\frac{\kappa}{J}I+A\right)e^{j\omega t}\right] \\ &= -\frac{Q_i}{r\omega_{nm}^2\left(1+x^2\right)}\Re\left[\Phi e^{j\omega t}\right] \\ \text{Where,} \qquad \Phi &= (x-j)\left(\frac{\kappa}{J}I+A\right) \end{aligned} \tag{3.128}$$

The power used or dissipated by the actuator is give by,

$$P_e = T_e\dot{\phi} = -\frac{Q_i\kappa}{r\omega_{nm}^2\left(1+x^2\right)}\Re\left[Ie^{j\omega t}\right]\Re\left[j\omega\Phi e^{j\omega t}\right] \tag{3.129}$$

In complex notation, the time average can be written as,

$$\begin{aligned} \langle P_e\rangle &= -\frac{Q_i\kappa}{2r\omega_{nm}^2\left(1+x^2\right)}\Re\left[j\omega\Phi I^*\right] \\ &= -\frac{Q_i\kappa}{2r\omega_{nm}^2\left(1+x^2\right)}\Re\left[(x-j)\left(\frac{\kappa}{J}II^*+AI^*\right)\right] \end{aligned} \tag{3.130}$$

Letting,

$$I = I_r + I_j j \tag{3.131}$$

where I_r and I_j are real valued, then,

$$I^* = I_r - I_j j \tag{3.132}$$

Plugging into Eq. (3.130),

$$\begin{aligned} \langle P_e\rangle &= -\frac{Q_i\kappa}{2r\omega_{nm}^2\left(1+x^2\right)}\Re\left[(x-j)\left(\frac{\kappa}{J}\left(I_r^2+I_j^2\right)+A\left(I_r-I_j j\right)\right)\right] \\ &= -\frac{Q_i\kappa x}{2r\omega_{nm}^2\left(1+x^2\right)}\left[\frac{\kappa}{J}\left(I_r^2+I_j^2\right)+AI_r+AxI_j\right] \end{aligned} \tag{3.133}$$

Optimizing first with respect to the real and imaginary components of the current,

Real (I_r)	Imaginary (I_j)
$\frac{\partial \langle P_e \rangle}{\partial I_r} = -\frac{Q_i \kappa x}{2r\omega_{nm}^2(1+x^2)}\left[\frac{2\kappa}{J} I_r + A\right] = 0$	$\frac{\partial \langle P_e \rangle}{\partial I_j} = -\frac{Q_i \kappa x}{2r\omega_{nm}^2(1+x^2)}\left[\frac{2\kappa}{J} I_j + Ax\right] = 0$
$I_{r_{max}} = -\frac{JA}{2\kappa}$	$I_{i_{max}} = -\frac{JAx}{2\kappa} = I_{r_{max}} x$

(3.134)

Substituting into the power equation, the maximum power becomes,

$$\langle P_e \rangle \Big|_{\substack{I_r = -\frac{JA}{2\kappa} \\ I_j = -\frac{JA}{2\kappa} x}} = \frac{JA^2 Q_i}{8\omega_{n_m}} \tag{3.135}$$

Equation (3.115) and Eq. (3.135) are identical indicating that choosing the optimal current provides the same power as a tuning the system. Evaluating the torque,

$$\begin{aligned} T_e &= \kappa i \\ &= \kappa \Re\left[I e^{j\omega t}\right] \\ &= \kappa \Re\left[\left(I_r + I_j j\right) e^{j\omega t}\right] \\ &= \kappa \Re\left[-\frac{JA}{2\kappa}\left(1 + xj\right) e^{j\omega t}\right] \\ &= -\frac{JA}{2} \Re\left[\left(1 + xj\right) e^{j\omega t}\right] \end{aligned} \tag{3.136}$$

Comparing this to the equivalent mechanical components model, Eq. (3.98), and applying the optimal current to Eq. (3.128) so the system displacement is,

$$\begin{aligned} \phi &= -\frac{Q_i}{r\omega_{nm}^2\left(1 + x^2\right)} \Re\left[-\frac{A}{2}\left(1 + x^2\right) j e^{j\omega t}\right] \\ &= \frac{Q_i A}{2r\omega_{nm}^2} \Re\left[j e^{j\omega t}\right] \end{aligned} \tag{3.137}$$

The torque can also be written as,

$$T_e = -\frac{Q_i A}{2r\omega_{n_m}^2}\Re\left[\left(b_e\omega - K_e j\right)e^{j\omega t}\right] \tag{3.138}$$

Comparing the real and imaginary parts of the torque equations,

$$\begin{array}{cc} \text{Real} & \text{Imaginary} \\ b_e = -\frac{2\kappa\omega_{n_m}}{AQ_i}I_r = \frac{J\omega_{n_m}}{Q_i} = b_i & K_e = \frac{2\omega\omega_{n_m}\kappa}{AQ_i}xI_j = J\omega_{n_m}\left(r^2-1\right) \end{array} \tag{3.139}$$

It can be seen that these are the same relationships as in the equivalent mechanical tuning model, which shows that the two models are equivalent.

Several things to notice brain dump: 1)The amplitude of the electrical torque increases as x increases (as the frequency difference increases or as the internal damping increases). This makes sense. The larger the difference in frequency the large the spring constant that is needed to bring the system's natural frequency to the driving frequency (cause resonance). 2)Looking at the equivalent mechanical components coefficients, we see that the equivalent damping is always present (I_R is never zero), but the spring constant is zero when $x = 0$. This is not profound just consistent with the model. If the mechanical system is already at resonance then from the mechanical side the electrical torque simply looks like an equivalent viscous damper because the spring constant is not needed for resonance. 3)An equivalent load resistance looks like an equivalent damper since the current is in phase with the voltage (no dynamic elements) and the voltage is in phase with the mechanical velocity. 4)The optimal current model has embedded in it the equivalent resistor model (setting $I_j = 0$). Thus since the current model is optimized, we should expect if the passive resistive system is the best we would expect the optimization to pick that value. Thus, we would expect the active system to always be the same or better than the passive system. As can be seen, I_j is only 0 when the normalized frequency difference is zero thus a passive system is only advantageous when the mechanical system is already at resonance.

Resistive Losses

As mentioned previously, Fig. (3-20) indicates tuning is always advantageous regardless of the frequency ratio. However, as in Fig. (3-21) the torque that must be supplied by the actuator increases significantly for large frequency differences. For very large torques it is suspected that the proposed model breaks down, and that losses associated with large actuator torques in the form of additional electrical damping must be included which will increase the overall internal damping in the system. To evaluate this suspicion, as seen in the previous section, an electro-magnetic actuator that can be modeled with torque proportional to current can be controlled to act exactly like the equivalent mechanical components model. Figure (3-22) is a schematic circuit

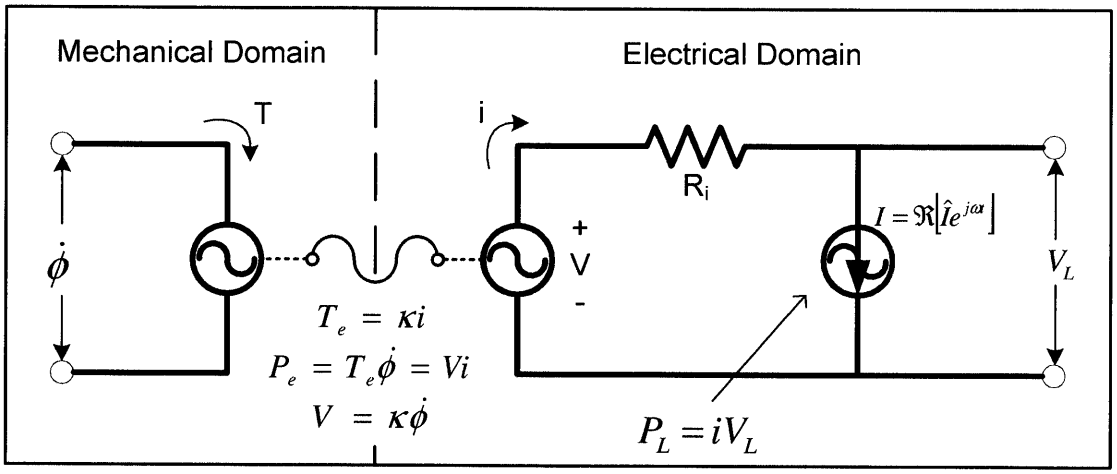

Figure 3-22: *Model used to evaluated losses associated with higher electrical torques. As the electrical current increases, a larger portion of power is lost in the internal resistance.*

representation of an electro-magnetic harvester. The model includes an electrical transducer that is assumed to be represented by the previously proposed electro-magnetic model with torque linearly proportional to current. On the electrical side, a current source, used to control phase and amplitude, is in series with an internal resistance (R_i) that consists of the unavoidable losses associated with the particular type of transducer, which for electro-magnetic transduction would primarily be coil resistance, and the losses associated with controlling the current.

Evaluating the power in the current source,

$$\begin{aligned} P_L &= iV_L \\ &= Vi - R_i i^2 \\ &= P_e - R_i i^2 \end{aligned} \tag{3.140}$$

Therefore, the changes in the proposed model captures the missing component of the previous tuning models. As can be seen, in Eq. (3.134) as the frequency difference increases, so does the current amplitude. The large current amplitude is needed to produce the large tuning torque demonstrated in Fig. (3-21). However, as suspected according to Eq. (3.140) larger currents associated with large actuator tuning torques do produce proportionally larger losses related to the higher actuator torque. Following the same procedure as outline previously, the time average of Eq. (3.140) is,

$$\langle P_L \rangle = -\frac{Q_i \kappa x}{2r\omega_{n_m}^2 \left(1+x^2\right)} \left[\frac{\kappa}{J}\left(I_r^2 + I_j^2\right) + AI_r + AxI_j\right] - R_i\left(I_r^2 + I_j^2\right) \tag{3.141}$$

And the optimal current components are,

$$I_r = -\frac{JA}{2\kappa}\left(\frac{1}{1+aR_i}\right) \tag{3.142}$$

$$I_j = I_r x \tag{3.143}$$

$$\text{Where;} \qquad a = \frac{J\omega_{n_m}\left(1+x^2\right)}{Q_i\kappa^2} = \frac{b_i}{\kappa^2}\left(1+x^2\right) \tag{3.144}$$

As the internal resistance increases, the scaling factor on the current reduces thus reducing the magnitude of the optimal current as expected. In the limit as $R_i \to 0$ the optimal current is identical to the previous value lending some amount of confidence to the results. Substituting these values into the power equation,

$$\langle P_L \rangle \Big|_{\substack{I_{r_{max}} \\ I_{i_{max}}}} = \frac{JA^2 Q_i}{8\omega_{n_m}}\left(\frac{1}{1+aR_i}\right) \tag{3.145}$$

Which again, makes intuitive sense, as the internal resistance increases, the harvested power decreases. And again, in the limit as $R_i \to 0$ the power is the same as the previous value. Care must be taken with more complicated intuitive explanations of this result since the largest component of R_i is the coil resistance and the torque constant κ and the coil resistance are related.

For completeness, compare the actively controlled system with a passive system.

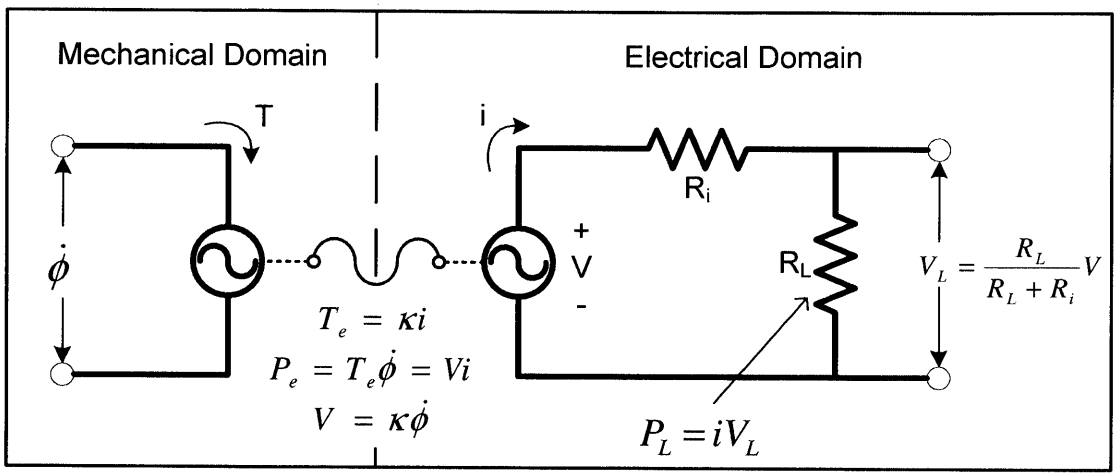

Figure 3-23: *Passively controlled.*

In this case the current control is is still proportional to current, but using the relationships seen in Fig. (3-22) the torque can be written in terms of the velocity as,

$$T_e = \frac{\kappa^2}{R_L + R_i}\dot{\phi} \tag{3.146}$$

Noticing that this is the same as Eq. (3.98) with,

$$\begin{aligned} K_e &= 0 \\ b_e &= \frac{\kappa^2}{R_L + R_i} \end{aligned}$$

Which by combining Eqs. (3.119) and (3.140) results in a time average maximum

power of,

$$\langle P_L \rangle_{(\text{passive})} = \frac{JA^2Q_i}{8\omega_{n_m}} \left(\frac{4\sqrt{1+x^2}}{x^2 + \left(1+\sqrt{1+x^2}\right)^2} \right) \left(\frac{R_L}{R_L + R_i} \right) \tag{3.147}$$

when,

$$b_e = \frac{\kappa^2}{R_L + R_i} = b_i\sqrt{1+x^2}$$

Thus, the power can be written as,

$$\begin{aligned} \langle P_L \rangle_{(\text{passive})} &= \frac{JA^2Q_i}{8\omega_{n_m}} \left(\frac{4\sqrt{1+x^2}}{x^2 + \left(1+\sqrt{1+x^2}\right)^2} \right) \left(\frac{a}{\sqrt{1+x^2}} R_L \right) \\ &= \frac{JA^2Q_i}{8\omega_{n_m}} \left(\frac{4}{x^2 + \left(1+\sqrt{1+x^2}\right)^2} \right) (aR_L) \end{aligned} \tag{3.148}$$

As before, normalize the passive system by the current controlled system,

$$\begin{aligned} \rho_{L_{(\text{passive})}} &= \frac{4aR_L\left(1+aR_i\right)}{x^2 + \left(1+\sqrt{1+x^2}\right)^2} \\ &= \frac{4}{1+\sqrt{1+x^2}} \left(\frac{R^2 + R\left(1+\sqrt{1+x^2}\right)}{\left(1+R\right)^2} \right) \end{aligned} \tag{3.149}$$

This is not identically 1 at $x = 0$ thus it is suspected that something is wrong since the passive solution is a subset of the active solution and when the passive solution is optimal the active solution should reduce to the passive solution as was shown earlier.

3.3.8 Conversion of Electrical to Mechanical Components

To simplify the abstract current solution of the previous section, consider what the electrical torque looks like for certain electrical components.

Starting with the simple voltage divider shown in Fig. (3-23), first notice that if

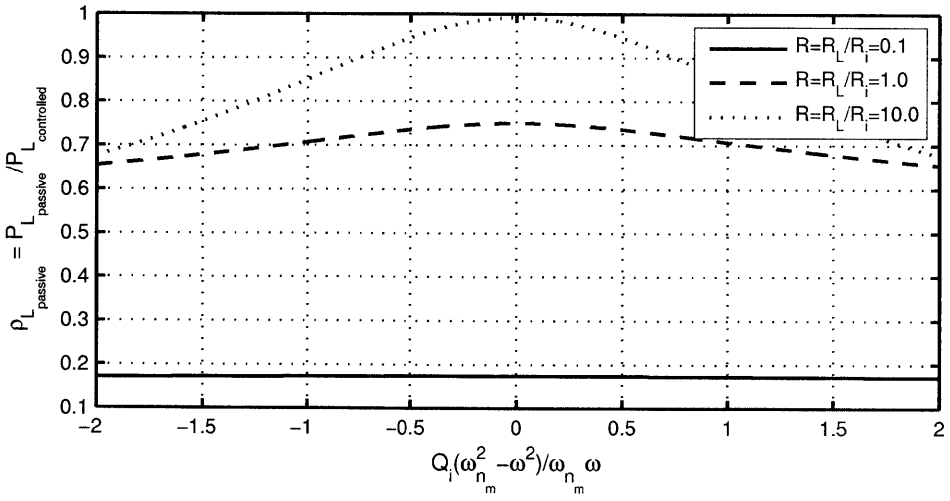

Figure 3-24: *Passive harvested power normalized by current controlled harvested power*

$R_i = 0$, then from Eq. (3.146),

$$T_e = \frac{\kappa^2}{R_L}\dot{\phi} \tag{3.150}$$

Thus for one resistor the equivalent damping coefficient is $b_e = \kappa^2/R_L$. For the resistors in series, the torque can be written as,

$$T_e = \frac{1}{\frac{1}{\kappa^2/R_L} + \frac{1}{\kappa^2/R_i}}\dot{\phi} = \frac{1}{\frac{1}{b_1} + \frac{1}{b_2}}\dot{\phi} \tag{3.151}$$

Adding an inductor in parallel with the damper is the same as adding a spring in parallel with the harvesting damper, Fig. (3-25). On the mechanical side, summing the torques around the mass-less connection (A) results in the governing equation,

$$T_e = b_{e_i}\left(\dot{\phi} - \dot{\phi}_1\right) = b_{e_L}\dot{\phi}_1 + K_e\phi_1 \tag{3.152}$$

On the electrical side, summing the currents at the common node (B) results in the

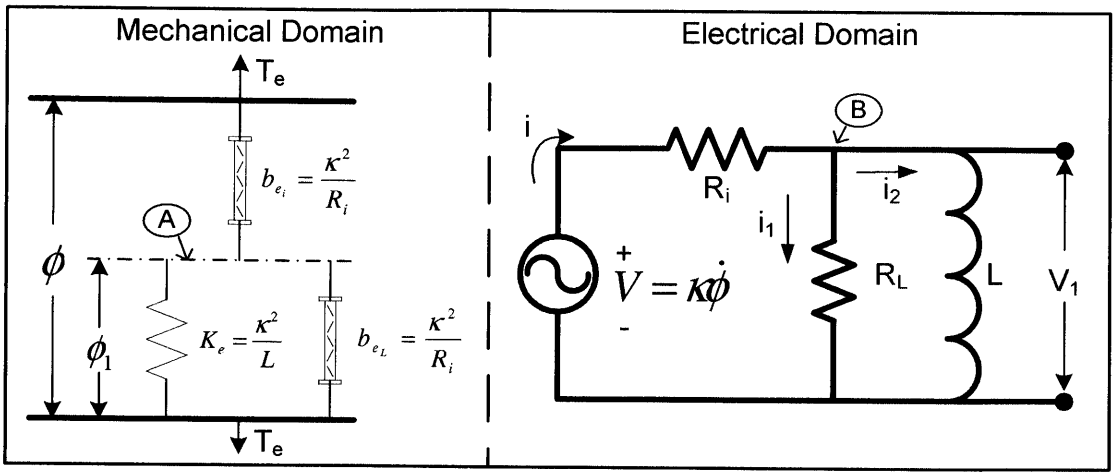

Figure 3-25: *Equivalent mechanical model a load resister in parallel with an inductor (including internal losses)*

governing equation,

$$\begin{aligned} i &= \frac{1}{R_i}(V - V_1) = \frac{1}{R_L}V_1 + \frac{1}{L}\int V_1 dt \\ \frac{1}{\kappa}T_e &= \frac{1}{R_i}\left(\kappa\dot{\phi} - \kappa\dot{\phi}_1\right) = \frac{1}{R_L}\kappa\dot{\phi}_L + \frac{1}{L}\int \kappa\dot{\phi}_1 dt \\ T_e &= \frac{\kappa^2}{R_i}\left(\dot{\phi} - \dot{\phi}_1\right) = \frac{\kappa^2}{R_L}\dot{\phi}_1 + \frac{\kappa^2}{L}\phi_1 \end{aligned} \tag{3.153}$$

Which when compared results in,

$$\begin{aligned} b_{e_i} &= \frac{\kappa^2}{R_i} \\ b_{e_L} &= \frac{\kappa^2}{R_L} \\ K_e &= \frac{\kappa^2}{L} \end{aligned} \tag{3.154}$$

Equivalent Mechanical Model Solution

Using this model adds and additional degree of freedom to the system (ϕ_1) and thus the governing differential equation becomes a system of equations,

$$\begin{aligned} J\ddot{\phi} + (b_i + b_{e_i})\dot{\phi} + K\phi - b_{e_i}\dot{\phi}_1 &= -J\ddot{\alpha} \\ b_{e_i}\dot{\phi} - (b_{e_i} + b_{e_L})\dot{\phi}_1 - K_e\phi_1 &= 0 \end{aligned} \tag{3.155}$$

For which the transfer function from $\ddot{\alpha}$ to $\dot{\phi}_1$ is,

$$\frac{\dot{\phi}_1}{\ddot{\alpha}} = H_{\ddot{\alpha}\to\dot{\phi}_1} = -\frac{Jb_{e_i}\omega j}{\left[(K - J\omega^2) + (b_i + b_{e_i})\,\omega j\right]\left[K_e + (b_{e_i} + b_{e_L})\,\omega j\right] + b_{e_i}^2\omega^2} \tag{3.156}$$

The harvested power is,

$$P = b_{e_L}\dot{\phi}_1^2 \tag{3.157}$$

To optimize the spring constant, assume a harmonic input $\ddot{\alpha} = \Re\left[Ae^{j\omega t}\right]$, and differentiate with respect to K_e.

$$K_{e_{max}} = \frac{b_{e_i}^2\omega^2\left(K - J\omega^2\right)}{\left(K - m\omega^2\right)^2 + \omega^2\left(b_i + b_{e_i}\right)^2} \tag{3.158}$$

As a sanity check, in the limit as the electrical resistance goes to zero, the internal electrical damping goes to infinity ($R_i \to 0 \Rightarrow b_{e_i} \to \infty$) the solution should reduce to the previous no-loss solution, which it does,

$$\lim_{b_{e_i}\to\infty} K_{e_{max}} = K - J\omega^2 \tag{3.159}$$

Substituting the maximum equivalent spring constant solution into the power equation and solving for the maximum harvesting damper again by differentiation results in,

$$b_{e_{L_{max}}} = \frac{b_{e_i}\left[\left(K - J\omega^2\right)^2 + \omega^2 b_i\left(b_i + b_{e_i}\right)\right]}{\left(K - m\omega^2\right)^2 + \omega^2\left(b_i + b_{e_i}\right)^2} \tag{3.160}$$

Again as a sanity check, check the limit,

$$\lim_{b_{e_i}\to\infty} b_{e_{L_{max}}} = b_i \tag{3.161}$$

Which is the same as the no-loss solution. Plugging this result into the power equation,

$$\begin{aligned} P_{max} &= \frac{1}{8}\frac{\omega^2 b_{e_i} J^2 A^2}{(K-J\omega^2)^2 + \omega^2 b_i (b_i + b_{e_i})} \\ &= \frac{mA^2 Q_i}{8\omega_{n_m}}\left(\frac{1}{1+aR_i}\right) \end{aligned} \tag{3.162}$$

Which is the same as the previous optimal current solution lending some confidence to the correctness of the mathematics.

Comparing Eqn. (3.154) to Eqn. (3.158) and (3.160) the values for L and R_L can be solve for in terms of the other fixed physical parameters.

$$\begin{aligned} L = \frac{\kappa^2}{K_e} &= \frac{(K-J\omega^2)^2 + \omega^2\left(b_i + \frac{\kappa^2}{R_i}\right)^2}{\frac{\kappa^2}{R_i^2}\omega^2(K-J\omega^2)} \\ &= \frac{\kappa^2}{J\omega_n^2}\left[\left(\frac{Q_i}{b\omega_n}\right)^2\left(\frac{1-r^2}{r^2}\right) + \left(\frac{1}{b}+1\right)^2\left(\frac{1}{1-r^2}\right)\right] \\ &= \frac{JR_i^2}{\kappa^2}\left(\frac{1}{1-r^2}\right)\left[\left(\frac{1-r^2}{r}\right)^2 + \left(\frac{1}{Q_i} + \frac{1}{J\omega_n}\frac{\kappa^2}{R_i}\right)\right] \end{aligned} \tag{3.163}$$

This equation illustrates a practical problem with analog tuning. As seen in Fig. 3-

Parameter	Value	Unit	Description
κ	0.0691	$V-s$	Electro-magnetic torque constant
J	$8X10^{-6}$	$kg-m^2$	Mass moment of inertia of rotor
ω_n	20	Hz	Natural frequency of the mechanical system
Q_i	40		Quality factor of the mechanical system

Table 3.2: *Numerical values used for inductor and resistor calculations*

26, as the frequency ratio approaches 1, the value of the inductance trends to $\pm\infty$. Additionally for frequency ratios less than 1, the inductor is negative valued which is

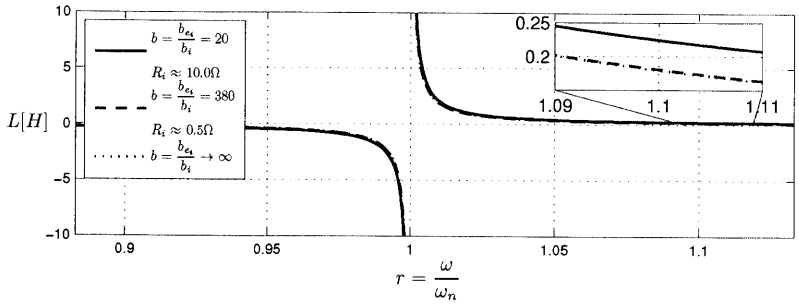

Figure 3-26: *Plot of the required parallel tuning inductance as a function of the frequency ratio. The numerical values used in the calculation of L are summarized in Table 3.3.8. As the frequency ratio approaches 1, the value of the inductance trends to $\pm\infty$ illustrating one of the practical problems with using analog components for tuning. Additionally for frequency ratios less than 1, the inductor is negative valued which is not possible with physical analog components. Also note that for the expected resistance values, the value of the tuning inductance is approximately the same as the zero resistance value (limiting case). Additionally, as is seen in section 3.3.10 the value used for κ is based on a small angle approximation that will likely not be true if the system is operating at resonance, thus the actual value of the inductor will be a function of the displacement for a single phase coil.*

not possible with physical analog components.

Closer inspection of Fig. 3-26 shows that for the expected resistance values, the value of the tuning inductance is approximately the same as the zero resistance value (limiting case $b \to \infty$). This can be seen in the inset; the inset shows that 0.5 Ω coil resistance curve is essentially identical to the limiting case.

It should also be noted, that as is seen in section 3.3.10 the value used for κ is based on a small angle approximation that will likely not be true if the system is operating at resonance. Thus, the actual value of the inductor will be a function of the displacement for a single phase coil. However, the figure does represent the maximum inductance.

Similarly, the optimal load resistance is,

$$R_L = \frac{\kappa^2}{b_{e_L}} = \kappa^2 \frac{\left(K - m\omega^2\right)^2 + \omega^2 \left(b_i + b_{e_i}\right)^2}{b_{e_i}\left[\left(K - J\omega^2\right)^2 + \omega^2 b_i \left(b_i + b_{e_i}\right)\right]} \tag{3.164}$$

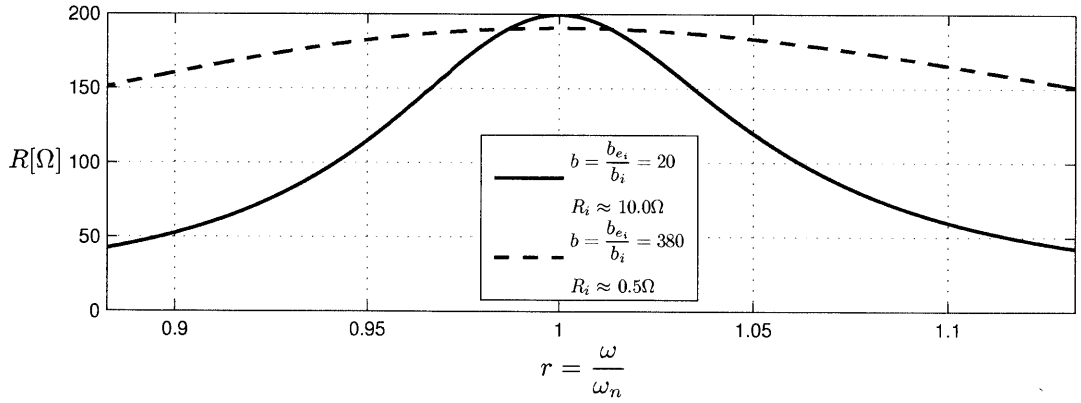

Figure 3-27: *Optimal load resistance as a function of the frequency ratio. The numerical values used for this calculation are given in Table 3.3.8.*

3.3.9 Comparison

In comparison, four different possibilities exist. *First*, the simplest is a system with no active tuning (all mechanical components fixed) and tuned to maximize the power at the resonant frequency. This configuration is the lower limiting case. *Second*, the mechanical spring is assumed to be tunable with no losses. This configuration is the upper limiting case. *Third*, the damping associated with energy harvesting (b_{e_L}) is assumed to tunable. *Fourth*, an equivalent electrical spring in parallel with the harvesting damper is assumed tunable and the harvesting damper is assumed to be tunable.

3.3.10 Torque Constant

From the electromagnetic equations, the voltage can be written as,

$$V = \lambda_0 p \cos(p\phi)\dot{\phi} \tag{3.165}$$

Thus, the torque constant can be written as,

$$\kappa = \lambda_0 p \cos(p\phi) \tag{3.166}$$

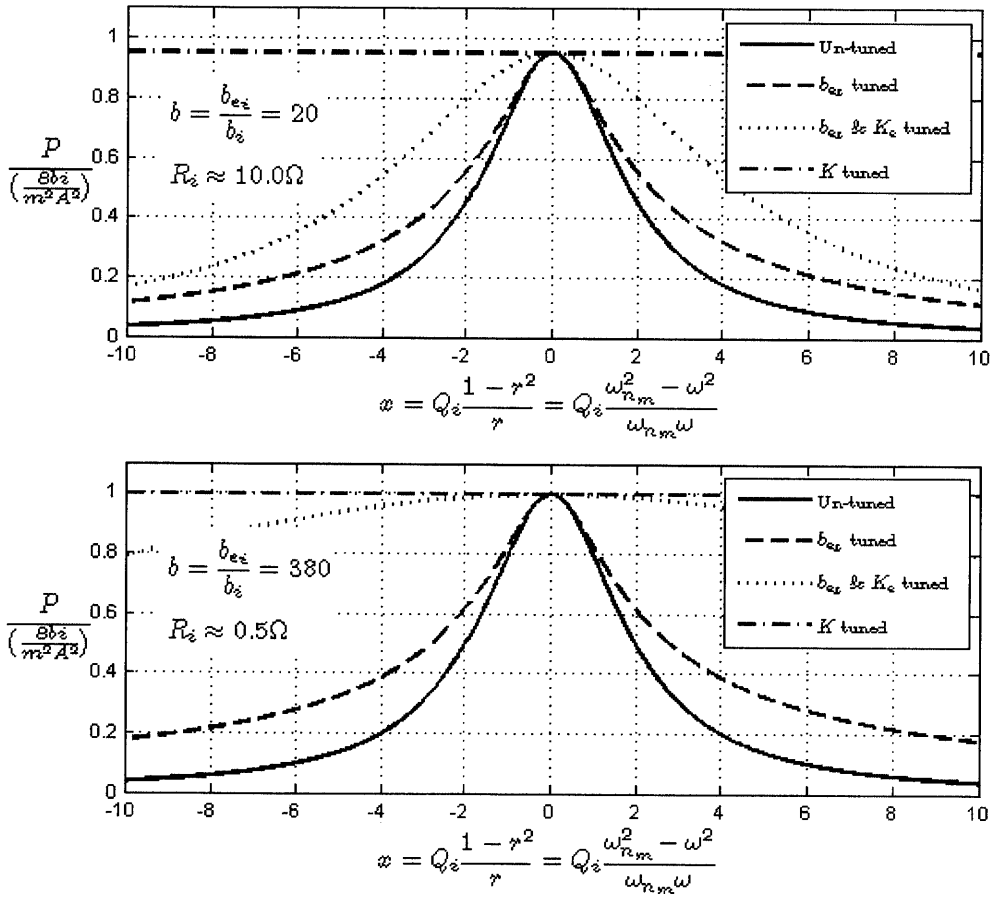

Figure 3-28: *Comparison of 4 different levels of tuning as a function of the non-dimensional frequency difference*

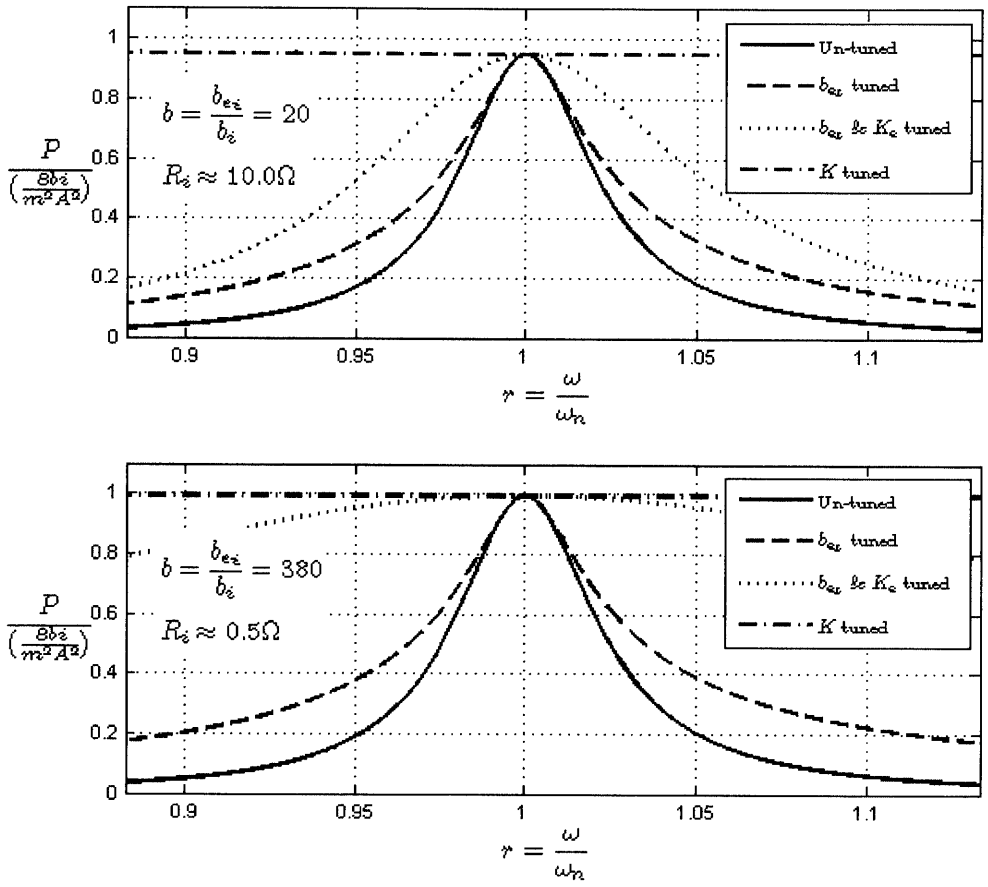

Figure 3-29: *Comparison of 4 different levels of tuning as a function of the frequency ratio*

For a constant velocity input ($\dot{\phi} = \omega_c$), the torque constant can be written as,

$$\kappa = \lambda_0 p \cos(p\omega_c t) \tag{3.167}$$

Where p is the number of pole pairs on the rotor and λ_0 is the magnetic flux, which is dependent on the parameters of the magnetic circuit.

In order to experimentally determine the torque constant, the upper clamp is removed from the torsion rod and the rotor is spun at constant velocity producing a sinusoidal voltage (Fig. 3-30). Using Matlab's Curve Fitting Toolbox,

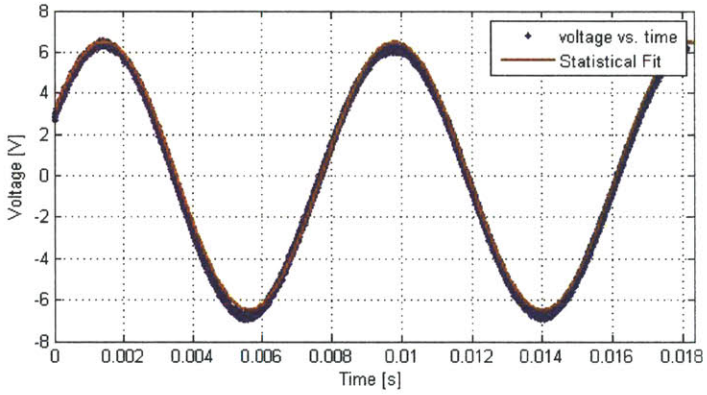

Figure 3-30: *Statistical curve fitting of constant velocity input. Using Matlab's Curve Fitting Toolbox,* $V = 6.489 \sin(749.6t + 0.4992)$

$$\begin{aligned} p\omega_c &= 749.6 \\ \lambda_0 p\omega_c &= 6.489 \end{aligned} \Rightarrow \lambda_0 = 8.66X10^{-3}Wb \tag{3.168}$$

The theoretical solution to the magnetic equations results in $\lambda_0 = 8.64X10^{-3}Wb$ a difference of 0.2%. According to Eqn. (3.166) κ is a function of the relative displacement. As an initial estimate, assume the small angle approximation applies, and

$$\kappa \approx \lambda_0 p = \left(8.64X^1 0{-}3\,[Wb]\right)(8) = 0.069\left[\frac{N-m}{A}\right] \tag{3.169}$$

As a sanity check, using the approximate values for magnet radius ($r \approx 9.7mm$) and magnet length ($h \approx 76.2mm$) this results in a magnetic pressure of $0.2\,[psi/A]$. Thus,

it would take a 5 $[A]$ current to create a 1 $[psi]$ electro-magnetic shear pressure on the rotor.

3.3.11 Impedance matching

Series or Parallel

As seen in Fig. 3-25, the proposed tuning circuit places an inductor in parallel with the load resistance. However, as seen in Fig. 3-26 for small tuning ratios the value of the inductance is very large. For such large values of inductance the internal resistance of the inductor is also very large (on the order of $k\Omega$) when compared to the expected coil resistance (on the order of Ω) and therefore cannot be neglected. However, a possible solution is to provide an equivalent impedance with a series arrangement of the inductor and load resistor as seen in Fig. 3-31. The total expected impedance in

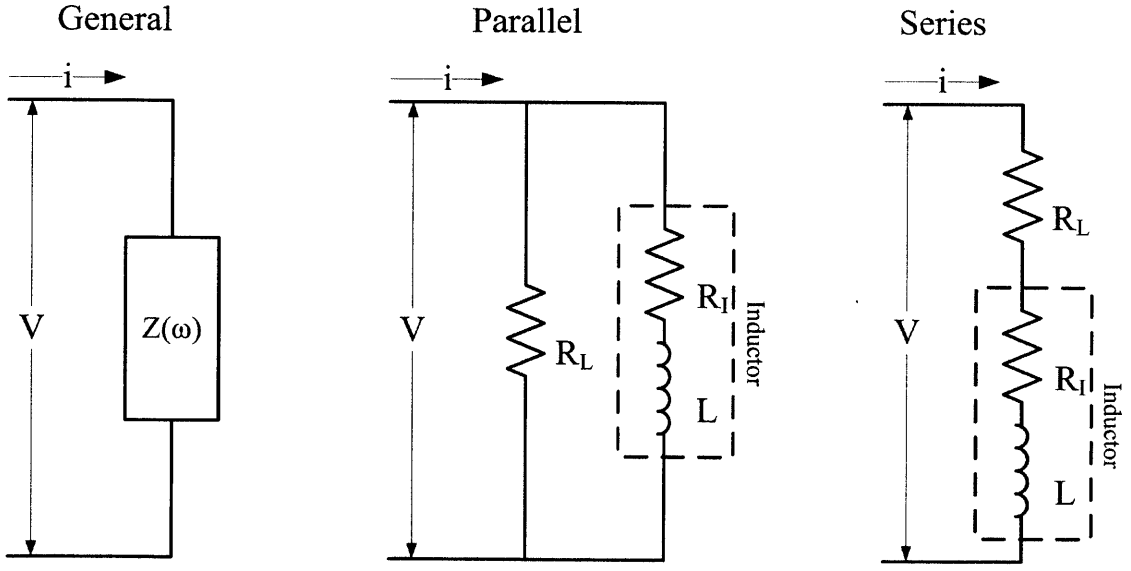

Figure 3-31: *The proposed tuning arrangement calls for an inductor in parallel with the load resistor to emulate a spring in parallel with the load damping. For large inductances, the internal resistance of the inductor can not be neglected. However, the internal resistance of the inductor becomes important.*

the the parallel case when the inductor resistance can be neglected is,

$$Z_{\text{parallel}}(\omega) = \frac{(R_L)(j\omega L)}{(R_L)+(j\omega L)} = \frac{j\omega L R_L}{R_L + j\omega L} \tag{3.170}$$

However, when the inductor resistance cannot be neglected the impedance becomes,

$$Z_{\text{parallel}}(\omega) = \frac{(R_L)(j\omega L + R_I)}{(R_L)+(j\omega L + R_I)} = \frac{R_I R_L + j\omega L R_L}{R_L + R_I + j\omega L} \tag{3.171}$$

The total impedance in the idealized series case is,

$$Z_{\text{series}}(\omega) = R_L + j\omega L \tag{3.172}$$

Denoting the series parameters by a prime, the impedance of each case can be equated to determine the equivalent series components,

$$\begin{aligned} Z_{\text{series}}(\omega) &= Z_{\text{parallel}}(\omega) \\ R'_L + j\omega L' &= \frac{R_I R_L + j\omega L R_L}{R_L + R_I + j\omega L} \end{aligned} \tag{3.173}$$

For which the equivalent series components can be found as,

$$RL' = \frac{R_L \omega^2 L^2}{R_L^2 + \omega^2 L^2} \tag{3.174}$$

$$L' = \frac{R_L^2 L}{R_L^2 + \omega^2 L^2} \tag{3.175}$$

Figure 3-32 shows that this arrangement will reduce the tuning inductance that is needed by a significant margin thus reducing the series

Capacitor

For the case when the inductor must be negative, a capacitor can be used. Following the same impedance argument, the equivalent capacitor for the parallel circuit is,

$$C = -\frac{1}{\omega^2 L} \tag{3.176}$$

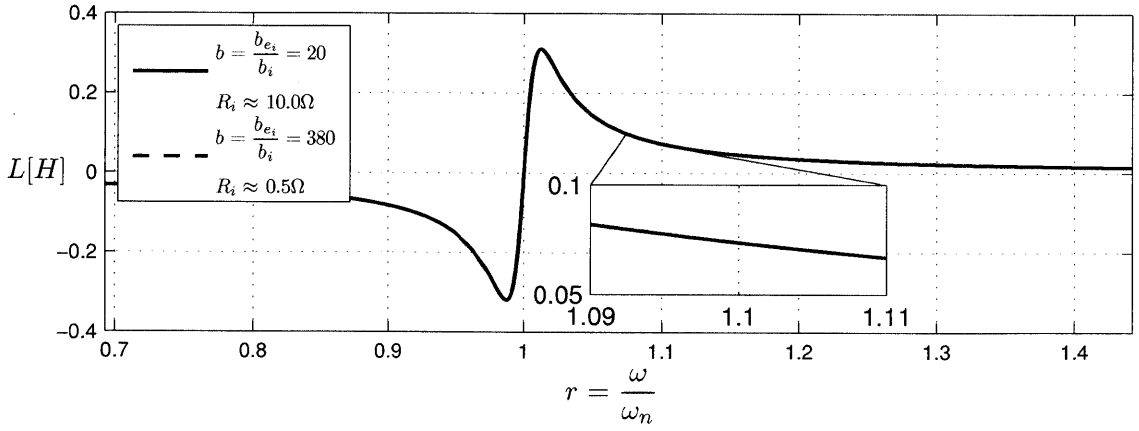

Figure 3-32: *Optimal tuning inductance for a series tuning circuit as a function of the frequency ratio.*

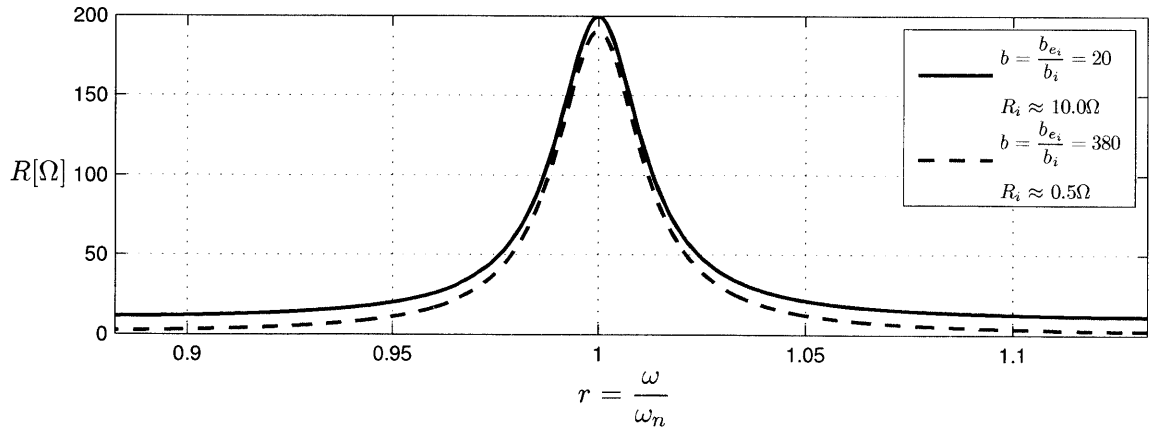

Figure 3-33: *Optimal load resistance for a series tuning circuit as a function of the frequency ratio.*

Note, this should be the same as adding a mass, and as discussed earlier, the effect on the system of adding a mass or spring should be identical. However, practically, since the inductance goes to zero as the tuning ratio approaches 1, the capacitance should go to zero further reducing the losses. Figure 3-34 However, experimental evidence

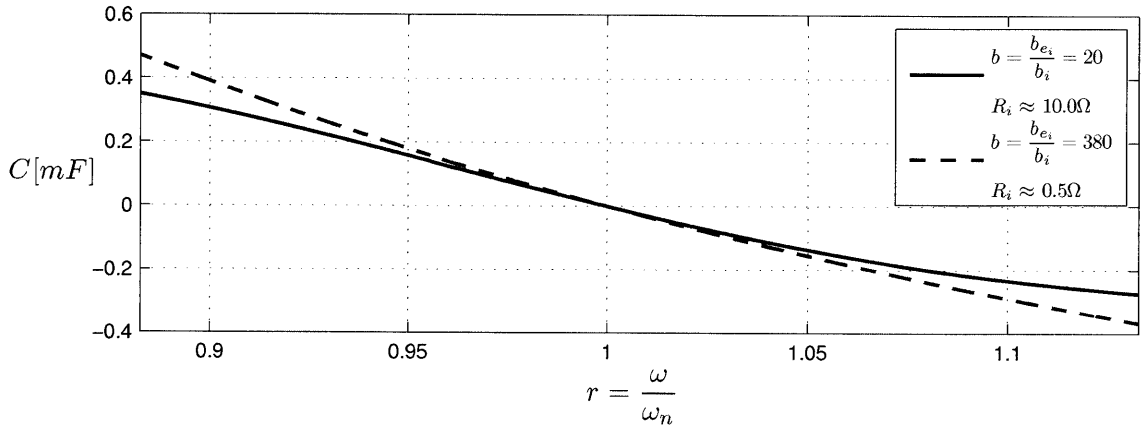

Figure 3-34: *Tuning capacitance as a function of frequency ratio.*

using a capacitor still does not change the natural frequency.

3.3.12 Aside for general solution of K_e and b_e

Governing equation repeated,

$$\ddot{\phi} + \frac{\omega_{n_m}}{Q_i}\dot{\phi} + \omega_{n_m}^2\phi = -\frac{\kappa}{J}i - \ddot{\alpha} \tag{3.177}$$

If

$$\ddot{\alpha} = Re\left[Ae^{j\omega t}\right] \tag{3.178}$$

and,

$$i = Re\left[\left(I_r + I_j j\right)e^{j\omega t}\right] \tag{3.179}$$

then,

$$\phi = -\frac{Q_i}{r\omega_{n_m}\left(1+x^2\right)}\Re\left[\left\{\left[\frac{\kappa}{J}\left(xI_r + I_j\right) + Ax\right] + \left[\frac{\kappa}{J}\left(xI_j - I_r\right) - A\right]j\right\}e^{j\omega t}\right] \tag{3.180}$$

Assuming a torque of the form,

$$T_e = K_e\phi + b_e\dot{\phi} \tag{3.181}$$

Then using the solution for ϕ the torque becomes,

$$\begin{aligned} T_e &= -\frac{Q_i}{\omega_{n_m}}\Re\left[\left\{\left(\frac{K_e}{r\omega_{n_m}}\left[\frac{\kappa}{J}\left(xI_r+I_j\right)+Ax\right]+b_e\left[\frac{\kappa}{J}\left(I_r-xI_j\right)+A\right]\right)\right. \\ &\quad \left.+\left(\frac{K_e}{r\omega_{n_m}}\left[\frac{\kappa}{J}\left(xI_j-I_r\right)-A\right]+b_e\left[\frac{\kappa}{J}\left(xI_r+I_j\right)+Ax\right]\right)j\right\}e^{j\omega t}\Big] \end{aligned} \tag{3.182}$$

In the electrical domain, the torque can be written as,

$$T_e = \kappa i = \kappa\Re\left[\left(I_r + I_j j\right)e^{j\omega t}\right] \tag{3.183}$$

Comparing real and imaginary terms and solving for K_e and b_e results in,

$$K_e = -\frac{J\kappa\omega_{n_m}^2 r}{Q_i}\left(\frac{\kappa x\left(I_r^2+I_j^2\right)+AJ\left(xI_r-I_j\right)}{\kappa^2\left(I_r^2+I_j^2\right)+AJ\left(2\kappa I_r+AJ\right)}\right) \tag{3.184}$$

$$b_e = -\frac{J\kappa\omega_{n_m}}{Q_i}\left(\frac{\kappa\left(I_r^2+I_j^2\right)+AJ\left(I_r+xI_j\right)}{\kappa^2\left(I_r^2+I_j^2\right)+AJ\left(2\kappa I_r+AJ\right)}\right) \tag{3.185}$$

Using the optimal tuning solution,

$$K_e = -\frac{Jr\omega_{n_m}x}{Q_i} \tag{3.186}$$

$$b_e = \frac{\omega_{n_m}J}{Q_i} \tag{3.187}$$

Then the current components are,

$$I_r = -\frac{AJ}{2\kappa} \tag{3.188}$$

$$I_j = I_r x \tag{3.189}$$

Alternately, the passive solution is,

$$K_e = 0 \tag{3.190}$$

$$b_e = \frac{\omega_{n_m} J}{Q_i}\sqrt{1+x^2} \tag{3.191}$$

for which the current components are,

$$I_r = -\frac{AJ}{2\kappa} \tag{3.192}$$

$$I_j = I_r\left(\frac{x}{1+\sqrt{1+x^2}}\right) \tag{3.193}$$

Notice that the real component of the current is the same in both the passive and the active systems.

3.4 Inertial

In the extreme, a fully inertial damper has a flat frequency response. So although an inertial damper does not attenuate any frequencies, it also does not amplify any frequencies, and as is shown below, a resonant system that amplifies some frequencies and attenuates the rest produces more power than a an inertial system.

3.4.1 Spring Mass Damper Model

Using the standard spring-mass-damper model shown in Figure 3-35, and summing the forces on the inertial proof mass, the equation of motion is,

$$\begin{aligned} \sum F &= 0 \\ J\left(\ddot{\phi}+\ddot{\alpha}\right)+\left(b_i+b_e\right)\dot{\phi}+K\phi &= 0 \\ \ddot{\phi}+\frac{b_i+b_e}{J}\dot{\phi}+\frac{K}{J}\phi &= -\ddot{\alpha} \end{aligned} \tag{3.194}$$

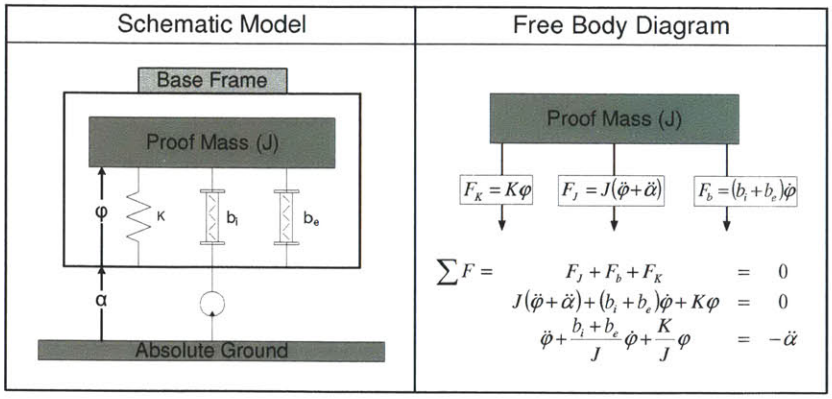

Figure 3-35: *Parameterized diagram of the spring-mass-damper model. The model consists of an inertial proof mass connected to a vibrating reference frame by a spring, an internal damping representing friction and other unavoidable losses, and an electrical damping representing the energy dissipated by the electrical system.*

Representing this equation as a linear system of first order differential equations,

$$\begin{Bmatrix} \dot{\phi} \\ \ddot{\phi} \end{Bmatrix} = \begin{bmatrix} 0 & 1 \\ -\frac{K}{J} & -\frac{b_i+b_e}{J} \end{bmatrix} \begin{Bmatrix} \phi \\ \dot{\phi} \end{Bmatrix} + \begin{Bmatrix} 0 \\ -\ddot{\alpha} \end{Bmatrix} \tag{3.195}$$

The power dissipated electrically is,

$$P = b_e \dot{\phi}^2$$

and the useful harvested power is,

$$P = \frac{1}{2} b_e \dot{\phi}^2 \tag{3.196}$$

3.4.2 Inertial Model

Figure 3-36 is the parameterized diagram of the inertial model. Solving for the forces

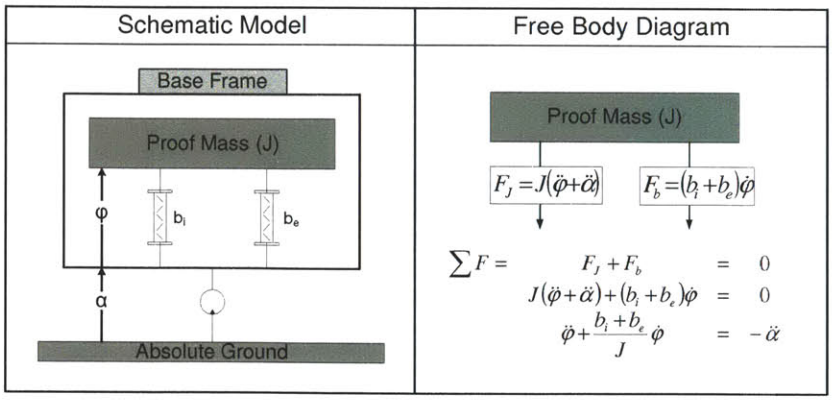

Figure 3-36: *Parameterized diagram of the inertial model. The model consists of an inertial proof mass connected to a vibrating reference frame by an internal damping representing friction and other unavoidable losses, and an electrical damping representing the energy dissipated by the electrical system. Mathematically, this is a special case of the spring-mass-damper system presented earlier with the spring constant set to zero.*

on the proof mass, the governing differential equation is,

$$\begin{aligned} \sum F &= 0 \\ J\left(\ddot{\phi} + \ddot{\alpha}\right) + (b_i + b_e)\,\dot{\phi} &= 0 \\ \ddot{\phi} + \frac{b_i + b_e}{J}\dot{\phi} &= -\ddot{\alpha} \end{aligned} \tag{3.197}$$

Comparing Equations 3.194 and 3.197 we see that the inertial model is a special case of the spring-mass-damper model where the spring constant is set to 0, $K = 0$. Again, to facilitate numerical solution, the equation is split into a system of first order differential equations,

$$\begin{Bmatrix} \dot{\phi} \\ \ddot{\phi} \end{Bmatrix} = \begin{bmatrix} 0 & 1 \\ 0 & -\frac{b_i+b_e}{J} \end{bmatrix} \begin{Bmatrix} \phi \\ \dot{\phi} \end{Bmatrix} + \begin{Bmatrix} 0 \\ -\ddot{\alpha} \end{Bmatrix} \tag{3.198}$$

Again, the useful harvested power is,

$$P = \frac{1}{2} b_e \dot{\phi}^2 \tag{3.199}$$

3.4.3 Ratchet Model

Figure 3-37 is a parameterized diagram of the ratchet system. The ratchet model is

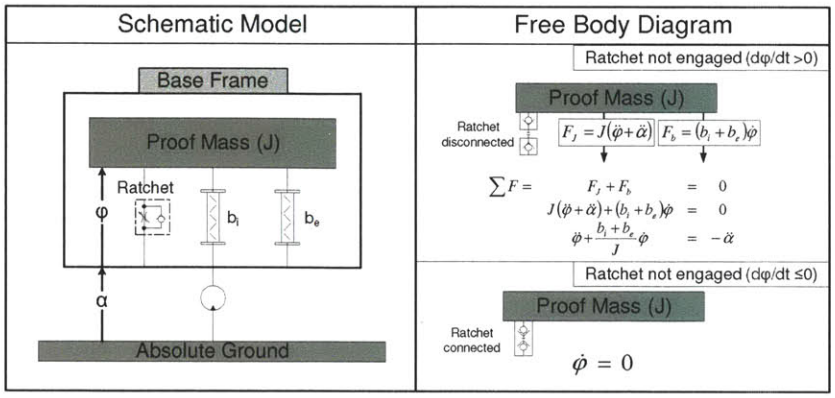

Figure 3-37: *Parameterized diagram of the ratchet model. The model consists of an inertial proof mass connected to a vibrating reference frame by an internal damping representing friction and other unavoidable losses, and an electrical damping representing the energy dissipated by the electrical system, and a ratchet that only allows the proof mass to move in one direction. The ratchet model is mathematically identical to the inertial model when the ratchet is not engaged, but when the ratchet is engaged, the relative velocity of the proof mass is zero since the proof mass is rigidly connected to the moving reference frame.*

the same as the inertial model, but a one-way clutch or ratchet is connected between the proof mass and the moving reference frame. If the reference frame is moving at a velocity that is higher than the velocity of the inertial proof mass (relative velocity less than 0) then the ratchet is engaged and the proof mass is rigidly connected to the moving reference frame which will accelerate the proof mass to the same absolute velocity as the reference frame. As the moving reference frame slows down and reverses directions, the inertia of the proof mass, will allow the proof mass to continue rotating at the highest velocity of the reference frame. However, losses in the bearings and energy harvested from the system will slow the proof mass down. The proof mass will continue to slow down until the relative velocity is less than zero at which time the ratchet will re-engage and the process will repeat. Thus, the proof mass will continue to rotate in one direction relative to the moving reference frame.

Summing the forces on the proof mass, the governing differential equation is,

$$\begin{aligned} \sum F &= 0 \\ J\left(\ddot{\phi}+\ddot{\alpha}\right)+\left(b_i+b_e\right)\dot{\phi} &= 0 \\ \ddot{\phi}+\frac{b_i+b_e}{J}\dot{\phi} &= -\ddot{\alpha} \text{ for } \dot{\phi} \geq 0 \\ \dot{\phi} &= 0 \text{ for } \dot{\phi} < 0 \end{aligned}$$

Which in first order linear form is,

$$\begin{aligned} \begin{Bmatrix} \dot{\phi} \\ \ddot{\phi} \end{Bmatrix} &= \begin{bmatrix} 0 & 1 \\ 0 & -\frac{b_i+b_e}{J} \end{bmatrix} \begin{Bmatrix} \phi \\ \dot{\phi} \end{Bmatrix} + \begin{Bmatrix} 0 \\ -\ddot{\alpha} \end{Bmatrix} \text{ for } \dot{\phi} \geq 0 \\ \dot{\phi} &= 0 \text{ for } \dot{\phi} < 0 \end{aligned} \tag{3.200}$$

Again, the useful harvested power is,

$$P = \frac{1}{2} b_e \dot{\phi}^2 \tag{3.201}$$

3.4.4 Results

Using Matlab's optimization tools, the power of each of the models is maximized. For the simulations, the inertia of the system is assumed to be approximately equal to the inertia estimated by ProEngineer and is given as, $J = 1.496 \times 10^{-5} kg \cdot m^2$. The internal losses are assumed to be primarily in the bearings and are estimated based on an empirical coefficient of friction estimate provided in [16] and is given as, $b_e = 1.00 \times 10^{-4} N \cdot m \cdot s/rad$.

REVISED ESTIMATE OF B_e: In order to estimate the internal damping, the upper torsion spring clamp is removed and a longer solid shaft is protruded out of the top of the device. An optical rotary encoder is attached to the protruding shaft, and measures the rotational velocity of the rotor (figure 3-38). Modeling the forces in the rotor,

$$\ddot{\phi}+\frac{b_i}{J}\dot{\phi} = 0;$$

Thus, the rotational velocity is,

$$\dot{\phi} = \dot{\phi}_0 e^{-\frac{b_i}{J}t} \tag{3.202}$$

A least-squares method is then used to fit this model to the measured data. Figure 3-38 shows the comparison. Matlab's *fminbnd* function is used to optimize the fit,

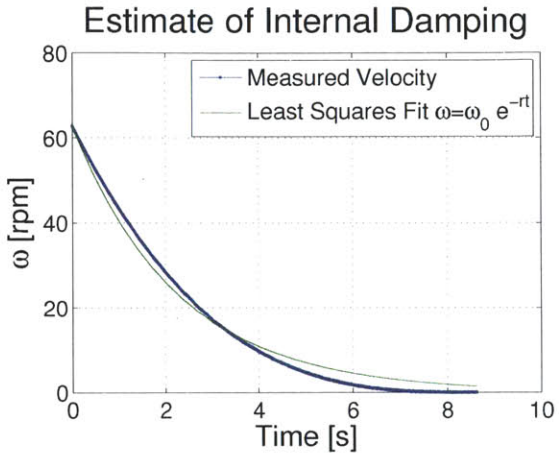

Figure 3-38: *To estimate the internal damping of the system, the rotor is given an initial velocity and allowed to spin freely. Then according to equation 3.202 an exponential curve is fitted to the data to determine an estimate for the damping coefficient.*

and returns a value $b_i = 6.6 \times 10^{-6}$.

The spring-mass-damper model requires a two dimensional search to optimize the power as a function of the spring constant, K, and the electrical damping coefficient, b_e. The optimization tool box function *fmincon(func,initial,boundaries)* is used where the function to be optimized calculates the power by solving equations 3.195 and 3.196 numerically using a 4^{th} order Runga-Kutta Method adapted from [6]; K initial is set so the natural frequency corresponds to the frequency of maximum amplitude in the input, and b_e initial equal b_i; and the boundaries on K are from 0 to a value that provides a natural frequency of $200Hz$, and the constraints on b_e are arbitrary choosen to bracket the internal damping by an order of magnitude in both directions.

The inertial and ratchet models are single parameter optimizations of power as a function of b_e, and thus the simpler optimization tool box function *fminbnd(func,boundaries)* is used where the function the numerical solution (same method as spring-mass-damper) of equations 3.198 and 3.199 for the inertial model and 3.200 and 3.201 for

the ratchet model, and the boundaries are again an order of magnitude bracketing of b_i.

Figure 3-39 displays the results of the optimization simulation for each of the

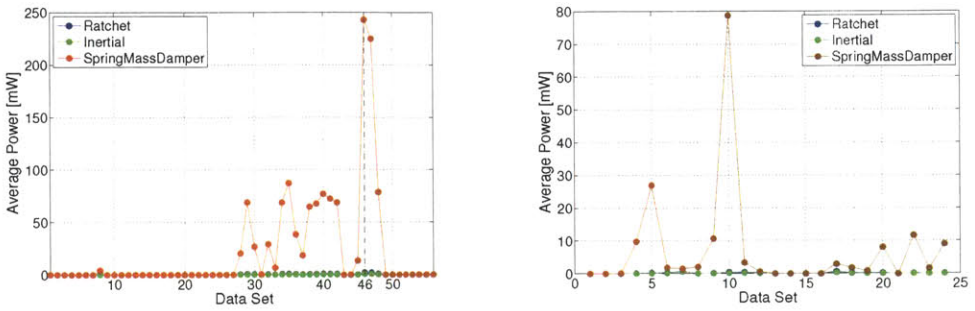

Figure 3-39: *Simulated maximum average harvested power for a ratchet, an inertial, and a spring-mass-damper model for each of the provided acceleration inputs. NOTE: each input is optimized separately.*

provided inputs. In most cases, the spring-mass-damper model is expected to harvest more power than the inertial model, which is expected to harvest more power than the ratchet model.

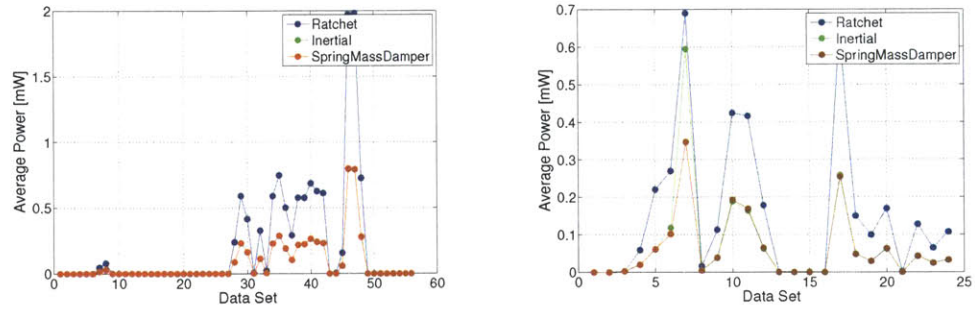

Figure 3-40: *Simulated maximum average harvested power for a ratchet, an inertial, and a spring-mass-damper model for each of the provided acceleration inputs. NOTE: a single K and b_e are optimized for all inputs.*

To further study the relationship, figure 3-41 plots the maximum output power of the optimizations against each other. Each of the data points represents the power in one model vs the power in the other model for a particular input. In figure 3-41(a), the spring-mass-damper model is compared to the inertial model, and shows

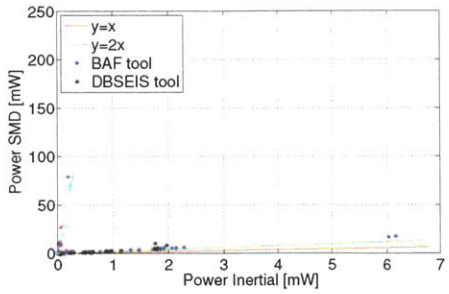

(a) Comparison of inertial and spring-mass-damper

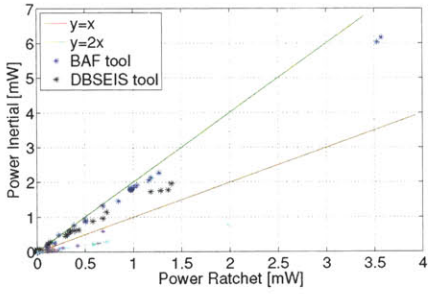

(b) Comparison of inertial and ratchet

Figure 3-41: *Comparison of the simulated maximum average power. (a) shows that an optimized spring-mass-damper model will make more power than the inertial model for all the provided inputs, and will typically make more than twice the power of the inertial system. (b) shows that the inertial model produces more power for all of the inputs than a rachet model since all the input data points are above the $y = x$ line.*

in general the spring-mass-damper model is expected to produce a little more than twice the power as the inertial model. In 3-41(b) the inertial and ratchet models are compared. Since the ratchet system is essentially the same as the inertial system but only moves in one direction, the power of the inertial system might be expected to be twice the power of the ratchet system; however, the comparison of power shows the inertial system provides somewhat less than twice the power of the ratchet system indicating that the ratchet is providing some rectification.

However, a key benefit of the ratchet system is the relative displacement.

To illustrate the previous misconceptions of the various models, take a closer look at the 46^{th} input trace indicated in figure 3-39. As can be seen using the optimization tools, the spring-mass-damper system provides more than double the power of the inertial model. Thus, focusing on the 46^{th} trace, figure 3-42 is a graph of the angular acceleration amplitude as a function of time and frequency. As can be seen, this particular trace exhibits a large resonant peak and the majority of the remaining amplitude is less than 5% of the amplitude of the resonant peak which from previous studies suggests that a resonant spring-mass-damper system will be able to resonate and be the best choice. Originally, a graphical search method was used in which the

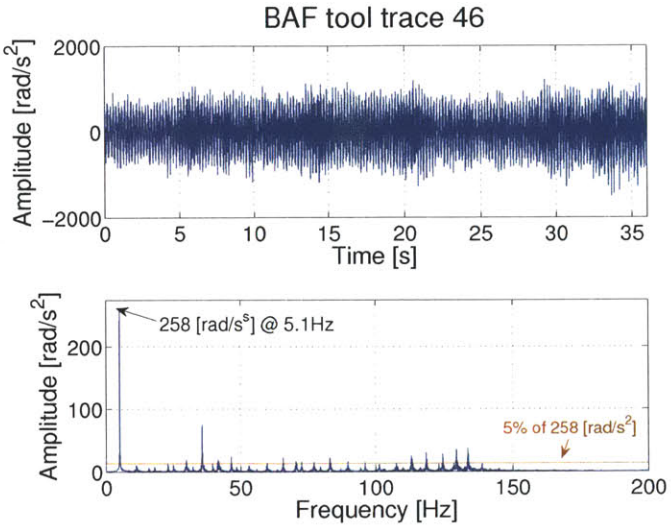

Figure 3-42: *Graph of the 46^{th} input of the BAF tool as a function of time and frequency.*

spring-mass-damper equations were solved for a range of K and b_e values as in figure 3-45 However, in initial searches, a resonant frequency range of 100Hz was used to define the limits on K and in 3-43(a). For this level of discritization, the maximum power occurs at $K = 0$ and is equivalent to the maximum power solved in the inertial model. Later, after comparison with the optimization results of figure 3-39 a finer graphical search as in 3-43(b) does in fact find that a spring mass damper is optimal with a 5Hz resonant frequency is optimal.

Describing the anthology of this error is useful for two reasons. First, to explain why the inertial model (or ratchet system) was originally thought to be superior to the spring-mass-damper model. Second, to illustrate the sensitivity of a spring-mass-damper model to the value of K. In figure 3-43(c), the range of K has been reduce to the equivalent of 7Hz search area to obtain the same numerical value as the optimization. Thus, the output of the spring-mass-damper is sensitive to the value of K. Figure 3-44 is a plot of the power as function of relative K and shows that a 60% error in the value of K can be allowed for a fixed damping coefficient before the inertial system would create more power. It is of interest to note that for this one particular input which is relatively narrow bandwidth, if the quality factor could be

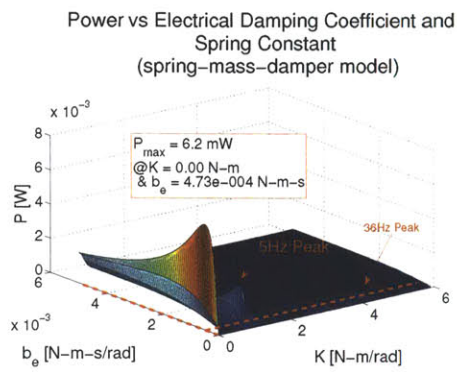

(a) K range 100Hz

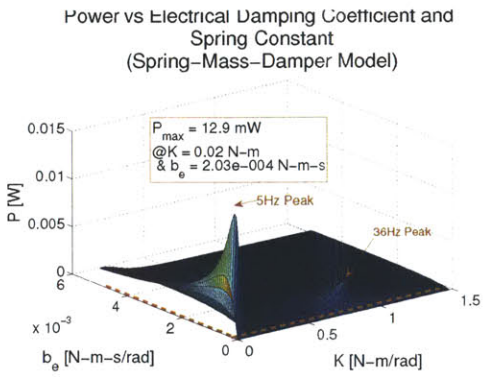

(b) K range 50Hz

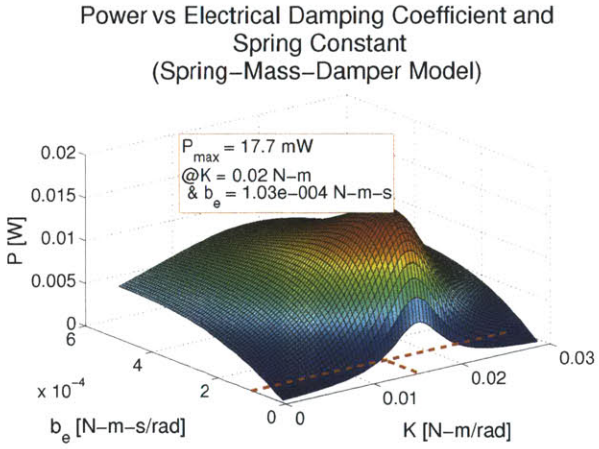

(c) K range 7Hz, Note: the range on b_e has also been reduced.

Figure 3-43: *The predicted output power as a function of K and b_e. The power is extremely dependent on the value of K as can be seen by the increasingly finer search grids. In (a) the maximum power is for a resonant system; however, as the grid is refined, in (b) the maximum power is now more accurately found at 5Hz. To get an accurate prediction of the optimal K requires a very fine search grid (as in (c)), which suggests that the power is sensitive to changes in K. Note, the optimal damping coefficient is equivalent to the internal damping as predicted in previous studies, $b_e = b_i$*

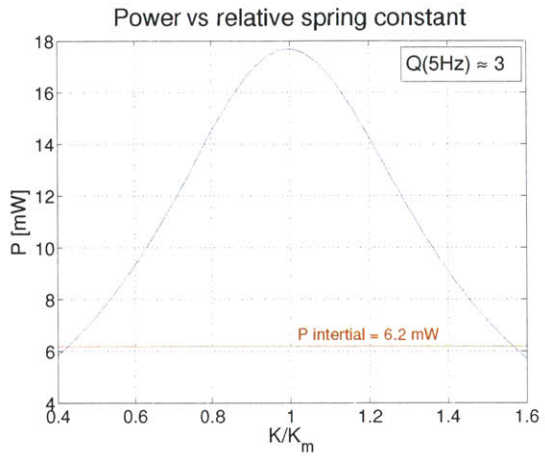

Figure 3-44: *Plot of the sensitivity of power to changes in spring constant*

increased at 5Hz to 50, then the average power output would be 0.25 W, but only a 10% change in K would be required before a resonant system would be superior.

As noted in the modeling section, the inertial and ratchet models are mathematically identical except for the non-linear ratchet, so when the ratchet is not engaged the models should predict similar power, however, when the ratchet is engaged and no relative velocity exists and the harvested power is zero nearly half the time. This explains why the ratchet model produces half the power of the inertial model. However, in earlier comparison studies, the inertial model was not explicitly studied and was only used when the spring mass damper model predicted (usually incorrectly) that it was optimal. In these cases, the simulations choose the ratchet model as the better alternative for electromagnetic reasons. In the original models the electrical damping was modeled as a torque created by the generator as in reality and not as a simplified viscous damping coefficient. Thus, dimensional considerations are taken into account. Figure ?? shows the displacement and velocity of the inertial and ratchet models for the 46^{th} trace. In 3-45(a) the relative displacement of the inertial system is limited to approximately 10 deg, while the relative displacement of the ratchet system has seen a full rotation within 2 seconds. The magnetic circuit for the inertial system with such small displacements is difficult and prone to losses, and since the relative velocity in both cases (3-45(b)) is similar, all be it one sided, the original simulations

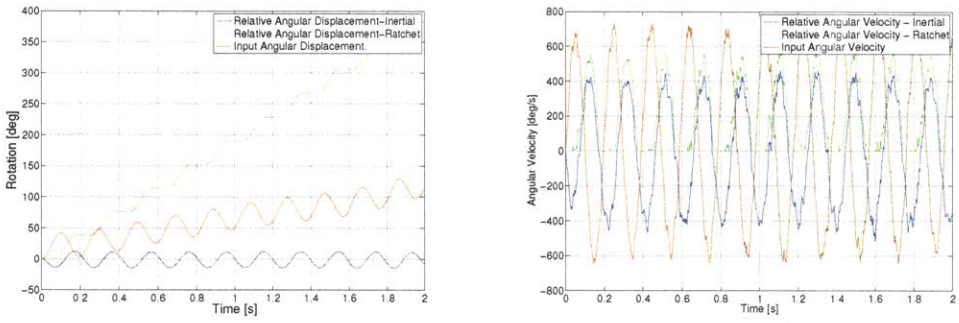

(a) Angular Displacement

(b) Angular Velocity

Figure 3-45: *Comparison of relative angular displacement and velocity for the inertial and ratchet models.*

predicted the ratchet system as superior.

As a first order check, using the inertial system as and example, the maximum relative velocity is $\dot{\phi}_{max} \approx 400 deg/s$, which results in a maximum electrical damping torque of $T \approx .7N - mm$. In the prototype this torque is applied at a lever arm of $13.3mm$ which results in a force of $F \approx 0.5N$ applied of an area of $6 \times 10^{-3} m^2$ for a electrical shear stress of $\tau = 0.001 psi$ which should be obtainable. Thus, the previous model of the electrical torque will need to be reviewed and either corrected or used to verify the assertion that the continuous rotation in the ratchet system provides sufficient benefit electro-magnetically to deem the ratchet system superior to the inertial.

Chapter 4

Rotational Prototype

Input Parameters

The system is subject to some physical parameters. Figure 4-1 shows the constraints.

- $0 \leq K \leq 5,000 \quad \frac{N}{m}$
- $0 \leq b_e \leq 250 \quad \frac{N-s}{m}$
- $r_{mag} = 0.375 \quad in$
- $0.1 \leq h \leq 2 \quad in$

  $$m = \rho_{mag} \pi r_{mag}^2 h$$

- $Q_i = 100$

  $$b_i = \frac{\sqrt{Km}}{Q_i}$$

The maximum extracted power is optimized using a brute force optimization technique where the power is plotted as a function of the spring constant and electrical damping while independently varying h (and thus indirectly the mass).

Parameters

- $h = 0.53 \quad in$

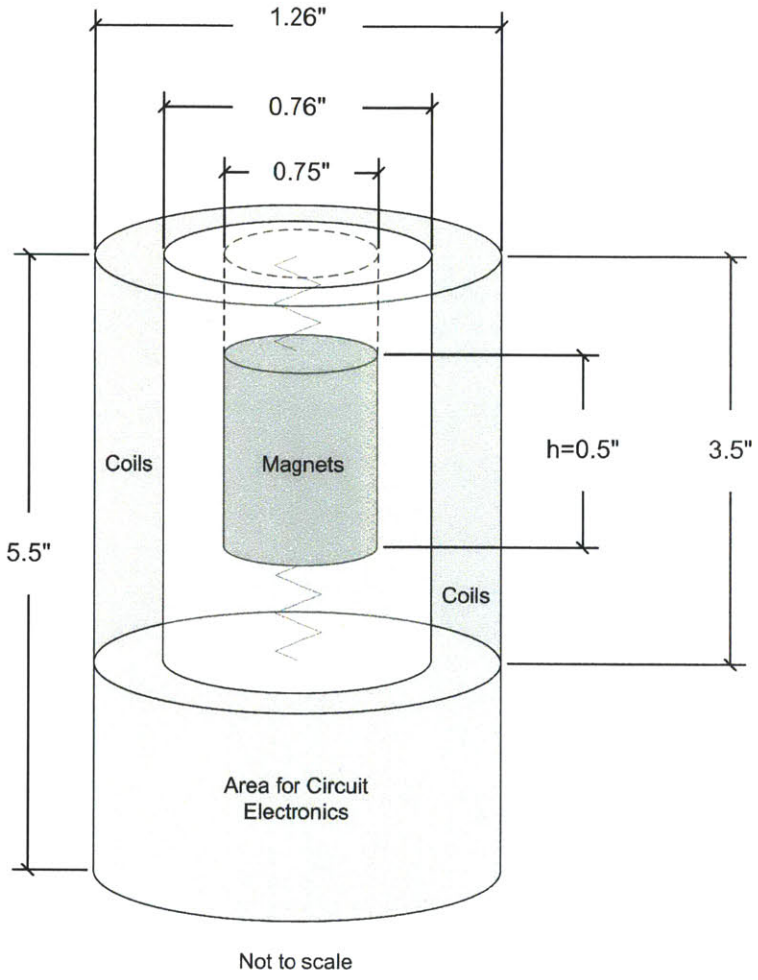

Figure 4-1: *Physical parameters of the system*

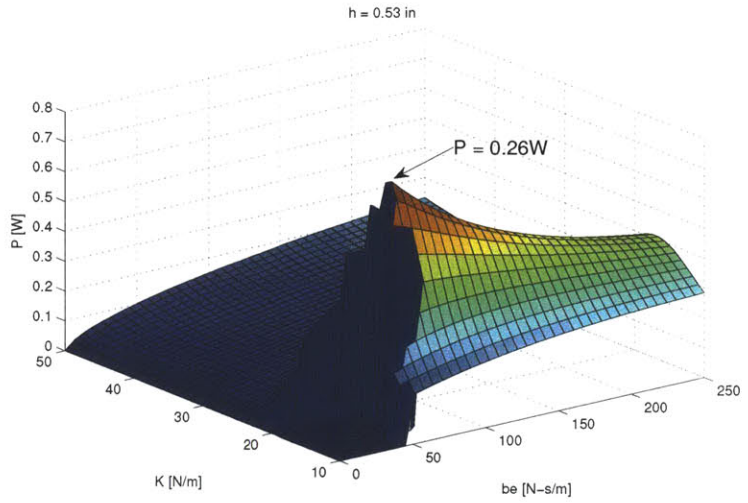

Figure 4-2: *Expected power at a magnet mass width of 0.25in as a function of the internal spring constant K and the total electrical damping factor including power extraction and electrical losses. Note, the system is displacement limited and further power improvements could be made by either a non-linear spring or active control of the electrical damping.*

- $K = 28 \quad \frac{N}{m}$
- $b_e = 78 \quad \frac{N-s}{m}$

$\tau_e = 1.6 \quad psi$

NOTE: The power is displacement limited as can be seen by in the plot. In the model when any parameter exceeds its maximum value the power is set to 0 to indicate inadmissible operation. The power would not actually be 0 at this location but the magnets would be hitting the stops. The maximum power can be improved by including control over the electrical damping (optimal control model) or including a non-linear spring that will gradually stiffen when approaching the limits allowing the device to operate in this range. These options are currently being modeled to determine which is optimal.

Several wrist watches have been successfully powered (or wound) by rotating proof masses[?], but in those instances, the frequency of vibration is very low (0.5–2 Hz), and the amplitude of vibration is several orders of magnitude larger than the size of the device. Thus, the majority of the work is done by the relative change in the

direction of the gravitational field associated with such large amplitude changes and not the relative motion produced by inertial forces on the proof mass. To the authors' knowledge, what is not available, is a macro scale device capable of harvesting the higher frequency (5–100 Hz) but much lower amplitude vibrations of rotating machinery in varying attitudes. As explained by [20], most proposed methods of transduction have similar maximum potential power densities and thus the choice is often application specific. Combining these results with the estimates of [?], electromagnetic induction is chosen as the best method of transduction for this device based on expected mechanical vibrations and form factor restraints. Thus, presented here are the design and performance of a *rotational, macro-scale, energy harvester.* The harvester uses a rotating spring-"mass"-damper that can be directly connected to a rotational system subjected to torsional vibration and through electromagnetic induction, harvest the potential energy of those vibrations.

4.1 Spring Constant

4.2 Internal Damping

4.3 Electro-magnetics

Building on the calculation of the open circuit flux density, the next step is to calculate the open circuit voltage, often referred to as the electromotive force (EMF).

4.3.1 Modeling

Conductors are arranged around the stator as shown in Figure 4-3. According to Faraday's law of induction, as the rotor moves relative to the stator the changing magnetic flux passing through the coils will induce a voltage,

$$\varepsilon = -\frac{d\lambda_B}{dt}$$

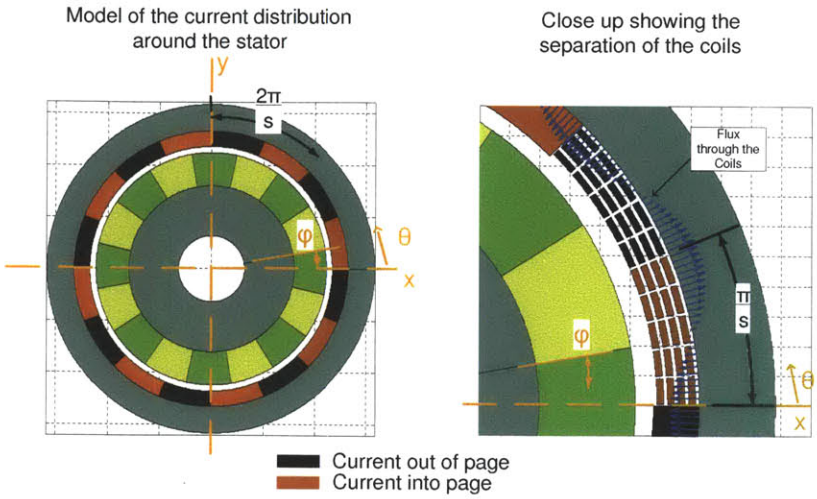

Figure 4-3: *Schematic of the current distribution on the stator. The current travels out-of (black) or into (red) the page and connects into an equivalent loop above and below the page. Thus, a series of equivalent loops are created that are spaced π/s apart where s represents the number of loops. The current is carried in conductors that are distributed on the stator as shown in the zoomed in schematic. α represents the angular offset between turns.*

where ε is the induced voltage (or EMF) and λ_B is the total magnetic flux through the coils. The flux through a single turn of the coil is defined as,

$$
\begin{aligned}
\lambda_{coil} &= \int \tilde{\mathbf{B}} \cdot \mathbf{d\tilde{a}} \\
&= \int_{z=0}^{h} \int_{\theta'=\theta}^{\theta+\frac{\pi}{s}} \tilde{\mathbf{B}} \cdot r\hat{\mathbf{e}}_r \quad d\theta' dz \\
&= \int_{z=0}^{h} \int_{\theta'=\theta}^{\theta+\frac{\pi}{s}} rB_r \quad d\theta' dz \\
&= \int_{z=0}^{h} \int_{\theta'=\theta}^{\theta+\frac{\pi}{s}} -\frac{2B_R r_m \left[\left(\frac{r_m}{r_{ic}}\right)^{n_k} - \left(\frac{r_{ic}}{r_m}\right)^{n_k}\right]\left[\left(\frac{r}{r_{oc}}\right)^{n_k} + \left(\frac{r_{oc}}{r}\right)^{n_k}\right]}{\pi(2k-1)\left[\left(\frac{r_{ic}}{r_{oc}}\right)^{n_k} - \left(\frac{r_{oc}}{r_{ic}}\right)^{n_k}\right]} \sin\left(n_k(\theta' - \phi)\right) \quad d\theta' dz \\
&= \int_{\theta'=\theta}^{\theta+\frac{\pi}{s}} -\frac{2hB_R r_m \left[\left(\frac{r_m}{r_{ic}}\right)^{n_k} - \left(\frac{r_{ic}}{r_m}\right)^{n_k}\right]\left[\left(\frac{r}{r_{oc}}\right)^{n_k} + \left(\frac{r_{oc}}{r}\right)^{n_k}\right]}{\pi(2k-1)\left[\left(\frac{r_{ic}}{r_{oc}}\right)^{n_k} - \left(\frac{r_{oc}}{r_{ic}}\right)^{n_k}\right]} \sin\left(n_k(\theta' - \phi)\right) \quad d\theta' \\
&= \int_{\theta'=\theta}^{\theta+\frac{\pi}{s}} -b \sin\left(n_k(\theta' - \phi)\right) \quad d\theta' \\
&= b\,\frac{1}{n_k} \cos\left(n_k(\theta' - \phi)\right)\Big|_{\theta'=\theta}^{\theta'=\theta+\frac{\pi}{s}} \qquad 127 \\
&= \frac{b}{n_k}\left[\cos\left(n_k(\theta + \frac{\pi}{s} - \phi)\right) - \cos\left(n_k(\theta - \phi)\right)\right] \qquad (4.1)
\end{aligned}
$$

To account for multiple turns, a turns density function is included in the formulation,

$$\lambda_B = \int_{\theta'=\theta}^{\theta+\frac{\pi}{s}} \eta(\theta')\lambda_{coil}(\theta') \quad d\theta' \tag{4.2}$$

where $\eta(\theta)$ is the solution of,

$$\int_{\theta=0}^{\frac{\pi}{s}} \eta(\theta) \quad d\theta = N$$

where N is the total number of turns. Figure 4-3 shows that the turns distribution is a square function, thus,

$$\eta = \frac{Ns}{\pi}$$

Thus,

$$\begin{aligned}
\lambda &= \int_{\theta'=\theta}^{\theta+\frac{\pi}{s}} \frac{Ns}{\pi}\frac{b}{n_k}\left[\cos\left(n_k(\theta'+\frac{\pi}{s}-\phi)\right)-\cos\left(n_k(\theta'-\phi)\right)\right] \quad d\theta' \\
&= \frac{Nsb}{n_k^2\pi}\left[\sin\left(n_k(\theta'+\frac{\pi}{s}-\phi)\right)-\sin\left(n_k(\theta'-\phi)\right)\right]_{\theta'=\theta}^{\theta+\frac{\pi}{s}} \\
&= \frac{Nsb}{n_k^2\pi}\left[\sin\left(n_k(\theta+\frac{2\pi}{s}-\phi)\right)-2\sin\left(n_k(\theta+\frac{\pi}{s}-\phi)\right)+\sin\left(n_k(\theta-\phi)\right)\right]
\end{aligned} \tag{4.3}$$

Summing up all the coils,

$$\lambda_B = \sum_{j=0}^{s-1} \frac{Nsb}{n_k^2\pi}\left[\sin\left(n_k(\frac{2j\pi}{s}+\frac{2\pi}{s}-\phi)\right)-2\sin\left(n_k(\frac{2j\pi}{s}+\frac{\pi}{s}-\phi)\right)+\sin\left(n_k(\frac{2j\pi}{s}-\phi)\right)\right]$$

Up to this point it has been assumed that the magnet pitch $(2\pi/p)$ and the coil pitch $(2\pi/s)$ are different. However, if $s \neq p$ then $\lambda_B = 0$ (Proof is in Appendix ??, Section 4.3.3). Thus, the current pitch and magnet pitch must be equal and setting s equal

to p from now on,

$$\begin{aligned}
\lambda_B &= \sum_{j=0}^{p-1} \frac{Npb}{n_k^2\pi} \left\{ \left[-\cos\left(\frac{n_k}{s}(2j\pi + 2\pi)\right) + 2\cos\left(\frac{n_k}{s}(2j\pi + \pi)\right) - \cos\left(\frac{n_k}{s}(2j\pi)\right) \right] \sin(n_k\phi) \right. \\
&\qquad \left. + \left[\sin\left(\frac{n_k}{s}(2j\pi + 2\pi)\right) - 2\sin\left(\frac{n_k}{s}(2j\pi + \pi)\right) + \sin\left(\frac{n_k}{s}(2j\pi)\right) \right] \cos(n_k\phi) \right\} \\
&= \sum_{j=0}^{p-1} \frac{Npb}{n_k^2\pi} \left\{ \left[-\cos\left((2k-1)(j+1)2\pi\right) + 2\cos\left((2k-1)(2j+1)\pi\right) - \cos\left((2k-1)j2\pi\right) \right] \sin(n_k\phi) \right. \\
&\qquad \left. + \left[\sin\left((2k-1)(j+1)2\pi\right) - 2\sin\left((2k-1)(2j+1)\pi\right) + \sin\left((2k-1)(j+1)2\pi\right) \right] \cos(n_k\phi \right. \\
&= \sum_{j=0}^{p-1} \frac{Npb}{n_k^2\pi} \left\{ \left[-(1) + 2(-1) - (1) \right] \sin(n_k\phi) + \left[(0) - 2(0) + (0) \right] \cos(n_k\phi) \right\} \\
&= \sum_{j=0}^{p-1} -4\frac{Npb}{n_k^2\pi} \sin(n_k\phi) \\
&= -4\frac{Np^2b}{n_k^2\pi} \sin(n_k\phi) \\
&= -\lambda_0 \sin(n_k\phi) \qquad (4.
\end{aligned}$$

where,

$$\lambda_0 = \frac{8NhB_R r_m \left[\left(\frac{r_m}{r_{ic}}\right)^{n_k} - \left(\frac{r_{ic}}{r_m}\right)^{n_k} \right] \left[\left(\frac{r}{r_{oc}}\right)^{n_k} + \left(\frac{r_{oc}}{r}\right)^{n_k} \right]}{\pi^2(2k-1)^3 \left[\left(\frac{r_{ic}}{r_{oc}}\right)^{n_k} - \left(\frac{r_{oc}}{r_{ic}}\right)^{n_k} \right]}$$

Applying the chain rule to Faraday's law of induction, the induced voltage (ε) can be solved for as,

$$\begin{aligned}
\varepsilon &= -\frac{d\lambda_B}{dt} \\
&= -\frac{d\lambda_B}{d\phi}\frac{d\phi}{dt} \\
&= \lambda_0 n_k \cos\left(n_k\phi\right)\dot{\phi}
\end{aligned}$$

If the current is separated into multiple phases that are assumed to be equally spaced, the induced voltage is shifted in space in proportion to the number of phases. Thus, the induced voltage in the a^{th} phase is,

$$\varepsilon_a = \lambda_0 n_k \cos\left(n_k\phi + \frac{2\pi(a-1)}{A}\right)\dot{\phi} \qquad (4.5)$$

where A is the total number of phases.

Equation 4.5 is incorporated into Matlab for numerical calculations and the code is provided in Appendix ??, Section A.0.10.

4.3.2 Results

Combined with the numerical values in table 4.2, Table 4.1 lists the numerical values used to calculate the induced voltage,

Variable	Value	Unit	Description
s	8		Number of coil pole pairs
N	32		Number of turns in the coil
r	0.525	in	Radial dimension to the flux surface ($r = r_{oc}$)
	13.3	mm	
h	3.0	in	Axial dimension
	76.2	mm	
a	1		Phase number
A	1		Total number of coil phases

Table 4.1: *Values used in the calculation of the induced voltage*

Initially, assume the rotor to be rotating at a constant rate,

$$\dot{\phi} = \omega$$

Thus, the angular displacement is a linear function of time,

$$\phi = \omega t + C \tag{4.6}$$

For simplicity, assume $\phi|_{t=0} = 0$, thus, $C = 0$ and,

$$\begin{aligned} \phi(t) &= \omega t \\ \dot{\phi}(t) &= \omega \end{aligned}$$

Applying ϕ and $\dot{\phi}$ to Equation 4.5, Figure 4-4 shows the induced voltage.

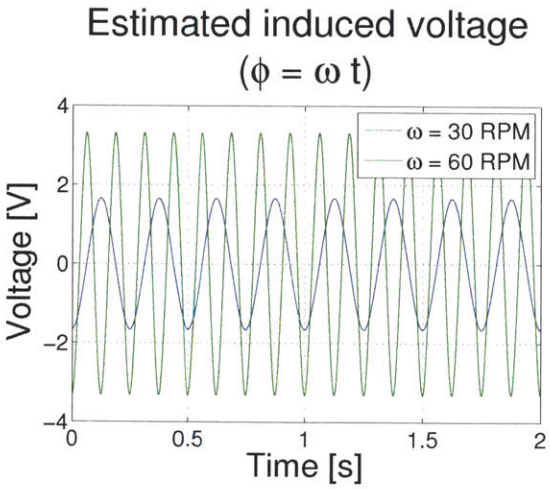

Figure 4-4: *Plot of the calculated induced voltage (EMF) for a constant angular velocity input to an 8 pole, single phase, 32 turn, electric machine with dimension defined by Figure ?? and Table ??*

An oscillatory input better matches the expected input. Thus, assuming an input of,

$$\begin{aligned} \phi(t) &= \Phi \sin(\omega t) + \phi_0 \\ \dot{\phi}(t) &= \Phi\omega \cos(\omega t) \end{aligned}$$

the induced voltage is shown for two different initial positions and a three different sinusoidal amplitudes in Figure 4-5. In each of the above cases, the radius at which

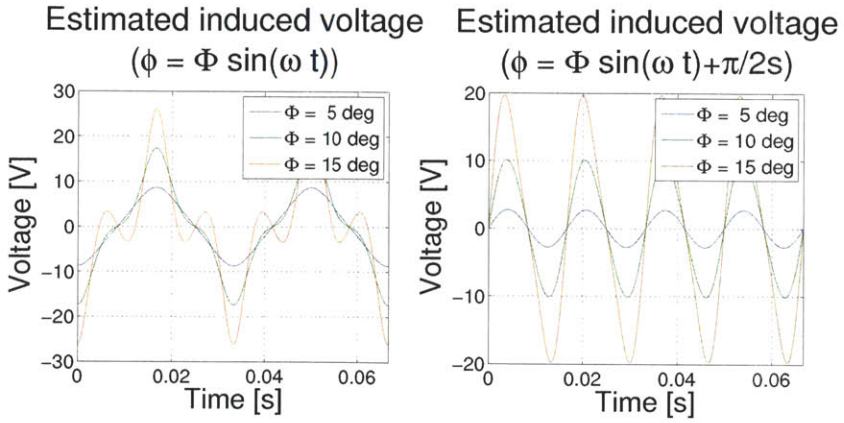

Figure 4-5: *Plot of the calculated induced voltage (EMF) for a sinusoidal angular displacement input.*

the flux is evaluated is assumed to be the same as the outer core. This provides a conservative estimate of the induced voltage since some of the coils are closer to the surface of the magnet and see a higher flux density.

4.3.3 Solution of $\lambda_B = 0$ for $s \neq p$

When the magnetic pitch $(2\pi/s)$ and the current pitch $(2\pi/p)$ are assumed to be different, that is $s \neq p$, the total flux through the coils λ_B must be 0 ($\lambda_B = 0$ for $s \neq p$). The following section shows the steps in the mathematical proof of this starting with the general solution for the flux

$$\begin{aligned}\lambda_B &= \sum_{j=0}^{s-1} \lambda_0 \left[\sin\left(n_k(\frac{2j\pi}{s} + \frac{2\pi}{s} - \phi)\right) - 2\sin\left(n_k(\frac{2j\pi}{s} + \frac{\pi}{s} - \phi)\right) + \sin\left(n_k(\frac{2j\pi}{s} - \phi)\right)\right] \\ &= \sum_{j=0}^{s-1} \lambda_0 \, []\end{aligned}$$

The next step in the analysis is to assume a load. Based on the load, the expected current and power can be calculated.

4.3.4 Modeling

The simplest circuit that provides a reasonable approximation for the amount of power that can be extracted from the system is to assume the load can be modeled like an equivalent resistance (Figure 4-6). The harvested power is then equivalent to the power dissipated in the load resistor.

$$\begin{aligned}P &= i_{R_L} V_{R_L} \\ &= \frac{V_{R_L}^2}{R_L} \\ &= \frac{\left(\frac{R_L}{R_L + R_c}\varepsilon\right)^2}{R_L} \\ &= \frac{R_L}{(R_L + R_c)^2}\varepsilon^2\end{aligned}$$

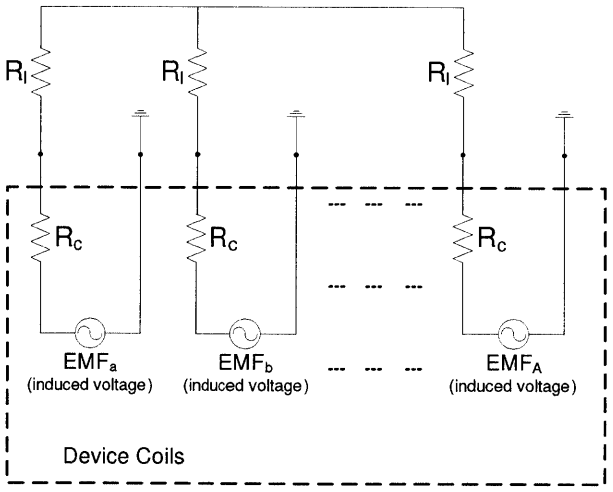

Figure 4-6: *Equivalent circuit diagram of the coil and equivalent load resistance.*

Optimizing the harvested power as a function of the load resistance,

$$\begin{aligned} \frac{dP}{dR_L} = -\frac{R_L - R_c}{(R_L + R_c)^3}\varepsilon^3 &= 0 \\ R_L &= R_c \end{aligned}$$

Thus, to maximize the harvested power, the load resistance should be matched to the coil resistance,

$$P = \frac{\varepsilon^2}{4R_c}$$

Extending this to multiple phases, the power is the sum of the power in each phase.

$$P = \frac{1}{4R_c}\sum_{a=1}^{A}\varepsilon_a^2 \tag{4.7}$$

To determine the equivalent damping coefficient, combine Equations 4.5 and 4.7,

$$\begin{aligned} P &= \frac{1}{4R_c}\sum_{a=1}^{A}\left[\lambda_0 n_k \cos\left(n_k\phi + \frac{2\pi(a-1)}{A}\right)\dot{\phi}\right]^2 \\ &= \frac{\lambda_0^2 n_k^2 \dot{\phi}^2}{4R_c}\sum_{a=1}^{A}\cos^2\left(n_k\phi + \frac{2\pi(a-1)}{A}\right) \\ &= \frac{\lambda_0^2 n_k^2 \dot{\phi}^2}{4R_c}\begin{cases} \cos^2(n_k\phi) & A=1 \\ 2\cos^2(n_k\phi) & A=2 \\ \frac{A}{2} & A>2 \end{cases} \end{aligned} \tag{4.8}$$

Thus, the equivalent damping coefficient is,

$$b_e = = \frac{\lambda_0^2 n_k^2}{4R_c}\begin{cases} \cos^2(n_k\phi) & A=1 \\ 2\cos^2(n_k\phi) & A=2 \\ \frac{A}{2} & A>2 \end{cases} \tag{4.9}$$

NOTE: THIS IS NOT EXACTLY CORRECT, b_e IN THE VIBRATION EQUATIONS IS ALL THE ENERGY DISSIPATED BY THE ELECTRIC SYSTEM. I BELIEVE BASED ON THE PREVIOUS ASSUMPTIONS THAT THE TOTAL ENERGY DISSIPATED ELECTRICALLY IS TWICE THE ENERGY HARVESTED, BUT I WILL NEED TO DOUBLE CHECK. EITHER WAY, THE ACTUAL ELECTRIC DAMPING COEFFICIENT IS A LITTLE DIFFERENT PROBABLY TWICE THE HARVESTED DAMPING COEFFICIENT.

To calculate the harvested power, a model of the coil resistance is needed. According to [?] the resistance in a conductor can be estimated by,

$$R = \frac{\ell\rho}{A}$$

where ℓ is the length, ρ is the materials resistivity, and A is the cross sectional area.

The total coil resistance consists of a sum of the active conductor resistance, consisting of the conductor paths arranged axial around the stator in the region of magnetic flux; and the end-turn conductor resistance, consisting of the conductor paths that connect the active conductors at either end of the device. The resistance of one complete loop is connected in series with the resistance Np loops. Since, multiple-phase are assumed to be matched, the resistance in phase a is $R_a = R_1/A$ where R_1 is the total resistance of a single phase system, resulting in a total coil resistance of,

$$R_a = \frac{Np}{A}\rho\left(\frac{\ell_{\text{active}}}{A_{\text{active}}} + \frac{\ell_{\text{et}}}{A_{\text{et}}}\right)$$

The conductor length of the active section is twice the active axial length of the coil, $\ell_{\text{active}} = 2h$. Assuming an approximately square profile wire with a given insulation thickness (as in Figure 4-6), the active cross-section area is,

$$A_{\text{active}} = t_{\text{layer}}\left(\frac{r\pi}{n_t s} - k_t\right)$$

where t_{layer} is the flexible circuit printed copper thickness, and the active length is,

The length of the end-turns is shown in Figure 4-7, and one complete turn consists of 4 lengths. The cross-sectional area of the end-turns can be estimated by scaling the active area by the angle $\theta = \arctan\left(\frac{2s(z-h)}{r\pi}\right)$,

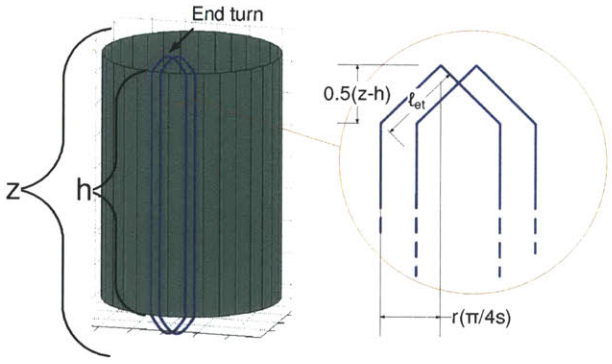

$$\ell_{et} = \sqrt{\left(\frac{z-h}{2}\right)^2 + \left(r\frac{\pi}{4s}\right)^2}$$

Figure 4-7: *Estimation of the end-turn length for calculation of the coil resistance.*

$$A_{\text{end-turns}} = \sin(\theta) A_{\text{active}}$$

Thus, the coil resistance is,

$$R = \frac{NP\rho}{AA_{\text{active}}} \left(2h + \frac{\ell_{et}}{\sin(\theta)} \right)$$

Given this model,

$$= \frac{\lambda_0^2 n_k^2 \dot{\phi}^2}{4R_c} \begin{cases} \cos^2(n_k\phi) & A = 1 \\ 2\cos^2(n_k\phi) & A = 2 \\ \frac{A}{2} & A > 2 \end{cases} \tag{4.10}$$

A Matlab function is provided in Appendix **??**, Section A.0.9 to calculate the resistance.

4.3.5 Results

The first step in the design of an electric generator is the open-circuit fields analysis. The following documents the modeling and calculation of the magnetic field in a multi-pole rotational permanent magnet electric machine.

4.3.6 Modeling

The device to be analyzed is a permanent magnet generator, and the schematic that the model is based on is shown in Figure 4-8. The device is a relatively standard magnetic-shear type permanent-magnet machine. The system consists of 2p permanent magnets arranged radially around a rotor core. The magnets are permanently magnetized in either the plus (north) or minus (south) radial direction ($\tilde{\mathbf{M}} \propto \pm\hat{\mathbf{e}}_r$).

To obtain a model of the machine a few simplifying assumptions are imposed. First, the axial dimension is assumed to be at least 3 times larger than the diameter

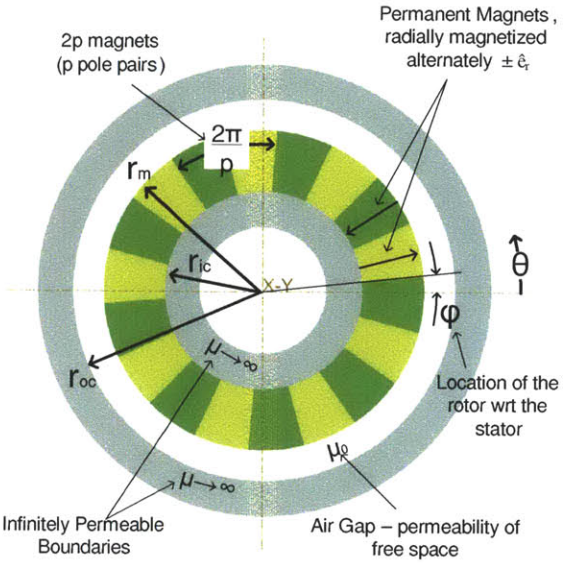

Figure 4-8: *Representative axial cross-section of electric machine. The model consists of 2p permanent magnets attached to an infinitely permeable rotor. The magnets are magnetized radially and arranged in an alternating North-South arrangement* ($\tilde{\mathbf{M}} \propto \pm\hat{\mathbf{e}}_r$)*. The rotor is surrounded by an infinitely permeable, stationary stator.*

of the outer core, and several orders of magnitude larger than the width of the air gap between the magnets face and outer core, a 2-dimensional model is sufficient. Second, the fields are assumed to be small enough in the permeable materials that the materials can be assumed infinitely permeable.

The solution of the magnetic flux density in the air gap ($\tilde{\mathbf{B}}$ field) starts with the quasi-static version of the Ampere-Maxwell law in differential form[32].

$$\tilde{\nabla} \times \tilde{\mathbf{H}} = \tilde{\mathbf{J}}_{free}$$

In an open-circuit fields analysis, no currents free currents exist in the model, and the Ampere-Maxwell law reduces to,

$$\tilde{\nabla} \times \tilde{\mathbf{H}} = \mathbf{0}$$

and thus, the magnetic field intensity ($\tilde{\mathbf{H}}$) can be written as the gradient of a scalar

potential ψ,

$$\tilde{\mathbf{H}} = -\nabla\psi \tag{4.11}$$

Equation 4.11 and the general accepted constitutive law, $\tilde{\mathbf{B}} = \mu_0\left(\tilde{\mathbf{H}} + \tilde{\mathbf{M}}\right)$ are then substituted into Gauss' law for magnetic fields [32],

$$\begin{aligned}
\tilde{\nabla}\cdot\tilde{\mathbf{B}} &= \mathbf{0} \\
\tilde{\nabla}\cdot\mu_0\left(\tilde{\mathbf{H}}+\tilde{\mathbf{M}}\right) &= \mathbf{0} \\
\tilde{\nabla}\cdot\left(\tilde{\mathbf{H}}+\tilde{\mathbf{M}}\right) &= \mathbf{0} \\
\tilde{\nabla}\cdot\tilde{\mathbf{H}}+\tilde{\nabla}\cdot\tilde{\mathbf{M}} &= \mathbf{0} \\
\tilde{\nabla}\cdot\tilde{\mathbf{H}} &= -\tilde{\nabla}\cdot\tilde{\mathbf{M}} \\
\tilde{\nabla}\cdot(-\nabla\psi) &= -\tilde{\nabla}\cdot\tilde{\mathbf{M}} \\
\tilde{\nabla}\cdot(\nabla\psi) &= \tilde{\nabla}\cdot\tilde{\mathbf{M}} \\
\nabla^2\psi &= \tilde{\nabla}\cdot\tilde{\mathbf{M}}
\end{aligned} \tag{4.12}$$

To further reduce the equation, the distribution of magnetization can be mathematically described by a fourier series,

$$\tilde{\mathbf{M}} = \begin{cases} \displaystyle\sum_{k=1}^{\infty} M_0 \frac{4}{\pi}\frac{r_m}{r}\frac{\sin\left[p\left(2k-1\right)\left(\theta-\psi\right)\right]}{2k-1}\,\hat{\mathbf{e}}_r & r_{ic} < r < r_m \\ 0 & r_m < r < r_{oc} \end{cases}$$

where in reference to Figure 4-8, r_m is the radial distance to the outer surface of the magnets, r is the radial coordinate, p is the number of pole pairs, θ represents the angular coordinate, and ϕ represents the rotation of the rotor with respect to the coordinate system. Treating the two regions defined by the magnetization vector separately, in the region of free space between the magnets and the outer magnetic core the magnetization vector is zero, and thus Equation 4.12 simplifies to Laplace's

equation,

$$\nabla^2 \psi_a = 0 \tag{4.13}$$

where the a subscript denotes the potential in the "air" region.

In the area filled by magnets, the divergence of the magnetization vector is,

$$\begin{aligned} \tilde{\nabla} \cdot \tilde{\mathbf{M}} &= \frac{1}{r}\frac{\partial}{\partial r}(rM_r) \\ &= \frac{1}{r}\frac{\partial}{\partial r}\left(r\sum_{k=1}^{\infty} M_0 \frac{4}{\pi}\frac{r_m}{r}\frac{\sin\left[p\left(2k-1\right)\left(\theta-\phi\right)\right]}{2k-1}\right) \\ &= 0 \end{aligned}$$

Substituting this into Equation 4.12 again results in Laplace's equation

$$\nabla^2 \psi_m = 0 \tag{4.14}$$

where the m subscript denotes the potential in the "magnet" region.

The solution of Laplace's equation in cylindrical coordinates can be obtain in most electromagnetic texts, and is given in general as,

$$\psi = \sum_{k=1}^{\infty} r^{n_k}\left[A_{1_k}\sin\left(n_k\beta\right) + A_{2_k}\cos\left(n_k\beta\right)\right] + r^{-n_k}\left[A_{3_k}\sin\left(n_k\beta\right) + A_{4_k}\cos\left(n_k\beta\right)\right] \tag{4.15}$$

where $\theta - \phi \equiv \beta$ and $p(2k-1) \equiv n_k$ are used to simplify and shorten the expressions.

Solve for the constants by using the boundary conditions imposed on the fields. Start with the outer boundary at $r = r_{oc}$. From the Ampere-Maxwell law, in the absence of a free surface current (as assumed earlier), the tangential component of the field intensity must be continuous. Additionally, since the outer core material is assumed to be infinitely permeable, the field intensity inside the core material must

be zero. Thus,

$$\begin{aligned}
\hat{\mathbf{e}}_r \times \left(-\tilde{\mathbf{H}}_a \Big|_{r=r_{oc}} \right) &= \mathbf{0} \\
-H_{a_\theta}|_{r=r_{oc}} &= 0 \\
\frac{1}{r_{oc}} \frac{\partial \psi_a}{\partial \theta}\Big|_{r=r_{oc}} &= 0 \\
\frac{\partial \psi_a}{\partial \theta}\Big|_{r=r_{oc}} &= 0
\end{aligned}$$

Performing the integration and dropping the summation notation for simplicity,

$$\left(r_{oc}^{n_k} A_{a1_k} + r_{oc}^{-n_k} A_{a3_k}\right) \cos\left(n_k \beta\right) - \left(r_{oc}^{n_k} A_{a2_k} + r_{oc}^{-n_k} A_{a4_k}\right) \sin\left(n_k \beta\right) = 0$$

Since this must hold true for all values of β, the result is two equations which can be used to solve for the constants

$$\begin{bmatrix} r_{oc}^{n_k} & 0 & r_{oc}^{-n_k} & 0 \\ 0 & r_{oc}^{n_k} & 0 & r_{oc}^{-n_k} \end{bmatrix} \begin{Bmatrix} A_{a1_k} \\ A_{a2_k} \\ A_{a3_k} \\ A_{a4_k} \end{Bmatrix} = \begin{Bmatrix} 0 \\ 0 \end{Bmatrix}$$

Similarly, at the inner core,

$$\begin{aligned}
\hat{\mathbf{e}}_r \times \left(\tilde{\mathbf{H}}_m \Big|_{r=r_{ic}} \right) &= \mathbf{0} \\
H_{m_\theta}|_{r=r_{ic}} &= 0 \\
-\frac{1}{r_{ic}} \frac{\partial \psi_m}{\partial \theta}\Big|_{r=r_{ic}} &= 0 \\
\frac{\partial \psi_m}{\partial \theta}\Big|_{r=r_{ic}} &= 0
\end{aligned}$$

Again performing the integration and also dropping the summation for visual simplicity,

$$\left(r_{ic}^{n_k} A_{1_m} + r_{ic}^{-n_k} A_{3_m}\right) \cos\left(n_k \beta\right) - \left(r_{ic}^{n_k} A_{2_m} + r_{ic}^{-n_k} A_{4_m}\right) \sin\left(n_k \beta\right) = 0 \qquad (4.16)$$

Again, since this must hold for all values of β, the result is two equations for the constants.

$$\begin{bmatrix} r_{ic}^{n_k} & 0 & r_{ic}^{-n_k} & 0 \\ 0 & r_{ic}^{n_k} & 0 & r_{ic}^{-n_k} \end{bmatrix} \begin{Bmatrix} A_{m1_k} \\ A_{m2_k} \\ A_{m3_k} \\ A_{m4_k} \end{Bmatrix} = \begin{Bmatrix} 0 \\ 0 \end{Bmatrix}$$

Applying the same boundary condition to the interface between the magnet and the air,

$$\begin{aligned} \hat{\mathbf{e}}_\mathbf{r} \times \left(\tilde{\mathbf{H}}_a \Big|_{r=r_m} - \tilde{\mathbf{H}}_m \Big|_{r=r_m} \right) &= \mathbf{0} \\ H_{a_\theta}|_{r=r_m} - H_{m_\theta}|_{r=r_m} &= 0 \\ -\frac{1}{r_m} \left(\frac{\partial \psi_a}{\partial \theta} \Big|_{r=r_m} - \frac{\partial \psi_m}{\partial \theta} \Big|_{r=r_m} \right) &= 0 \\ \frac{\partial \psi_a}{\partial \theta} \Big|_{r=r_m} - \frac{\partial \psi_m}{\partial \theta} \Big|_{r=r_m} &= 0 \end{aligned}$$

After integration this becomes,

$$\begin{aligned} &\left[r_m^{n_k} \left(A_{a1_k} - A_{m1_k} \right) + r_m^{-n_k} \left(A_{a3_k} - A_{m3_k} \right) \right] \cos\left(n_k \beta \right) \\ &- \left[r_m^{n_k} \left(A_{a2_k} - A_{m2_k} \right) + r_m^{-n_k} \left(A_{a4_k} - A_{m4_k} \right) \right] \sin\left(n_k \beta \right) = 0 \end{aligned}$$

which again provides 2 equations for the constants,

$$\begin{bmatrix} r_m^{n_k} & 0 & r_m^{-n_k} & 0 & -r_m^{n_k} & 0 & -r_m^{-n_k} & 0 \\ 0 & r_m^{n_k} & 0 & r_m^{-n_k} & 0 & -r_m^{n_k} & 0 & -r_m^{-n_k} \end{bmatrix} \begin{Bmatrix} A_{a1_k} \\ A_{a2_k} \\ A_{a3_k} \\ A_{a4_k} \\ A_{m1_k} \\ A_{m2_k} \\ A_{m3_k} \\ A_{m4_k} \end{Bmatrix} = \begin{Bmatrix} 0 \\ 0 \end{Bmatrix}$$

The final boundary condition is determined by applying Gauss' law at the magnet-air interface. From Gauss' law, the normal component of the magnetic flux density must be continuous.

$$\begin{aligned}
\hat{\mathbf{e}}_r \cdot \left(\tilde{\mathbf{B}}_a\Big|_{r=r_m} - \tilde{\mathbf{B}}_m\Big|_{r=r_m} \right) &= \mathbf{0} \\
B_{a_r}|_{r=r_m} - B_{m_r}|_{r=r_m} &= 0 \\
\mu_0 \, H_{a_r}|_{r=r_m} - \mu_0 \left(H_{m_r} + M_r\right)|_{r=r_m} &= 0 \\
H_{a_r}|_{r=r_m} - H_{m_r}|_{r=r_m} &= M_r|_{r=r_m} \\
\frac{\partial \psi_a}{\partial r}\bigg|_{r=r_m} - \frac{\partial \psi_m}{\partial r}\bigg|_{r=r_m} &= -\, M_r|_{r=r_m}
\end{aligned}$$

After integration and substitution,

$$\begin{aligned}
&\left[r_m^{n_k}\left(A_{a2_k} - A_{m2_k}\right) + r_m^{-n_k}\left(-A_{a4_k} + A_{m4_k}\right)\right]\cos(n_k\beta) \\
&+ \left[r_m^{n_k}\left(A_{a1_k} - A_{m1_k}\right) + r_m^{-n_k}\left(-A_{a3_k} + A_{m3_k}\right)\right]\sin(n_k\beta) \;=\; -\frac{4M_0 r_m}{\pi n_k(2k-1)}\sin(n\beta)
\end{aligned}$$

Which again yields 2 equations,

$$\begin{bmatrix}
r_m^{n_k} & 0 & -r_m^{-n_k} & 0 & -r_m^{n_k} & 0 & r_m^{-n_k} & 0 \\
0 & r_m^{n_k} & 0 & -r_m^{-n_k} & 0 & -r_m^{n_k} & 0 & r_m^{-n_k}
\end{bmatrix}
\begin{Bmatrix}
A_{a1_k} \\ A_{a2_k} \\ A_{a3_k} \\ A_{a4_k} \\ A_{m1_k} \\ A_{m2_k} \\ A_{m3_k} \\ A_{m4_k}
\end{Bmatrix}
=
\begin{Bmatrix}
-\frac{4M_0 r_m}{\pi n_k(2k-1)} \\ 0
\end{Bmatrix}$$

Combining all the equations,

$$\begin{bmatrix} r_{oc}^{n_k} & 0 & r_{oc}^{-n_k} & 0 & 0 & 0 & 0 & 0 \\ 0 & r_{oc}^{n_k} & 0 & r_{oc}^{-n_k} & 0 & 0 & 0 & 0 \\ 0 & 0 & 0 & 0 & r_{ic}^{n_k} & 0 & r_{ic}^{-n_k} & 0 \\ 0 & 0 & 0 & 0 & 0 & r_{ic}^{n_k} & 0 & r_{ic}^{-n_k} \\ r_m^{n_k} & 0 & r_m^{-n_k} & 0 & -r_m^{n_k} & 0 & -r_m^{-n_k} & 0 \\ 0 & r_m^{n_k} & 0 & r_m^{-n_k} & 0 & -r_m^{n_k} & 0 & -r_m^{-n_k} \\ r_m^{n_k} & 0 & -r_m^{-n_k} & 0 & -r_m^{n_k} & 0 & r_m^{-n_k} & 0 \\ 0 & r_m^{n_k} & 0 & -r_m^{-n_k} & 0 & -r_m^{n_k} & 0 & r_m^{-n_k} \end{bmatrix} \begin{Bmatrix} A_{a1_k} \\ A_{a2_k} \\ A_{a3_k} \\ A_{a4_k} \\ A_{m1_k} \\ A_{m2_k} \\ A_{m3_k} \\ A_{m4_k} \end{Bmatrix} = \begin{Bmatrix} 0 \\ 0 \\ 0 \\ 0 \\ 0 \\ 0 \\ -\frac{4M_0 r_m}{n_k \pi (2k-1)} \\ 0 \end{Bmatrix}$$

Matlab is used to solve the system of equations (code provided in Appendix ?? Section A.0.13),

$$\begin{Bmatrix} A_{a1_k} \\ A_{a2_k} \\ A_{a3_k} \\ A_{a4_k} \\ A_{m1_k} \\ A_{m2_k} \\ A_{m3_k} \\ A_{m4_k} \end{Bmatrix} = \frac{2M_0 r_m}{n_k \pi (2k-1) \left(\left(\frac{r_{oc}}{r_{ic}} \right)^{n_k} - \left(\frac{r_{ic}}{r_{oc}} \right)^{n_k} \right)} \begin{Bmatrix} \frac{1}{r_{oc}^{n_k}} \left(\left(\frac{r_{ic}}{r_m} \right)^{n_k} - \left(\frac{r_m}{r_{ic}} \right)^{n_k} \right) \\ 0 \\ -r_{oc}^{n_k} \left(\left(\frac{r_{ic}}{r_m} \right)^{n_k} - \left(\frac{r_m}{r_{ic}} \right)^{n_k} \right) \\ 0 \\ \frac{1}{r_{ic}^{n_k}} \left(\left(\frac{r_{oc}}{r_m} \right)^{n_k} - \left(\frac{r_m}{r_{oc}} \right)^{n_k} \right) \\ 0 \\ -r_{ic}^{n_k} \left(\left(\frac{r_{oc}}{r_m} \right)^{n_k} - \left(\frac{r_m}{r_{oc}} \right)^{n_k} \right) \\ 0 \end{Bmatrix}$$

Thus, the potential solution for the two regions is,

$$\begin{Bmatrix} \psi_a \\ \\ \psi_m \end{Bmatrix} = \frac{2M_0 r_m}{n_k \pi (2k-1)} \sin(n_k \beta) \begin{Bmatrix} \frac{\left[\left(\frac{r}{r_{oc}} \right)^{n_k} - \left(\frac{r_{oc}}{r} \right)^{n_k} \right] \left[\left(\frac{r_m}{r_{ic}} \right)^{n_k} - \left(\frac{r_{ic}}{r_m} \right)^{n_k} \right]}{\left(\frac{r_{ic}}{r_{oc}} \right)^{n_k} - \left(\frac{r_{oc}}{r_{ic}} \right)^{n_k}} \\ \\ \frac{\left[\left(\frac{r}{r_{ic}} \right)^{n_k} - \left(\frac{r_{ic}}{r} \right)^{n_k} \right] \left[\left(\frac{r_m}{r_{oc}} \right)^{n_k} - \left(\frac{r_{oc}}{r_m} \right)^{n_k} \right]}{\left(\frac{r_{ic}}{r_{oc}} \right)^{n_k} - \left(\frac{r_{oc}}{r_{ic}} \right)^{n_k}} \end{Bmatrix}$$

The $\tilde{\mathbf{H}}$ field in the air gap is then,

$$\begin{aligned}
\tilde{\mathbf{H}}_a &= -\nabla\psi_a \\
&= -\left(\frac{\partial\psi_a}{\partial r}\hat{\mathbf{e}}_r + \frac{1}{r}\frac{\partial\psi_a}{\partial\theta}\hat{\mathbf{e}}_\theta\right) \\
&= -\frac{2M_0 r_m\left[\left(\frac{r_m}{r_{ic}}\right)^{n_k} - \left(\frac{r_{ic}}{r_m}\right)^{n_k}\right]}{\pi r(2k-1)\left[\left(\frac{r_{ic}}{r_{oc}}\right)^{n_k} - \left(\frac{r_{oc}}{r_{ic}}\right)^{n_k}\right]} \begin{Bmatrix} \left[\left(\frac{r}{r_{oc}}\right)^{n_k} + \left(\frac{r_{oc}}{r}\right)^{n_k}\right]\sin(n_k\beta) \\ \\ \left[\left(\frac{r}{r_{oc}}\right)^{n_k} - \left(\frac{r_{oc}}{r}\right)^{n_k}\right]\cos(n_k\beta) \end{Bmatrix}
\end{aligned} \tag{4.17}$$

and the $\tilde{\mathbf{B}}$ field in the air gap is,

$$\begin{aligned}
\tilde{\mathbf{B}}_a &= \mu_0\tilde{\mathbf{H}}_a \\
&= -\frac{2\mu_0 M_0 r_m\left[\left(\frac{r_m}{r_{ic}}\right)^{n_k} - \left(\frac{r_{ic}}{r_m}\right)^{n_k}\right]}{\pi r(2k-1)\left[\left(\frac{r_{ic}}{r_{oc}}\right)^{n_k} - \left(\frac{r_{oc}}{r_{ic}}\right)^{n_k}\right]} \begin{Bmatrix} \left[\left(\frac{r}{r_{oc}}\right)^{n_k} + \left(\frac{r_{oc}}{r}\right)^{n_k}\right]\sin(n_k\beta) \\ \\ \left[\left(\frac{r}{r_{oc}}\right)^{n_k} - \left(\frac{r_{oc}}{r}\right)^{n_k}\right]\cos(n_k\beta) \end{Bmatrix}
\end{aligned} \tag{4.18}$$

and in the magnetic region,

$$\begin{aligned}
\tilde{\mathbf{H}}_m &= -\nabla\psi_m \\
&= -\left(\frac{\partial\psi_m}{\partial r}\hat{\mathbf{e}}_r + \frac{1}{r}\frac{\partial\psi_m}{\partial\theta}\hat{\mathbf{e}}_\theta\right) \\
&= -\frac{2M_0 r_m\left[\left(\frac{r_m}{r_{oc}}\right)^{n_k} - \left(\frac{r_{oc}}{r_m}\right)^{n_k}\right]}{\pi r(2k-1)\left[\left(\frac{r_{ic}}{r_{oc}}\right)^{n_k} - \left(\frac{r_{oc}}{r_{ic}}\right)^{n_k}\right]} \begin{Bmatrix} \left[\left(\frac{r}{r_{ic}}\right)^{n_k} + \left(\frac{r_{ic}}{r}\right)^{n_k}\right]\sin(n_k\beta) \\ \\ \left[\left(\frac{r}{r_{ic}}\right)^{n_k} - \left(\frac{r_{ic}}{r}\right)^{n_k}\right]\cos(n_k\beta) \end{Bmatrix}
\end{aligned} \tag{4.19}$$

$$
\begin{aligned}
\tilde{\mathbf{B}}_m &= \mu_0\left(\tilde{\mathbf{H}}_m + \tilde{\mathbf{M}}\right) \\
&= \mu_0\left[\left\{\begin{array}{c} H_r \\ H_\theta \end{array}\right\} + \left\{\begin{array}{c} M_r \\ 0 \end{array}\right\}\right] \\
&= \mu_0\left[-\frac{2M_0 r_m\left[\left(\frac{r_m}{r_{oc}}\right)^{n_k} - \left(\frac{r_{oc}}{r_m}\right)^{n_k}\right]}{\pi r(2k-1)\left[\left(\frac{r_{ic}}{r_{oc}}\right)^{n_k} - \left(\frac{r_{oc}}{r_{ic}}\right)^{n_k}\right]}\left\{\begin{array}{l} \left[\left(\frac{r}{r_{ic}}\right)^{n_k} + \left(\frac{r_{ic}}{r}\right)^{n_k}\right]\sin\left(n_k\beta\right) \\ \\ \left[\left(\frac{r}{r_{ic}}\right)^{n_k} - \left(\frac{r_{ic}}{r}\right)^{n_k}\right]\cos\left(n_k\beta\right) \end{array}\right\}\right. \\
&\qquad \left. + \quad \frac{4M_0 r_m}{\pi r\left(2k-1\right)}\left\{\begin{array}{c} \sin\left(n_k\beta\right) \\ 0 \end{array}\right\}\right] \\
&= -\frac{2\mu_0 M_0 r_m}{\pi r(2k-1)}\left\{\begin{array}{l} \left[\frac{\left[\left(\frac{r_m}{r_{oc}}\right)^{n_k} - \left(\frac{r_{oc}}{r_m}\right)^{n_k}\right]\left[\left(\frac{r}{r_{ic}}\right)^{n_k} + \left(\frac{r_{ic}}{r}\right)^{n_k}\right]}{\left(\frac{r_{ic}}{r_{oc}}\right)^{n_k} - \left(\frac{r_{oc}}{r_{ic}}\right)^{n_k}} - 2\right]\sin\left(n_k\beta\right) \\ \\ \frac{\left[\left(\frac{r_m}{r_{oc}}\right)^{n_k} - \left(\frac{r_{oc}}{r_m}\right)^{n_k}\right]\left[\left(\frac{r}{r_{ic}}\right)^{n_k} - \left(\frac{r_{ic}}{r}\right)^{n_k}\right]}{\left(\frac{r_{ic}}{r_{oc}}\right)^{n_k} - \left(\frac{r_{oc}}{r_{ic}}\right)^{n_k}}\cos\left(n_k\beta\right) \end{array}\right\}
\end{aligned}
\tag{4.20}
$$

4.3.7 Results

Table 4.2 contains the numerical values used in the calculations of the results. The

Variable	Value	Unit	Description
μ_0	$4\pi \times 10^{-7}$	$\frac{henry}{m} \equiv \frac{kgm}{A^2 s^2}$	Magnetic permeability of free space[32]
B_R	1.29	T	residual flux density[1]
r_{oc}	0.525	in	Radial dimension to inner surface of the outer permeable material
	13.3	mm	
r_m	0.440	in	Radial dimension to outer surface of magnets
	11.2	mm	
r_{ic}	0.315	in	Radial dimension to outer surface of the inner permeable material
	8.00	mm	
p	8		number of pole pairs

Table 4.2: *Values used in the calculation of the results (*NOTE *for radial dimensions see Figure 4-8)*

strength of rare earth magnets is typically given in terms of the residual flux density (B_R), which is related to the remanence (M_0) by, $B_R = \mu_0 M_0$ (note: notationally, B_R denotes residual flux density and B_r denotes the radial component of the flux

density).

The exact solution requires an infinite sum; however, for realistic numerical simulations an estimate of the number of terms need for reasonable convergence of the series is determined numerical by comparing the change in the radial component of the flux density at the outer core for successive summation terms. The radial component at the outer core is used since this is the component and location most relevant to the calculation of the open circuit voltage (EMF). Thus, the radial flux density evaluated at the outer core is,

$$B_r|_{r=r_{oc}} = -\frac{4B_R r_m}{\pi r_{oc}(2k-1)} \frac{\left(\frac{r_m}{r_{ic}}\right)^{n_k} - \left(\frac{r_{ic}}{r_m}\right)^{n_k}}{\left(\frac{r_{ic}}{r_{oc}}\right)^{n_k} - \left(\frac{r_{oc}}{r_{ic}}\right)^{n_k}} \sin(n_k\beta)$$

Figure 4-9 is a plot of the radial flux density evaluated at the outer core ($B_r|_{r=r_{oc}}$) for increasing values of k. Also plotted is the root mean square of the relative error of the radial flux for increasing values of k ($\text{RMS}\left[B_r(k) - B_r(k-1)\right]$). As can be seen, for the numerical values chosen, the series converges very quickly, with a relative error on the order of 4×10^{-3} at the second term of the summation. For each successive simulation, a section of the code used to produce these plots (provided in Appendix ?? Section A.0.14) is include to determine the number of summation terms necessary for convergence by requiring a minimum relative rms error.

Finally, based on Equations 4.18 and 4.20, a vector plot of the flux density is shown in Figure 4-10. The matlab code used to calculate the vector field is given in Appendix ?? Section A.0.15.

As the number of coil turns reduces, the width of the copper bars increases and the losses associated with eddy currents increases. According to Faraday's law

$$\oint \tilde{\mathbf{E}} \cdot d\tilde{\mathbf{l}} = \int -\frac{\partial \tilde{\mathbf{B}}}{\partial t} \cdot d\tilde{\mathbf{s}} \tag{4.21}$$

As seen in figs. (4-11) and (4-12), ignoring fringing fields (which are small in the bars and occur primarily in the end turns) and due to symmetry the electric field is

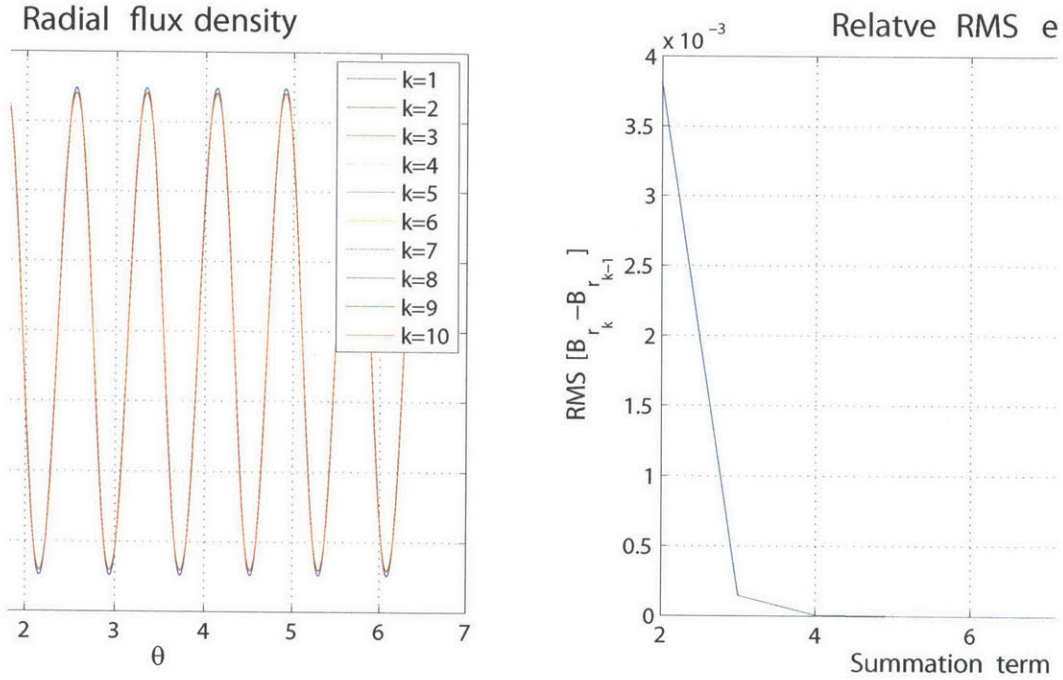

Figure 4-9: *Plot of the radial flux density evaluated at the outer core ($B_r|_{r=r_{oc}}$) for increasing values of k and the relative rms error between successive terms in the summation. As can be seen, for the numerical values used, 4 terms should be sufficient for convergence of the infinite summation.*

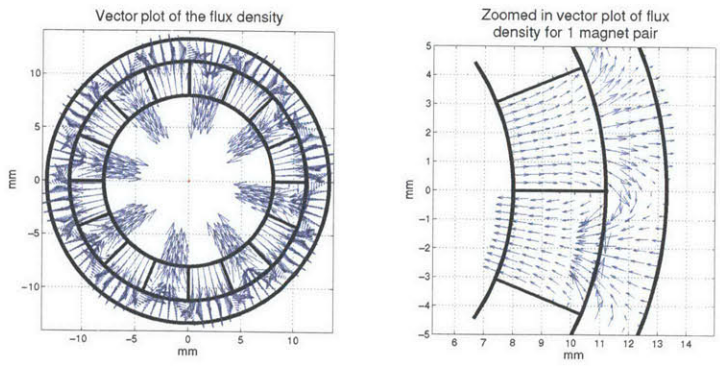

Figure 4-10: *Vector plot of the flux density* ($\tilde{\mathbf{B}}$).

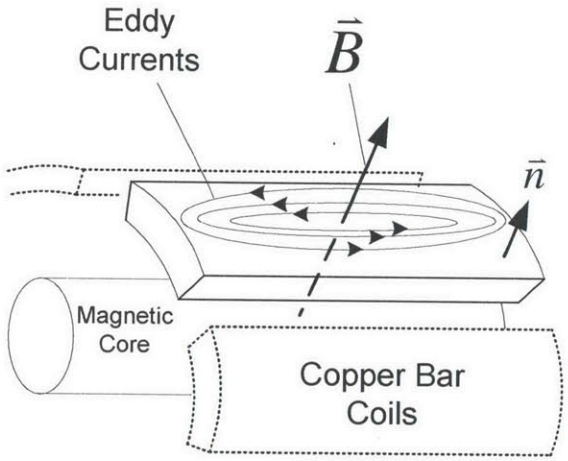

Figure 4-11: *Radially directed magnetic fields passing through the copper bars create circulating currents*

constant around the closed loop thus,

$$\oint \tilde{\mathbf{E}} \cdot d\tilde{\mathbf{l}} = 2E\,(L + w) \approx 2EL \tag{4.22}$$

where the assumption $L >> w$ has been used in the approximation. Again ignoring fringing the magnetic field does not vary axially, however the field does vary angularly,

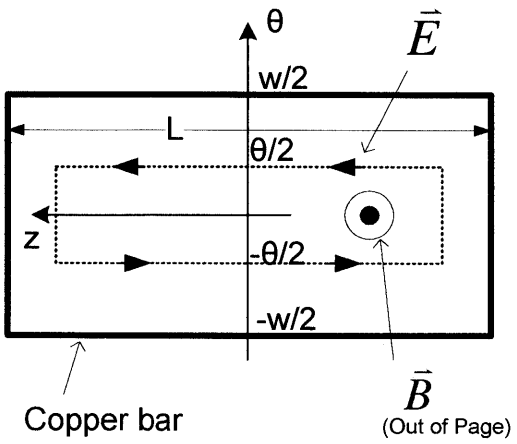

Figure 4-12: *Faraday's law is used to calculate the electric field around a closed loop through which a time varying magnetic field passes.*

thus

$$\int -\frac{\partial \tilde{\mathbf{B}}}{\partial t} \cdot d\tilde{\mathbf{s}} = L \int_{x=-\theta/2}^{\theta/2} -\frac{\partial B_r}{\partial t}\, dx \tag{4.23}$$

Figure (4-13) is a plot of the magnetic field density evaluated at the the surface of the outer core. However, only the time varying component contributes to the electric field. Thus, the magnetic field density through the copper bar is approximately,

$$B_r = B_0 \cos\left(\frac{\phi_0 \sin(\omega t)}{p} - x\right) \tag{4.24}$$

where, B_0 is amplitude of the spacial field density, ϕ_0 is the vibration amplitude, ω is the frequency of vibration, and p is the number of pole pairs. Differentiating with respect to time yields,

$$\frac{\partial B_r}{\partial t} = \frac{\phi_0 B_0 \omega}{p} \cos(\omega t) \sin\left(x - \frac{\phi_0 \sin(\omega t)}{p}\right) \tag{4.25}$$

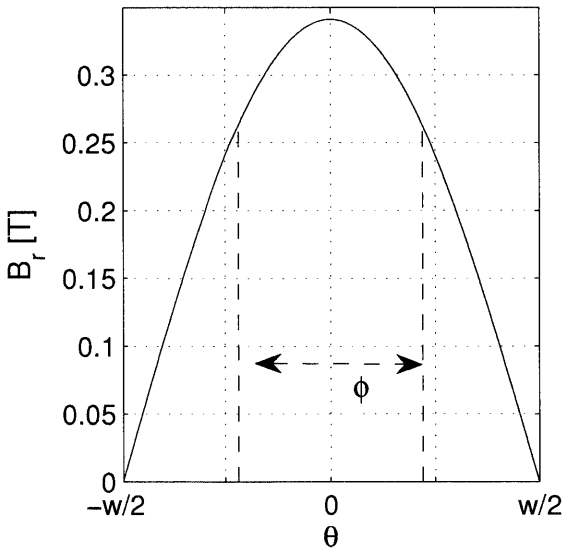

Figure 4-13: *Magnetic field evaluated at the core back iron across one magnetic pole pair. The red indicates the worst possible expected oscillation of value of magnetic field through a bar.*

Integrating this,

$$\begin{aligned} L \int_{x=-\theta/2}^{\theta/2} -\frac{\partial B_r}{\partial t}\, dx &= L \int_{x=-\theta/2}^{\theta/2} \frac{\phi_0 B_0 \omega}{p} \cos(\omega t) \sin\left(x - \frac{\phi_0 \sin(\omega t)}{p}\right) dx \\ &= \frac{L B_0 \phi_0 \omega}{p} \cos(\omega t) \left[\cos\left(\frac{1}{2p}\left(2\phi_0 \sin(\omega t) + \theta p\right)\right) - \cos\left(\frac{1}{2p}\left(2\phi_0 \sin(\omega t) - \theta p\right)\right)\right] \\ &= \frac{2 L B_0 \phi_0 \omega}{p} \sin\left(\frac{\theta}{2}\right) \cos(\omega t) \sin\left(\frac{\phi_0 \sin(\omega t)}{p}\right) \end{aligned} \tag{4.26}$$

Combining Eqs. (4.21), (4.22), and (4.26),

$$\begin{aligned} 2EL &= \frac{2 L B_0 \phi_0 \omega}{p} \sin\left(\frac{\theta}{2}\right) \cos(\omega t) \sin\left(\frac{\phi_0 \sin(\omega t)}{p}\right) \\ E &= \frac{B_0 \phi_0 \omega}{p} \sin\left(\frac{\theta}{2}\right) \cos(\omega t) \sin\left(\frac{\phi_0 \sin(\omega t)}{p}\right) \end{aligned} \tag{4.27}$$

The loss density is then the product of the current density and electric field, $P_{eddy} = J \cdot E$. Assuming the common constitutive relationship for copper ($J = \sigma E$)

the power lost can be written as,

$$\begin{aligned} P_{eddy} &= \sigma E^2 \\ &= \sigma \frac{B_0^2 \phi_0^2 \omega^2}{p^2} \sin^2\left(\frac{\theta}{2}\right) \cos^2(\omega t) \sin^2\left(\frac{\phi_0 \sin(\omega t)}{p}\right) \end{aligned} \tag{4.28}$$

Averaging this over one time cycle,

$$\begin{aligned} \bar{P}_{eddy} &= \frac{\omega}{2\pi} \int_{t=0}^{\frac{2\pi}{\omega}} \frac{\sigma B_0^2 \phi_0^2 \omega^2}{p^2} \sin^2\left(\frac{\theta}{2}\right) \cos^2(\omega t) \sin^2\left(\frac{\phi_0 \sin(\omega t)}{p}\right) dt \\ &= \frac{\sigma B_0^2 \phi_0^2 \omega^3}{2\pi p^2} \sin^2\left(\frac{\theta}{2}\right) \int_{t=0}^{\frac{2\pi}{\omega}} \cos^2(\omega t) \sin^2\left(\frac{\phi_0 \sin(\omega t)}{p}\right) dt \\ &\approx \frac{\sigma B_0^2 \phi_0^4 \omega^3}{800\pi p^2} \sin^2\left(\frac{\theta}{2}\right) \end{aligned} \tag{4.29}$$

Spatially averaging over the copper bar,

$$\begin{aligned} \left\langle \bar{P}_{eddy} \right\rangle &= \frac{2}{w} \int_{\theta=0}^{\frac{w}{2}} \frac{\sigma B_0^2 \phi_0^4 \omega^3}{800\pi p^2} \sin^2\left(\frac{\theta}{2}\right) d\theta \\ &= \frac{\sigma B_0^2 \phi_0^4 \omega^3}{1600\pi p^2} \end{aligned} \tag{4.30}$$

Now multiplying by the total number of bars,

$$\left\langle \bar{P}_{eddy} \right\rangle_{total} = \frac{\sigma B_0^2 \phi_0^4 \omega^3}{800\pi p} = 36\mu W \tag{4.31}$$

where the values used for the numerical calculation are found in tab. (4.3).

variable	value	unit
σ_{copper}	$6e10^7$	$S \cdot m^{-1}$
B_0	0.4	T
ϕ_0	0.7	rad
ω	20	Hz
p	8	

Table 4.3: Values of the constants in the current prototype

4.3.8 Coils

Winding a wire coil can be thought of as a material added process. The challenge of this approach is adding the material in the correct geometry. Conversely, if the coils are cut from stock material that already has the correct geometry, the assembly process is simplified and straightness and parallelism is ensured.

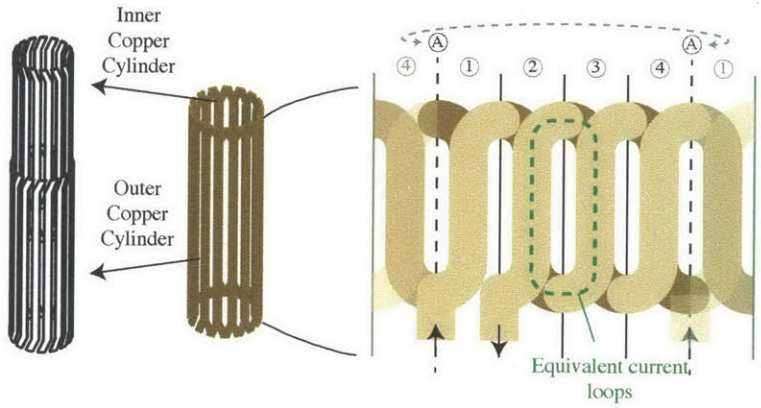

Figure 4-14: *Illustration of the surface wound coil design.*

Figure 4-14 is an illustration of the coil deign. The coil consists of an array of rectangular conductors in two layers. Both the outer and inner layers of conductors have a central straight section and oppositely directed angular portions at both ends. The central straight section is the active section of the coil, and the angular sections complete the end turns.

To manufacturing this type of geometry, the negative space in the design is cut out of a set of concentric copper cylinders that are the correct thickness and diameter of the final armature, but are longer than the finished length of the final armature (Fig. 4-15). Since the cylinders are longer than the finished length of the final coil, a ring of copper holds the individual conductors in their prospective positions maintaining location, straightness, and parallelism. In some extreme applications where the thickness of the copper cylinder or the width of the individual conductors is too small to self support, a sacrificial cylinder can be inserted inside the copper cylinders

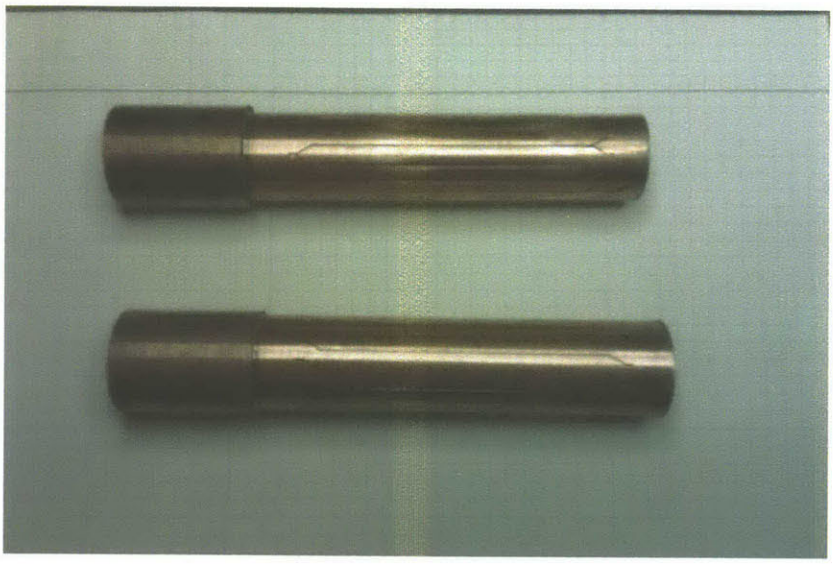

Figure 4-15: *Copper cylinders with geometry cut out of using Omax MicroWater Jet (Patent Pending).*

to provide structure.

The width of the cuts is very important to the performance of the coils. Wide kerfs remove a large amount of conductor material and reduce the compaction factor of the coil. Technically, the cuts could also be cut in a laser tube cutter, but due to the index of refraction of copper, laser cutting copper is very difficult. Unfortunately, the cuts cannot be cut straight through since the angular portions on opposite sides of the cylinder are in opposite directions. This makes using wire EDM difficult. However, it should be possible to develop a wire EDM with guide rollers in the center of the cylinder to allow for cutting only one wall of cylinder. This would also add addition difficulties related to rethreading the electrode wire in each slit. The slits shown in Fig. 4-15 are cut with a new patent pending micro water jet technology being developed by Omax. The micro water jet can self pierce (eliminating electrode threading) and cut on one side, and the new micro jet technology has an as cut kerf width of approximately 0.006". Rectangular voids are incorporated at both ends of the slits. These voids are primarily to simplify soldering, but also provide a good location for piercing.

Next, insulation must be applied to the cylinders to prevent electrical contact

Figure 4-16: *The top cylinders are oxidized in an attempt to create an insulaiton layer. However, the oxide layer was flaky and unreliable as an insulation. The bottom picture is a Paralyene coated cylinder.*

between the inner and outer layers of conductor. Just as in the radial direction, the larger the distance between layers of copper, the lower the compaction factor of the coil. Thus, an oxide layer was tried as the insulation layer between cylinders. However, the oxide layer was flaky and un reliable (Fig. 4-16). Ultimately a polymer insulator such as Paralyene or Kapton is better suited and can be applied to similar thicknesses as the oxide layer with vapor deposition processes. When the process is scaled up to larger scale manufacturing, more refinement could be used in this area. Oxidizing in oxygen rich environments, or dip/spay-on coatings might be more cost effective than vapor deposition of Paralyene. Special attention should be taken to de-burr the outer surface of the inner cylinder and the inner surface of the outer cylinder before the insulation is applied. A burr on either or these surfaces could scratch the insulation leading to unwanted electrical contact between the layers. The outer cylinder requires additional attention since the water jetting process typically leaves flashing on the inner surface. In the current prototype, a flexible hone is used to de-burr the inner surface of the outer cylinder (Fig. 4-17). Emery cloth is used to de-burr the inner cylinder.

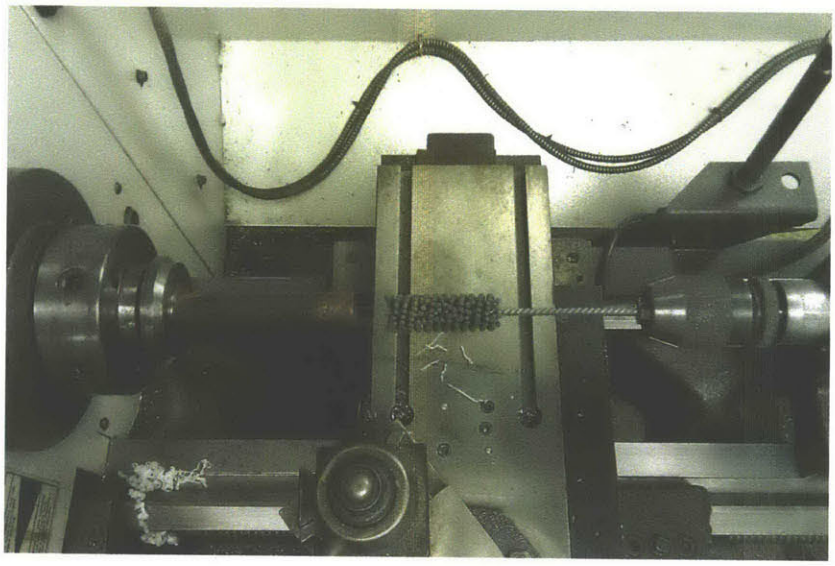

Figure 4-17: *Flexible hone used to de-burr the interior surface or the outer cylinder*

Figure 4-18: *Ideally, the insulated inner cylinder can be inserted into the insulated outer cylinder. However, if necessary the outer cylinder can be split along one of the slits to create more clearance.*

Once the insulation has been applied, the cylinders can be assembled. In the simplest arraignment, inner cylinder is inserted inside the outer cylinder. However, if necessary, the outer cylinder can be split to provide additional clearance (Fig. 4-18). The assembled cylinders are placed in a mold and potted in epoxy to fix the cylinders together and provide additional structure for the completed armature (Fig. 4-19).

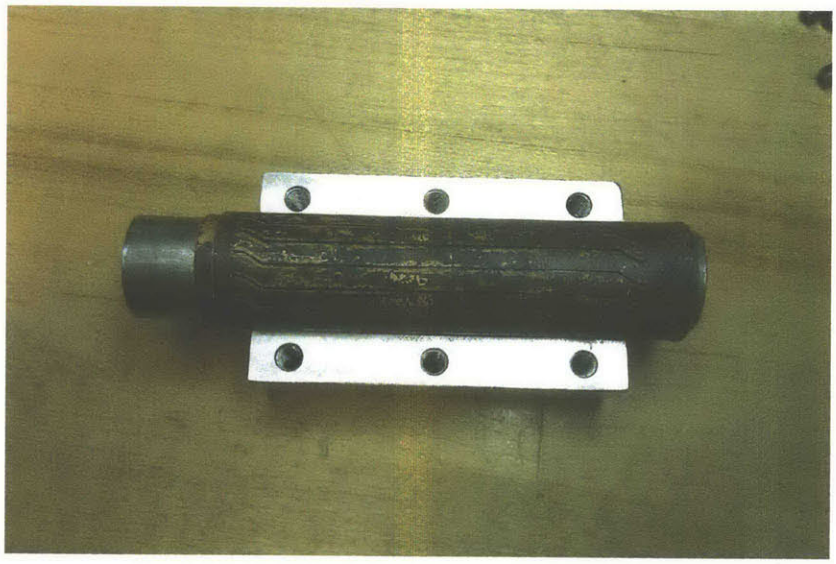

Figure 4-19: *Assembled cylinders are placed in a mold and potted in epoxy to affix the cylinders and provide additional structure.*

Now that the coils are potted in epoxy, the support rings created by the extra long cylinders can be cut off (Fig. 4-20), and the ends can be dip soldered to create the end turn connections (Fig. 4-21). Finally, the connecting wires can be soldered

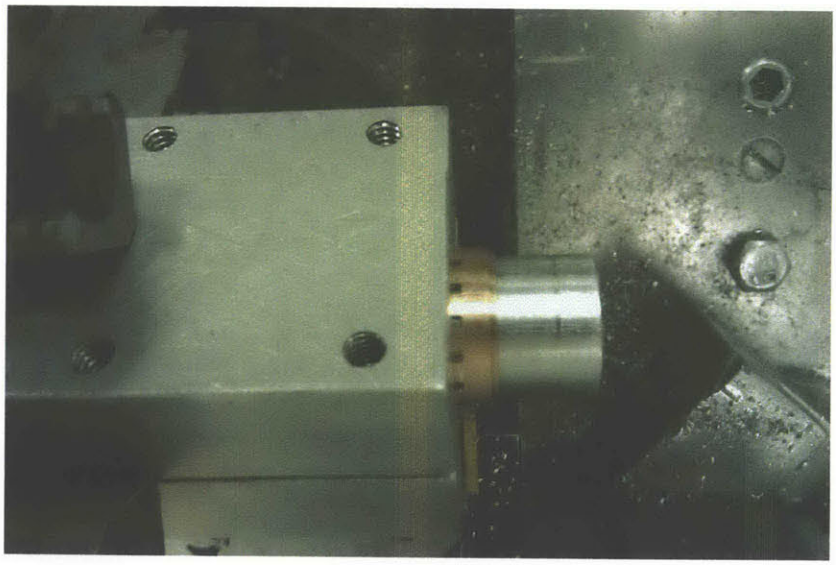

Figure 4-20: *The support rings created by the extra long cylinders being cut off.*

into place completing the coil (Fig. 4-22).

The prototype coil shown in Figs. 4-14-4-22 is 1" in diameter, 4 turns, single phase,

Figure 4-21: *The end turns are created by dip soldering.*

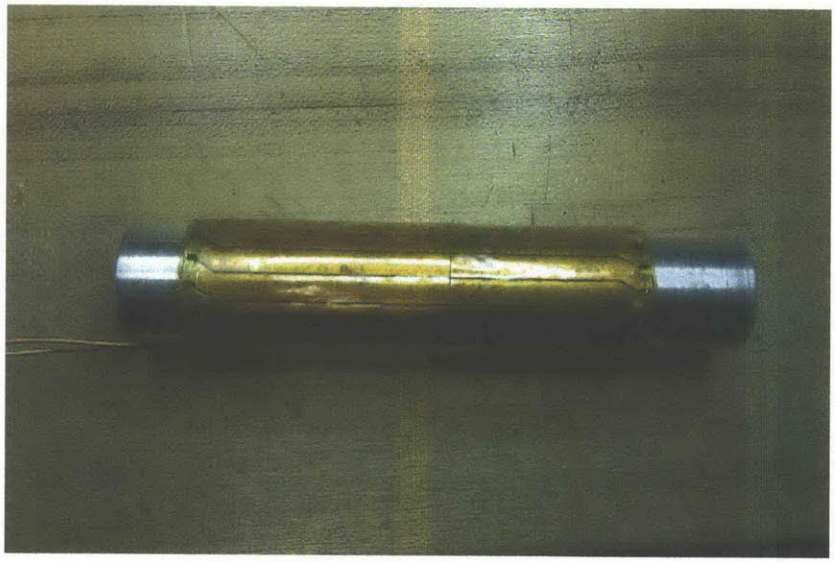

Figure 4-22: *Completed Coil*

and 8 poles with a measured resistance of 0.5 Ω.

Appendix A

Matlab Codes

A.0.9 Calculation of EMF

```
% [R] = rtechetch(in) function used to calculate the restance of a
% tech-etch coil
%
%INPUTS
%   in() -  a vector containing the appropriate inputs
%       in(1) - [m], roc radial distance to the outer core
%       in(2) - [m], tcop thickness of the copper
%       in(3) - [] , nl number of layers
%       in(4) - [] , nt number of traces per layer
%       in(5) - [m], kl thickness between layers
%       in(6) - [m], kt thickness between traces
%       in(7) - [m], h active axial coil length
%       in(8) - [m], z maximum coil length
%       in(9) - [ohm-m] , resistivity
%       in(10)- [] , s number of coil pairs
%OUTPUTS
%   R - [ohm], total coil resistance
%
```

```
%A Zachary Trimble
%8.17.2009

function [R] = rtechetch(in)

%distribute input vector
roc  = in(1);
tcop = in(2);
nl   = in(3);
nt   = in(4);
kl   = in(5);
kt   = in(6);
h    = in(7);
z    = in(8);
rho  = in(9);
s    = in(10);

r = roc-1*nl/1*(tcop+3/2*kl);
tcoil = r*pi/nt/s;
disp('Total coil thickness');
disp(tcoil/0.0254);
Aactive = tcoil*tcop;
lactive = 2*nl*nt*s*h;

Ractive = lactive*rho/Aactive;

theta = atan(2*s*(z-h)/r/pi);
Aet   = sin(theta)*Aactive;
let   = 4*nl*nt*s*sqrt(((z-h)/2)^2+(r*pi/4/s)^2);
```

```
Ret  = let*rho/Aet;

R = Ractive+Ret;
```

A.0.10 Calculation of EMF

```
% emf = inducedV(phi,dphi,in), calculates the induced voltage
%
%INPUTS
%   phi - [rad], vector of the angular displacement
%   dphi - [rad/s], vector of the angular velocity
%   in - vector containing the relevant inputs to the system
%       in(1) - [m], ric radius to the outer surface of the inner core
%       in(2) - [m], rm radius to the outer surface of the magnets
%       in(3) - [m], roc radius to the inner surface of the outer core
%       in(4) - [T], BR residual flux density
%       in(5) - [] , p number of magnetic pole pairs
%       in(6) - [m], N number of coil turns
%       in(7) - [h], h axial dimension
%       in(8) - [m], r radial coordinate the current is located at
%       in(9) - [] , a phase number
%       in(10)- [] , A total number of phases
%OUTPUTS
%   emf - [V], induced voltage
%
%A Zachary Trimble
%8.10.2009

function emf = inducedV(phi,dphi,in);
```

```
%Initialize the emf vector
emf = zeros(size(phi));

%Extract the inputs from the in variable
ric = in(1);
rm  = in(2);
roc = in(3);
BR  = in(4);
p   = in(5);
N   = in(6);
h   = in(7);
r   = in(8);
a   = in(9);
A   = in(10);

%Define a minimum relative rms error between summation terms and a maximum
%number of interations to all
errmin  = 1e-6;
imax    = 100;

%Calculate the B vector for increasing summation terms until either the
%maximum iterations limit or the minimum relative error limit is reached.
i = 0;
err = 1;

while i<imax && err>errmin;
    i = i+1;
    emf0 = emf;
    nk = p*(2*i-1);
    lambda0 = 8*N*h*BR*rm*...
```

```
                ((rm/ric)^nk-(ric/rm)^nk)*...
                ((r/roc)*nk+(roc/r)^nk)/...
                (pi^2*(2*i-1)^3*((ric/roc)^nk-(roc/ric)^nk));
    emf = emf + lambda0*nk*cos(nk*phi+2*pi*(a-1)/A).*dphi;
    err = sqrt(mean((emf-emf0).^2));
end
```

A.0.11 Calculation of Induced Voltage for Constant Angular Velocity Input

```
%The following script file use the inducedV.m function to calculate the
%induced voltage for continuous constant rotation

%%%%%%%%%%%%%%%%%%%%%%%%%
%%% PREPARE WORKSPACE %%%
%%%%%%%%%%%%%%%%%%%%%%%%%
clear all
close all
clc

%%%%%%%%%%%%%
%%% INPUTS %%%
%%%%%%%%%%%%%
%general dimensions
roc = 13.3;                     %[mm], radius to outer core
rm  = 11.2;                     %[mm], radius to outer magnet face
ric = 8.00;                     %[mm], radius to inner core
h   = 3*25.4;                   %[mm], axial dimension of device

%magnetic parameters
```

```
p   = 8;                          %[], number of magnetic pole pairs
BR  = 1.29;                       %[T], Residual Flux density
N   = 32;                         %[], number of turns in the coil
a   = 1;                          %[], phase number
A   = 1;                          %[], total number of phases

%create input vector
in(10)= A;
in(9) = a;
in(8) = roc/1000;
in(7) = h/1000;
in(6) = N;
in(5) = p;
in(4) = BR;
in(3) = roc/1000;
in(2) = rm/1000;
in(1) = ric/1000;

%similation vectors
wrpm = [30 290];                      %[rpm], constant revolution speed
w = wrpm*2*pi/60;
t = linspace(0,2*pi/w(1),1000);    %[s], time vector
phi(2,:)  = w(2)*t;
phi(1,:)  = w(1)*t;
dphi(2,:) = ones(1,length(t))*w(2);
dphi(1,:) = ones(1,length(t))*w(1);

%%%%%%%%%%%%%%%%%%%
%%% CALCULATIONS %%%
%%%%%%%%%%%%%%%%%%%
```

```
emf1 = inducedV(phi(1,:),dphi(1,:),in);
emf2 = inducedV(phi(2,:),dphi(2,:),in);

%%%%%%%%%%%%%%%%%%%%
%%% PLOT RESULTS %%%
%%%%%%%%%%%%%%%%%%%%
figure(1); clf;
set(gcf,'units','normalized',...
        'position',[0.25,0.25,0.5,0.5]);
plot(t,emf1,t,emf2);
grid on;
set(gca,'fontsize',18);
title(texlabel(sprintf('Estimated induced voltage\n(phi = omega t)')),...
      'fontsize',30);
xlabel('Time [s]','fontsize',26);
ylabel('Voltage [V]','fontsize',26);
xlim([0,2*pi/w(1)]);
%ylim(0.3*[-1,1]);
legend(texlabel(sprintf('omega = %2.0f RPM',wrpm(1))),...
       texlabel(sprintf('omega = %2.0f RPM',wrpm(2))));
```

A.0.12 Calculation of Induced Voltage for Oscillating Angular Input

```
%The following script file use the inducedV.m function to calculate the
%induced voltage for an oscilating input phi = phi0*sin(w*t)

%%%%%%%%%%%%%%%%%%%%%%%%%%
%%% PREPARE WORKSPACE %%%
%%%%%%%%%%%%%%%%%%%%%%%%%%
```

```
clear all
close all
clc

%%%%%%%%%%%%%
%%% INPUTS %%%
%%%%%%%%%%%%%
%general dimensions
roc = 13.3;                    %[mm], radius to outer core
rm  = 11.2;                    %[mm], radius to outer magnet face
ric = 8.00;                    %[mm], radius to inner core
h   = 3*25.4;                  %[mm], axial dimension of device

%magnetic parameters
p   = 8;                       %[], number of magnetic pole pairs
BR  = 1.29;                    %[T], Residual Flux density
N   = 32;                      %[], number of turns in the coil
a   = 1;                       %[], phase number
A   = 1;                       %[], total number of phases

%create input vector
in(10)= A;
in(9) = a;
in(8) = roc/1000;
in(7) = h/1000;
in(6) = N;
in(5) = p;
in(4) = BR;
in(3) = roc/1000;
in(2) = rm/1000;
```

```
in(1) = ric/1000;

%similation vectors
whz  = 30;                      %[Hz], oscilation frequency
w    = 2*pi*30;
phi0 = [5 10 15];               %[deg], oscilation amplitude
C    = pi/2/p;
t    = linspace(0,4*pi/w,1000);
%%%%%%%%%%%%%%%%%%%
%%% CALCULATIONS %%%
%%%%%%%%%%%%%%%%%%%
emf = zeros(3,1000);
for i = 1:3
    phi  = phi0(i)*pi/180*sin(w*t);
    dphi = phi0(i)*pi/180*w*cos(w*t);
    emf(i,:) = inducedV(phi,dphi,in);
end

emfc = zeros(3,1000);
for i = 1:3
    phi  = phi0(i)*pi/180*sin(w*t)+C;
    dphi = phi0(i)*pi/180*w*cos(w*t);
    emfc(i,:) = inducedV(phi,dphi,in);
end

%%%%%%%%%%%%%%%%%%%
%%% PLOT RESULTS %%%
%%%%%%%%%%%%%%%%%%%
figure(1); clf;
set(gcf,'units','normalized',...
```

```
        'position',[0.05,0.25,0.9,0.5]);

subplot(1,2,1);
plot(t,emf);
grid on;
set(gca,'fontsize',18);
title(texlabel(sprintf('Estimated induced voltage\n(phi = phi_A sin(omega t))')),...
      'fontsize',30);
xlabel('Time [s]','fontsize',26);
ylabel('Voltage [V]','fontsize',26);
xlim([0,4*pi/w]);
%ylim(0.3*[-1,1]);
legend(texlabel(sprintf('phi_A = %2.0f deg',phi0(1))),...
       texlabel(sprintf('phi_A = %2.0f deg',phi0(2))),...
       texlabel(sprintf('phi_A = %2.0f deg',phi0(3))));

subplot(1,2,2);
plot(t,emfc);
grid on;
set(gca,'fontsize',18);
title(texlabel(sprintf('Estimated induced voltage\n(phi = phi_A sin(omega t)+pi/2s)')
      'fontsize',30);
xlabel('Time [s]','fontsize',26);
ylabel('Voltage [V]','fontsize',26);
xlim([0,4*pi/w]);
%ylim(0.3*[-1,1]);
legend(texlabel(sprintf('phi_A = %2.0f deg',phi0(1))),...
       texlabel(sprintf('phi_A = %2.0f deg',phi0(2))),...
       texlabel(sprintf('phi_A = %2.0f deg',phi0(3))));
```

A.0.13 Symbolic Solution of Potential Constants

```
%This is a symbolic math script function used to solve for the scalar
%potential constants associated with the magnetic field.

%PREPARE WORKSPACE
clear all
clc

%INITIALIZE SYMOLIC SYMBOLS
syms n roc ric rm M0 k real

%CREATE MATRICIES AND VECTORS
A = [roc^n  0      roc^(-n)  0        0      0      0        0;...
     0      roc^n  0         roc^(-n) 0      0      0        0;...
     0      0      0         0        ric^n  0      ric^(-n) 0;...
     0      0      0         0        0      ric^n  0        ric^(-n);...
     rm^n   0      rm^(-n)   0       -rm^n   0     -rm^(-n)  0;...
     0      rm^n   0         rm^(-n)  0     -rm^n   0       -rm^(-n);...
     rm^n   0     -rm^(-n)   0       -rm^n   0      rm^(-n)  0;...
     0      rm^n   0        -rm^(-n)  0     -rm^n   0        rm^(-n)];

B = [0;...
     0;...
     0;...
     0;...
     0;...
     0;...
     -4*M0*rm/(pi*n*(2*k-1));...
     0];
```

```
%SOLVE THE EQUATIONS
x = inv(A)*B;

%DISPLAY THE RESULTS
pretty(x)
```

A.0.14 Numerical visualization of the convergence of the infinite series solutions

```
%The following script file is used to numerically visualize the number of
%terms required in the infinite series solutions of the B field

clear all
close all
clc


%INPUTS
BR  = 1.29;                          %[T = kg/A-s^2], residual flux density
rm  = 11.2e-3;                       %[m], radius to outer magnet face
roc = 13.3e-3;                       %[m], radius to outer core
ric = 8.00e-3;                       %[m], radius to inner core
phi = 0;                             %[rad], relative rotation of rotor
p   = 8;                             %[], number of pole pairs

%SIMULATION VARIABLES
theta = linspace(0,2*pi,1000);        %[rad], angular coordinate
Br    = zeros(10,length(theta));     %[T], radial flux density
```

```
%CALCULATIONS
beta  = theta-phi;                    %[rad], relative angular coordinate

Br(1,:) = ((rm/ric)^p-(ric/rm)^p)/((ric/roc)^p-(roc/ric)^p)*sin(p*beta);
for k = 2:10
    nk = p*(2*k-1);
    Br(k,:) = Br(k-1,:)+((rm/ric)^nk-...
    (ric/rm)^nk)/((ric/roc)^nk-...
    (roc/ric)^nk)/(2*k-1)*sin(nk*beta);
    Brerr(k-1) = sqrt(mean(((Br(k,:)-Br(k-1,:))).^2));
end
Br = -4*BR*rm/pi/roc*Br;

%DISPLAY RESULTS
fsize = [14,16,20];

figure(1);clf;
set(gcf,'units','normalized',...
        'position',[0.05,0.45,0.9,0.45]);
subplot(1,2,1);
plot(theta,Br);
grid on;
set(gca,'fontsize',fsize(1));
title(texlabel('Radial flux density'),'fontsize',fsize(3));
xlabel(texlabel('theta'),'fontsize',fsize(2));
ylabel(texlabel('B_r'),'fontsize',fsize(2));
legend('k=1','k=2','k=3','k=4','k=5','k=6','k=7','k=8','k=9','k=10');

subplot(1,2,2);
```

```
plot(2:10,Brerr);
set(gca,'fontsize',fsize(1));
grid on;
title(texlabel('Relatve RMS error'),'fontsize',fsize(3));
xlabel(texlabel('Summation term (k)'),'fontsize',fsize(2));
ylabel(texlabel('RMS[B_{r_k}-B_{r_{k-1}}]'),'fontsize',fsize(2));
```

A.0.15 Calculation and visualization of the vector flux density ($\tilde{B}$)

```
clear all
close all
clc


%INPUTS
BR  = 1.29;                          %[T = kg/A-s^2], residual flux density
rm  = 11.2e-3;                       %[m], radius to outer magnet face
roc = 13.3e-3;                       %[m], radius to outer core
ric = 8.00e-3;                       %[m], radius to inner core
phi = 0;                             %[rad], relative rotation of rotor
p   = 4;                             %[], number of pole pairs

%SIMULATION VARIABLES
theta = linspace(0,2*pi,100);         %[rad], angular coordinate
rmag  = linspace(ric,rm,5);          %[m], radial coordinate in the magnet
rair  = linspace(rm,roc,10);          %[m], radial coordinate in the air gap

[Rmag,Thetamag] = meshgrid(rmag,theta);
```

```
Betamag = Thetamag-phi;
[Rair,Thetaair] = meshgrid(rair,theta);
Betaair = Thetaair-phi;
[m,n] = size(Rmag);
Bmag = zeros(m,n,2);          %[T], radial flux density in magnet
[m,n,] = size(Rair);
Bair = zeros(m,n,2);          %[T], radial flux density in air gap

%CALCULATIONS

for k = 1:4
    nk = p*(2*k-1);
    Bmag(:,:,1) = Bmag(:,:,1) + ...
        1/(2*k-1)*((((rm/roc)^nk-(roc/rm)^nk)*...
        ((Rmag/ric).^nk+(ric./Rmag).^nk))/...
        ((ric/roc)^nk-(roc/ric)^nk)-2).*sin(nk*Betamag);
    Bmag(:,:,2) = Bmag(:,:,2) + ...
        1/(2*k-1)*((((rm/roc)^nk-(roc/rm)^nk)*...
        ((Rmag/ric).^nk-(ric./Rmag).^nk))/...
        ((ric/roc)^nk-(roc/ric)^nk)).*cos(nk*Betamag);
    Bair(:,:,1) = Bair(:,:,1) + ...
        1/(2*k-1)*((((rm/ric)^nk-(ric/rm)^nk)*...
        ((Rair/roc).^nk+(roc./Rair).^nk))/...
        ((ric/roc)^nk-(roc/ric)^nk)).*sin(nk*Betaair);
    Bair(:,:,2) = Bair(:,:,2) + ...
        1/(2*k-1)*((((rm/ric)^nk-(ric/rm)^nk)*...
        ((Rair/roc).^nk-(roc./Rair).^nk))/...
        ((ric/roc)^nk-(roc/ric)^nk)).*cos(nk*Betaair);
end
Bmag(:,:,1) = -2*BR*rm/pi./Rmag.*Bmag(:,:,1);
```

```
Bmag(:,:,2) = -2*BR*rm/pi./Rmag.*Bmag(:,:,2);
Bair(:,:,1) = -2*BR*rm/pi./Rair.*Bair(:,:,1);
Bair(:,:,2) = -2*BR*rm/pi./Rair.*Bair(:,:,2);

%DISPLAY RESULTS
%create reference circles for the visual simplicity
psi = linspace(0,2*pi,1000);
xcircic = ric*cos(psi)*1000;
ycircic = ric*sin(psi)*1000;
xcircm  = rm*cos(psi)*1000;
ycircm  = rm*sin(psi)*1000;
xcircoc = roc*cos(psi)*1000;
ycircoc = roc*sin(psi)*1000;

%plot the reference circles
fsize = [14,16,20];

figure(1);clf;
 set(gcf,'units','normalized',...
         'position',[0.01,0.35,0.98,0.55]);

subplot(1,2,1)
plot(xcircic,ycircic,'k',...
     xcircm,ycircm,'k',...
     xcircoc,ycircoc,'k','linewidth',5);
grid on;
axis equal;
set(gca,'fontsize',fsize(1));
title(texlabel('Vector plot of the flux density'),'fontsize',fsize(3));
xlabel(texlabel('mm'),'fontsize',fsize(2));
```

```
ylabel(texlabel('mm'),'fontsize',fsize(2));
hold on;
for i = 1:2*p
    plot([ric rm]*1000*cos(i*pi/p),[ric rm]*1000*sin(i*pi/p),...
        'k','linewidth',4);
end

%change the flux density calculation to cartesian coordinates for plotting
Xmag = Rmag.*cos(Thetamag)*1000;
Ymag = Rmag.*sin(Thetamag)*1000;
Umag = Bmag(:,:,1).*cos(Thetamag)-Bmag(:,:,2).*sin(Thetamag);
Vmag = Bmag(:,:,1).*sin(Thetamag)+Bmag(:,:,2).*cos(Thetamag);
Xair = Rair.*cos(Thetaair)*1000;
Yair = Rair.*sin(Thetaair)*1000;
Uair = Bair(:,:,1).*cos(Thetaair)-Bair(:,:,2).*sin(Thetaair);
Vair = Bair(:,:,1).*sin(Thetaair)+Bair(:,:,2).*cos(Thetaair);

%vector plot
quiver(Xmag,Ymag,Umag,Vmag,'b');
quiver(Xair,Yair,Uair,Vair,'b');
%plot zoom circle
plot(5*cos(psi)+10,5*sin(psi),'--r','linewidth',3);

%ZOOMED IN PLOT
%recalculate for zoomed in area
theta = linspace(-pi/p,pi/p,25);        %[rad], angular coordinate
rmag  = linspace(ric,rm,7);         %[m], radial coordinate in the magnet
rair  = linspace(rm,roc,5);         %[m], radial coordinate in the air gap

[Rmag,Thetamag] = meshgrid(rmag,theta);
```

```
Betamag = Thetamag-phi;
[Rair,Thetaair] = meshgrid(rair,theta);
Betaair = Thetaair-phi;
[m,n] = size(Rmag);
Bmag = zeros(m,n,2);          %[T], radial flux density in magnet
[m,n,] = size(Rair);
Bair = zeros(m,n,2);          %[T], radial flux density in air gap

for k = 1:10
    nk = p*(2*k-1);
    Bmag(:,:,1) = Bmag(:,:,1) + ...
        1/(2*k-1)*((((rm/roc)^nk-(roc/rm)^nk)*...
        ((Rmag/ric).^nk+(ric./Rmag).^nk))/...
        ((ric/roc)^nk-(roc/ric)^nk)-2).*sin(nk*Betamag);
    Bmag(:,:,2) = Bmag(:,:,2) + ...
        1/(2*k-1)*((((rm/roc)^nk-(roc/rm)^nk)*...
        ((Rmag/ric).^nk-(ric./Rmag).^nk))/...
        ((ric/roc)^nk-(roc/ric)^nk)).*cos(nk*Betamag);
    Bair(:,:,1) = Bair(:,:,1) + ...
        1/(2*k-1)*((((rm/ric)^nk-(ric/rm)^nk)*...
        ((Rair/roc).^nk+(roc./Rair).^nk))/...
        ((ric/roc)^nk-(roc/ric)^nk)).*sin(nk*Betaair);
    Bair(:,:,2) = Bair(:,:,2) + ...
        1/(2*k-1)*((((rm/ric)^nk-(ric/rm)^nk)*...
        ((Rair/roc).^nk-(roc./Rair).^nk))/...
        ((ric/roc)^nk-(roc/ric)^nk)).*cos(nk*Betaair);
end
Bmag(:,:,1) = -2*BR*rm/pi./Rmag.*Bmag(:,:,1);
Bmag(:,:,2) = -2*BR*rm/pi./Rmag.*Bmag(:,:,2);
Bair(:,:,1) = -2*BR*rm/pi./Rair.*Bair(:,:,1);
```

```
Bair(:,:,2) = -2*BR*rm/pi./Rair.*Bair(:,:,2);

%create reference circles for the visual simplicity
psi = linspace(-1.5*pi/p,1.5*pi/p,1000);
xcircic = ric*cos(psi)*1000;
ycircic = ric*sin(psi)*1000;
xcircm  = rm*cos(psi)*1000;
ycircm  = rm*sin(psi)*1000;
xcircoc = roc*cos(psi)*1000;
ycircoc = roc*sin(psi)*1000;

subplot(1,2,2);
plot(xcircic,ycircic,'k',...
     xcircm,ycircm,'k',...
     xcircoc,ycircoc,'k','linewidth',5);
grid on;
axis equal;
set(gca,'fontsize',fsize(1));
title(sprintf(...
    'Zoomed in vector plot of flux\ndensity for 1 magnet pair'),...
                    'fontsize',fsize(3));
xlabel(texlabel('mm'),'fontsize',fsize(2));
ylabel(texlabel('mm'),'fontsize',fsize(2));
hold on;
for i = 1:3
    plot([ric rm]*cos((i-2)*pi/p)*1000,[ric rm]*sin((i-2)*pi/p)*1000,...
        'k','linewidth',4);
end

%change the flux density calculation to cartesian coordinates for plotting
```

```
Xmag = Rmag.*cos(Thetamag)*1000;
Ymag = Rmag.*sin(Thetamag)*1000;
Umag = Bmag(:,:,1).*cos(Thetamag)-Bmag(:,:,2).*sin(Thetamag);
Vmag = Bmag(:,:,1).*sin(Thetamag)+Bmag(:,:,2).*cos(Thetamag);
Xair = Rair.*cos(Thetaair)*1000;
Yair = Rair.*sin(Thetaair)*1000;
Uair = Bair(:,:,1).*cos(Thetaair)-Bair(:,:,2).*sin(Thetaair);
Vair = Bair(:,:,1).*sin(Thetaair)+Bair(:,:,2).*cos(Thetaair);

%vector plot
quiver(Xmag,Ymag,Umag,Vmag,'b');
quiver(Xair,Yair,Uair,Vair,3,'b');
```

A.1 Matlab Data Reader Script

The following is a Matlab script that is used to read the provided data from the Excel spreadsheets into the Matlab environment, and plot the raw data.

```
clear all
clc
%INPUT -- set plots to 1 to plot and any other number to not
plots = 0;

%Read-in, separate, and collate the data from the provided spreadsheets
data = xlsread('Timer 822_time domain.xls','a6:d2053');
time(:,1)   = data(:,1);
yellow(:,1) = data(:,4);
green(:,1)  = data(:,3);
red(:,1)    = data(:,2);

data = xlsread('Timer 823_time domain.xls','a6:d2053');
```

```
time(:,2)   = data(:,1);
yellow(:,2) = data(:,4);
green(:,2)  = data(:,3);
red(:,2)    = data(:,2);

data = xlsread('Timer 824_time domain.xls','a6:d2053');
time(:,3)   = data(:,1);
yellow(:,3) = data(:,4);
green(:,3)  = data(:,3);
red(:,3)    = data(:,2);

data = xlsread('Timer 825_time domain.xls','a6:d2053');
time(:,4)   = data(:,1);
yellow(:,4) = data(:,4);
green(:,4)  = data(:,3);
red(:,4)    = data(:,2);

data = xlsread('Timer 826_time domain.xls','a6:d2053');
time(:,5)   = data(:,1);
yellow(:,5) = data(:,4);
green(:,5)  = data(:,3);
red(:,5)    = data(:,2);

if plots == 1
%Plot and save the data for visual reference

xmin = 0;
xmax = 2.05;
ymin = -5;
ymax = 5;
```

```
figure(1); clf;
plot(time,yellow); xlim([xmin,xmax]); ylim([ymin,ymax]);
set(gca,'fontsize',20);
title('Yellow','fontsize',30);
xlabel('Time [s]','fontsize',24);
ylabel('Acceleration [G]','fontsize',24);
saveas(gcf,'C:\Documentsand Settings\Zac\My Documents\Research\Shakeandspin...
              \WDPRepeater\Presentations\yellowTime.eps');
saveas(gcf,'C:\Documents and Settings\Zac\My Documents\Research\Shakeandspin...
              \WDPRepeater\Presentations\yellowTime.emf');

figure(2); clf;
plot(time,green); xlim([xmin,xmax]); ylim([ymin,ymax]);
set(gca,'fontsize',20);
title('Green','fontsize',30);
xlabel('Time [s]','fontsize',24);
ylabel('Acceleration [G]','fontsize',24);
saveas(gcf,'C:\Documents and Settings\Zac\My Documents\Research\Shakeandspin...
              \WDPRepeater\Presentations\greenTime.eps');
saveas(gcf,'C:\Documents and Settings\Zac\My Documents\Research\Shakeandspin...
              \WDPRepeater\Presentations\greenTime.emf');

figure(3); clf;
plot(time,red); xlim([xmin,xmax]); ylim([ymin,ymax]);
set(gca,'fontsize',20);
title('Red','fontsize',30);
xlabel('Time [s]','fontsize',24);
ylabel('Acceleration [G]','fontsize',24);
saveas(gcf,'C:\Documents and Settings\Zac\My Documents\Research\Shakeandspin...
```

```
            \WDPRepeater\Presentations\redTime.eps');
saveas(gcf,'C:\Documents and Settings\Zac\My Documents\Research\Shakeandspin...
            \WDPRepeater\Presentations\redTime.emf');

figure(4); clf;
subplot(1,3,1);
plot(time,red); xlim([xmin,xmax]); ylim([ymin,ymax]);
set(gca,'fontsize',20);
title('Red','fontsize',30);
xlabel('Time [s]','fontsize',24);
ylabel('Acceleration [G]','fontsize',24);

subplot(1,3,2);
plot(time,green); xlim([xmin,xmax]); ylim([ymin,ymax]);
set(gca,'fontsize',20);
title('Green','fontsize',30);
xlabel('Time [s]','fontsize',24);
ylabel('Acceleration [G]','fontsize',24);

subplot(1,3,3);
plot(time,yellow); xlim([xmin,xmax]); ylim([ymin,ymax]);
set(gca,'fontsize',20);
title('Yellow','fontsize',30);
xlabel('Time [s]','fontsize',24);
ylabel('Acceleration [G]','fontsize',24);

saveas(gcf,'C:\Documents and Settings\Zac\My Documents\Research\Shakeandspin...
            \WDPRepeater\Presentations\rawAccelerationData.eps');
saveas(gcf,'C:\Documents and Settings\Zac\My Documents\Research\Shakeandspin...
            \WDPRepeater\Presentations\rawAccelerationData.emf');
```

```
end
```

A.2 Matlab Rotation Script

The following is a Matlab script that is used to rotate the previously read data from the *(green,yellow,red)* coordinate system to the (r, θ, z) coordinate system.

```
%This script file rotates data provided by reader.m through a given
%angle theta to align the data with a more typical cylindrical coordinate
%system

%INPUT -- The script reader.m must be run first

%INPUT -- input the rotation angle
theta = -22*pi/180;

%INPUT -- set plots to 1 to plot and any other number to not
plots = 1;

%rotate the data to a more appropriate (r,theta) coordinate system
r = yellow*cos(theta)+green*sin(theta);
t = -yellow*sin(theta)+green*cos(theta);
z = red;

%Creates a continuous string of time data by colocating the 5 individual
%streams of data. The data is colocated visually by inspecting the begin
%and ending of each string and throwing away the first and/or last few
%points to eliminate jumps. This way the data appears smooth.
ts = zeros(10196,1);
ts(1:2040)     = ts(1:2040)+t(2:2041,1);
ts(2041:4079)  = ts(2041:4079)+t(6:2044,2);
ts(4080:6117)  = ts(4080:6117)+t(8:2045,3);
ts(6118:8157)  = ts(6118:8157)+t(2:2041,4);
```

```
ts(8158:10196) = ts(8158:10196)+t(9:2047,5);
times = ((1:10196)-1)*0.001;

if plots == 1
%Plot and save the data for visual reference

xmin = 0;
xmax = 2.05;
ymin = -5;
ymax = 5;

figure(1); clf;
plot(time,r); xlim([xmin,xmax]);ylim([ymin,ymax]);
set(gca,'fontsize',20);
title('Radial','fontsize',30);
xlabel('Time [s]','fontsize',24);
ylabel('Acceleration [G]','fontsize',24);
saveas(gcf,'C:\Documents and Settings\Zac\My Documents\Research\Shakeandspin...
              \WDPRepeater\Presentations\radialTime.eps');
saveas(gcf,'C:\Documents and Settings\Zac\My Documents\Research\Shakeandspin...
              \WDPRepeater\Presentations\radialTime.emf');

figure(2); clf;
plot(time,t);xlim([xmin,xmax]);ylim([ymin,ymax]);
set(gca,'fontsize',20);
title('Tangential','fontsize',30);
xlabel('Time [s]','fontsize',24);
ylabel('Acceleration [G]','fontsize',24);
saveas(gcf,'C:\Documents and Settings\Zac\My Documents\Research\Shakeandspin...
              \WDPRepeater\Presentations\tangentialTime.eps');
```

```
saveas(gcf,'C:\Documents and Settings\Zac\My Documents\Research\Shakeandspin...
              \WDPRepeater\Presentations\tangentialTime.emf');

figure(3); clf;
plot(time,z); xlim([xmin,xmax]);ylim([ymin,ymax]);
set(gca,'fontsize',20);
title('Axial','fontsize',30);
xlabel('Time [s]','fontsize',24);
ylabel('Acceleration [G]','fontsize',24);
saveas(gcf,'C:\Documents and Settings\Zac\My Documents\Research\Shakeandspin...
              \WDPRepeater\Presentations\axialTime.eps');
saveas(gcf,'C:\Documents and Settings\Zac\My Documents\Research\Shakeandspin...
              \WDPRepeater\Presentations\axialTime.emf');

figure(4); clf;
subplot(1,3,1);
plot(time,r); xlim([xmin,xmax]);ylim([ymin,ymax]);
set(gca,'fontsize',20);
title('Radial','fontsize',30);
xlabel('Time [s]','fontsize',24);
ylabel('Acceleration [G]','fontsize',24);

subplot(1,3,2);
plot(time,t); xlim([xmin,xmax]);ylim([ymin,ymax]);
set(gca,'fontsize',20);
title('Tangential','fontsize',30);
xlabel('Time [s]','fontsize',24);
ylabel('Acceleration [G]','fontsize',24);

subplot(1,3,3);
```

```
plot(time,z); xlim([xmin,xmax]);ylim([ymin,ymax]);
set(gca,'fontsize',20);
title('Axial','fontsize',30);
xlabel('Time [s]','fontsize',24);
ylabel('Acceleration [G]','fontsize',24);

saveas(gcf,'C:\Documents and Settings\Zac\My Documents\Research\Shakeandspin...
              \WDPRepeater\Presentations\rawRotated.eps');
saveas(gcf,'C:\Documents and Settings\Zac\My Documents\Research\Shakeandspin...
              \WDPRepeater\Presentations\rawRotated.emf');

end
```

A.3 Matlab Fourier Transform Script

The following is a Matlab script that is used to calculate the Discrete Fourier Transform of the previously rotated acceleration data.

Appendix B

Test Setup

B.1 Actuator Torque Analysis

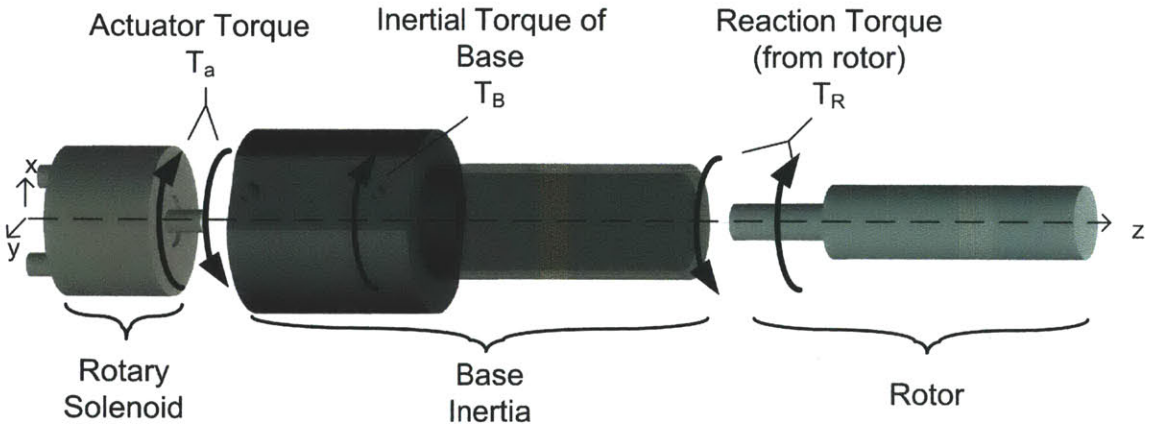

Figure B-1: *Torque analysis of the test setup. The rotary solenoid provides an actuation torque that is resisted by the inertia of the coupling and harvester casing. Additionally, the forces on the rotor inside the harvester apply a reaction torque to the base.*

The actuator torque can be found by summing the torques acting on the base of

the device,

$$\begin{aligned} T_a &= T_B - T_R \\ &= I_{z_B}\ddot{\alpha} + I_{z_R}\left(\ddot{\alpha} + \ddot{\phi}\right) \\ &= \left(I_{z_B} + I_{z_R}\right)\ddot{\alpha} + I_{z_R}\ddot{\phi} \end{aligned}$$

Where from an analysis of the rotor dynamics, in steady-state $\ddot{\phi}$ can be written as,

$$\ddot{\phi} = \frac{r^2}{(1-r^2) + \frac{r}{Q}j}\ddot{\alpha} \tag{B.1}$$

Substituting this result into the actuator torque equation results in an expression for the actuator torque as a function of the desired input acceleration.

$$\begin{aligned} T_a &= \left(I_{z_B} + I_{z_R}\right)\ddot{\alpha} + I_{z_R}\left(\frac{r^2}{(1-r^2) + \frac{r}{Q}j}\ddot{\alpha}\right) \\ &= \underbrace{\left(\underbrace{I_{z_B}}_{1} + \underbrace{I_{z_R}\left(1 + \frac{r^2}{(1-r^2) + \frac{r}{Q}j}\right)}_{2}\right)}_{\text{Equivalent Inertia}}\ddot{\alpha} \end{aligned}$$

From the perspective of the actuator, the test setup looks like an equivalent inertia that must be accelerated by the desired amount $\ddot{\alpha}$. The equivalent inertia consists of two components, the first component is the fixed or rigid inertia of the system and the second is the dynamic forces of the rotor.

Assume a harmonic acceleration input,

$$\ddot{\alpha} = A\cos(\omega t) = \Re\left[Ae^{j\omega t}\right]$$

In addition to analytic simplicity, a harmonic input is a good upper bound for the actuator torque. The purely inertial component is only dependent on the acceleration amplitude so a harmonic input of the same maximum amplitude of a random or wide-band input. The rotor dynamics component is a maximum at resonance, so

a harmonic input will require a larger torque than a random or wide-band input that does not induce resonance. Since the components of the torques are at different phases, is is possible that the torque required at by a random signal might require more torque at an off resonance frequency than a harmonic input. However, the harmonic input provides a reasonable upper bound. For the harmonic acceleration input, the actuator torque becomes,

$$
\begin{aligned}
T_a &= \Re\left[\underbrace{AI_{z_B}}_{1} e^{j\omega t} + \underbrace{AI_{z_R}\sqrt{\frac{1+\left(\frac{r}{Q}\right)^2}{\left(1-r^2\right)^2+\left(\frac{r}{Q}\right)^2}}\, e^{j(\omega t+\theta_1)}}_{2}\right] \\
&= \Re\left[\underbrace{A\sqrt{\frac{\left[\left(I_{z_B}+I_{z_R}\right)\left(1-r^2\right)+I_{z_R}r\right]^2+\left[\left(I_{z_B}+I_{z_R}\right)\left(\frac{r}{Q}\right)\right]^2}{\left(1-r^2\right)^2+\left(\frac{r}{Q}\right)^2}}\, e^{j(\omega t+\theta_2)}}_{3}\right] \qquad \text{(B.2)}
\end{aligned}
$$

The first quantity is the amplitude of the torque caused by the rigid inertia of the test set up. The second quantity is the amplitude of the torque caused by the dynamic forces of the rotor, and the third quantity is the amplitude of the torque cause by both simultaneously. Note because of the phase component, the total torque is not the sum of the individual torques. The values of I_{z_B} and I_{z_R} are calculated by ProEngineer and listed in Tab. B.1. The acceleration amplitude is determined by assuming an acceleration amplitude similar to that provided by the gyro data show in Fig. B-2. Although the harmonic components are only $5-10\ rad/s^2$, as mentioned previously the inertial components are dependent only on the total amplitude of acceleration which can be seen from the time plot to be approximately $100\ rad/s^2$. Since the goal is to get a good upper bound, an amplitude of $100\ rad/s^2$ is chosen.

Figure B-3 is a plot of the three torque components as a function of the frequency ratio. When the harvester is at resonance the rotor torque dominates. To help reduce the feed back of the harvester to the rotary solenoid the frequency invariant inertial

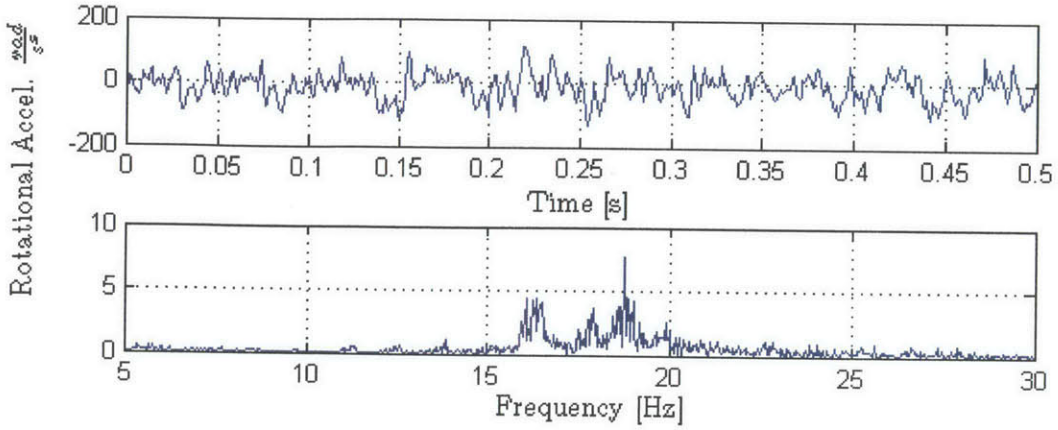

Figure B-2: *Plot of an example acceleration input. The data is measured with a velocity gyro and numerically differentiated in Matlab to obtain the acceleration. The data is collected over approximately 900s. The top plot is a small window of the rotational acceleration $\ddot{\alpha}$ as a function of time. The bottom plot is a DFFT in Matlab of the entire data run.*

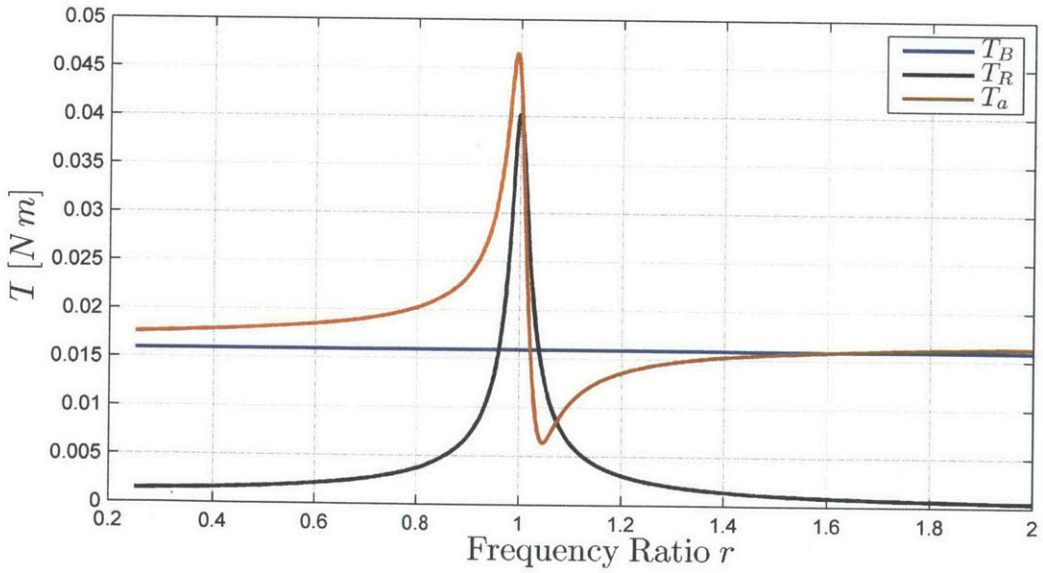

Figure B-3: *Torque components*

torque should be at least an order of magnitude greater than the frequency dependent rotor torque. To determine how much rigid inertia must be added to the base in order to produce an order of magnitude more torque, start by defining the torque ratio x as the ratio of inertial to rotor torques.

$$x|_{r=1} = \frac{I_{z_B} + I_{\text{added}}}{I_{z_R}\sqrt{1+Q^2}}$$

Where the rotor torque as been evaluated at the resonant frequency since this is the critical point. Solving this for the added inertia results in,

$$I_{\text{added}} = xI_{z_R}\sqrt{1+Q^2} - I_{z_B} = 3.86\,X\,10^{-3}$$

The additional inertia is added in the from of an aluminum ring shown in Fig. B-4. The inertia of the ring about the z-axis is,

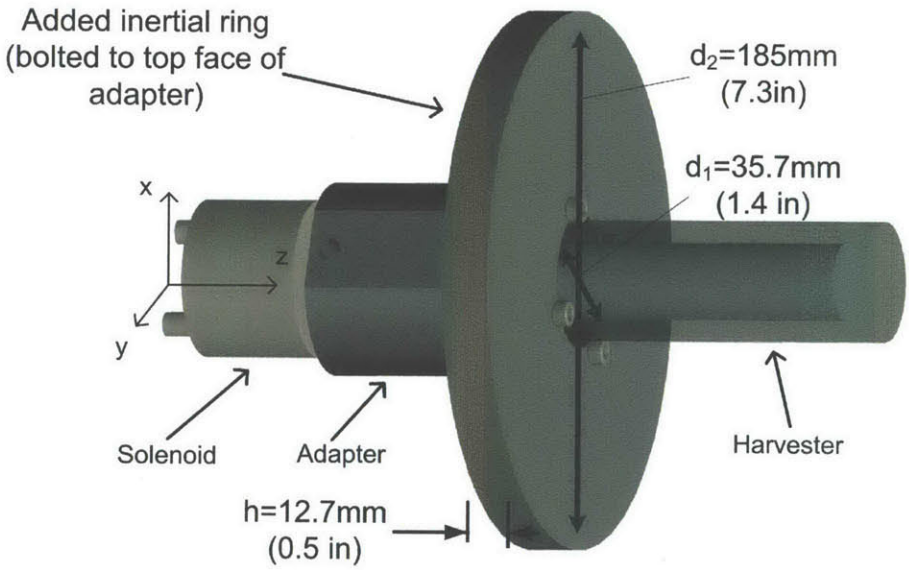

Figure B-4: *Solid model of the test setup with the inertial ring.*

$$I_{z_{\text{added}}} = \frac{1}{2}\pi\rho h\left(\left(\frac{r_2}{2}\right)^4 - \left(\frac{r_1}{2}\right)^4\right)$$

The inner radius of the ring is fixed by the dimensions of the adapter, but the density, thickness and outer radius can all be adjusted to get the needed inertia. A 12.7 mm (0.5 in) thick aluminum ring of outer diameter 185 mm (5.6 in) will provide the necessary inertia. Figure B-5 shows the smoothing effect the added inertia has on the required torque input.

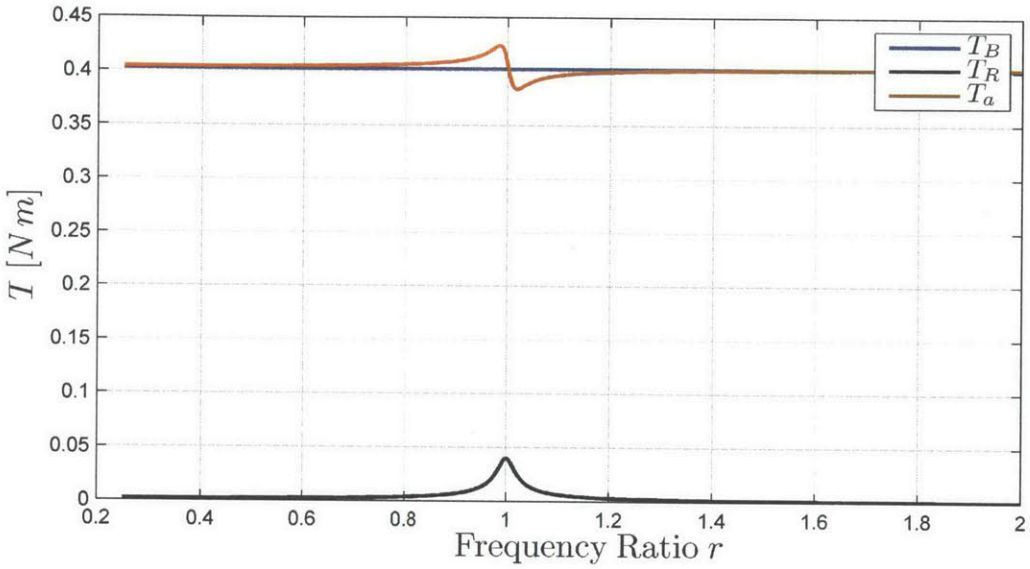

Figure B-5: *Torque components with added inertia*

B.2 Nomenclature

Table B.1: Nomenclature

Variable	Unit	Value	Description
I_{z_B}	$kg\ mm^2$	159	Mass moment of inertia of the base (coupling, inertial ring, and harvester casing) about the longitudinal or z-axis
I_{z_R}	$kg\ mm^2$	13.4	Mass moment of inertia of the harvester rotor about the longitudinal or z-axis
$\ddot{\alpha}$	rad/s^2		Rotational acceleration of the base with respect to ground
$\ddot{\phi}$	rad/s^2		Rotational acceleration of the harvester rotor with respect to the base
r			Frequency ratio defined as the input acceleration frequency divided by the natural frequency of the torsion spring and rotor
Q		30	Quality factor of the torsional spring-rotor inertia-damping system
T_a	$N\ m$		Actuator torque
T_B	$N\ m$		Inertial resistance torque provided by the setup base
T_R	$N\ m$		Dynamic rotor torque feed-back through the base as a result of the rotor motion
A	rad/s^2	100	Harmonic amplitude of $\ddot{\alpha}$
ω	Hz	5-50	Harmonic frequency of $\ddot{\alpha}$
t	s		Time
θ_1	rad		Phase angle of T_R
θ_2	rad		Phase angle of T_a
x		10	Torque ratio T_B/T_R
h	mm	12.7	Thickness of the inertial ring
d_1	mm	35.7	Inner hole diameter of inertial ring
d_2	mm	185	Outer diameter of inertial ring
ρ	kg/m^3	2700	Density of inertial ring
I_{added}	$kg\ mm^2$	3590	Inertia that must be added to require a minimum torque ratio of 10

Appendix C

Additional Acceleration Information

C.1 Raw Data

The raw data was recorded by the engineers at Schlumberger. As best as is understood by the research group, the data was recorded as follows. The prototype repeater housing was mounted to the drilling surface-sub, and the acceleration data in all three axes was recorded using a SaverXware 3Xm 3-axis accelerometer. The accelerometer was mounted in a prototype of the WPD Repeater housing as shown in figure C-1. The acceleration data is then provided in an Excel spreadsheet file. (Reference screen-shot shown in figure C-2) The spreadsheet provides a column of time data and three columns of acceleration values (measured in G) for each of the accelerometer's three channels. The data is recorded at a sampling frequency of $1000Hz$ for a total of $2.05s$. Five separate two second measurements are provided.

Matlab is used to plot the data in figure C-3. (Note: The data must first be read into the Matlab environment, then plotted. The Matlab code used to do this is given in appendix A.1). As can be seen, the average peak acceleration is visually on the order of $1G$ for the *red* channel, $2G$ for the *green* channel, and $4G$ for the *yellow* channel.

To have meaning, the directions of the accelerations must be related to the the

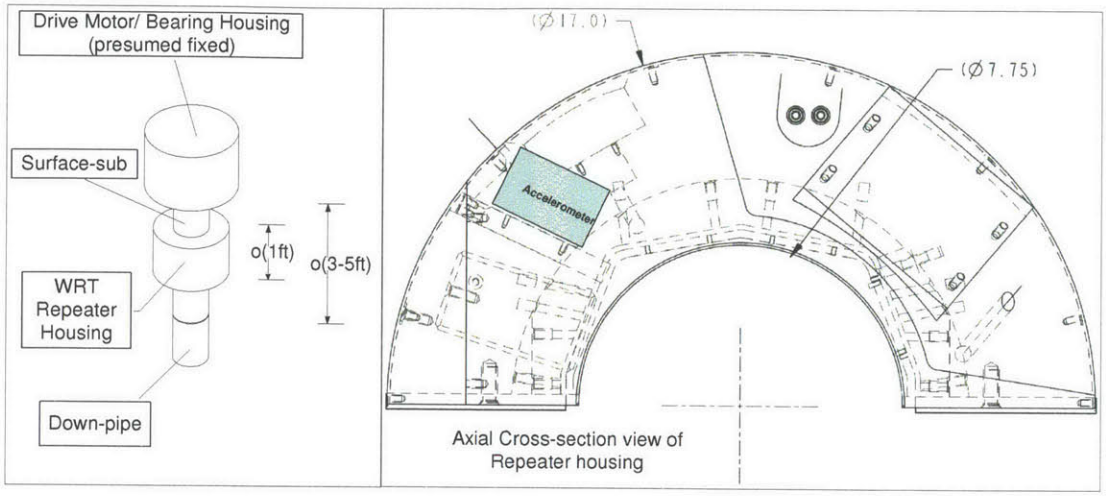

Figure C-1: *Cross-section of the WPD-repeater tool showing the location of the accelerometer.*

F11

	A	B	C	D	E	F	G	H	I	J	K
1	èSaverXware Time Domain Export File										
2	Generated From: C:\Documents and Settings\fbondar\Desktop\VEH\CTF OCT2007 data\PostProcessing\CTF OCT2007 Test Shock Data.SXd.SXe										
3	Event: Timer 822										
4	Active Channel Code: 7										
5	Time (sec)	CH1 Acc (G's)	CH2 Acc (G's)	CH3 Acc (G's)							
6	0.00E+00	-1.04E-01	1.83E-02	-1.29E+00							
7	1.00E-03	-6.10E-02	-2.62E-01	-8.48E-01							
8	2.00E-03	-4.27E-02	-7.81E-01	-2.03E+00							
9	3.00E-03	5.00E-01	-2.81E-01	-2.26E+00							
10	4.00E-03	1.40E-01	-1.59E-01	1.10E-01							
11	5.00E-03	2.32E-01	-3.11E-01	1.69E+00							
12	6.00E-03	7.93E-02	-5.31E-01	9.09E-01							
13	7.00E-03	3.66E-02	-8.12E-01	-2.38E-01							
14	8.00E-03	2.44E-02	7.39E-01	-9.83E-01							
15	9.00E-03	3.42E-01	8.42E-01	-2.75E-01							
16	1.00E-02	2.69E-01	-2.32E-01	9.16E-01							

Figure C-2: *Representative screen-shot of an example Excel spreadsheet file. The data is provided in four columns: one column of time, and three columns of acceleration corresponding to the three acceleration channels labeled by color.*

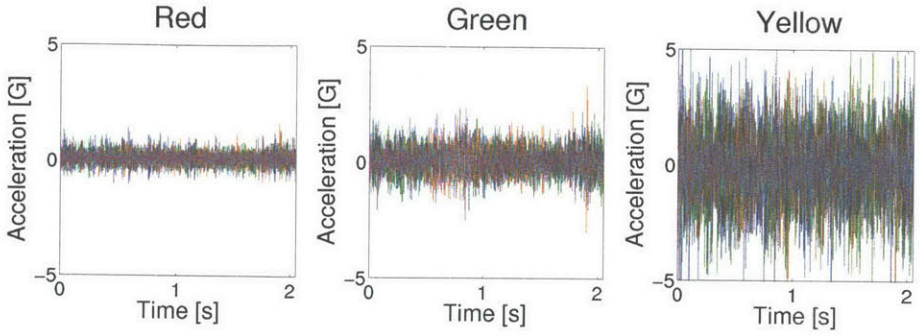

Figure C-3: *Plot of the measured acceleration as a function of time. Each of the plots contains five separate traces corresponding to the five individual trials. Also note, all of the plots are to the same scale so the relative magnitude of each acceleration channel can be compared.*

repeater housing. The directions are inferred from two resources: First, a plot of the normalized power spectral density (PSD) provided with the acceleration data by Schulumberger engineers where the relative directions of each channel are labeled on the plot (figure C-4), and Second, a picture of the SaverXware accelerometer where the channel directions are related to the physical dimension of the accelerometer (figure C-5).

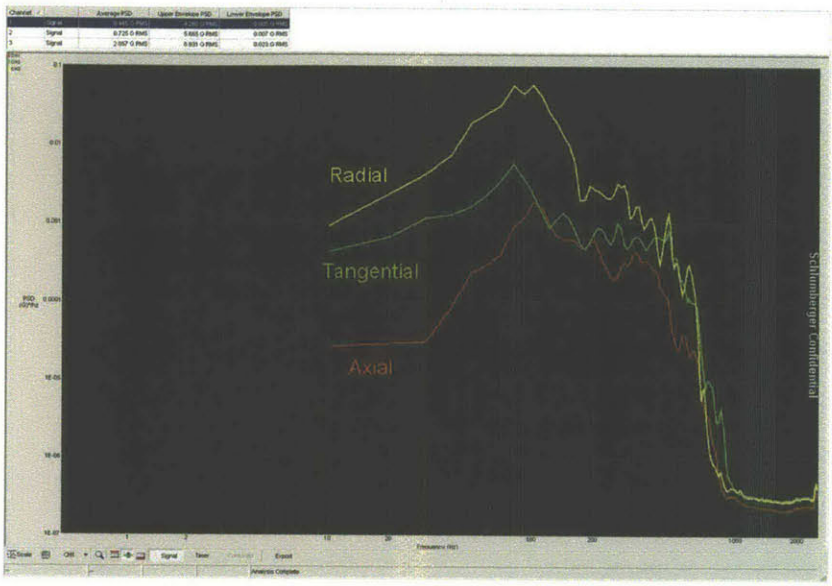

Figure C-4: *Plot of the scaled Power Spectral Density (PSD) of the acceleration data provided by Schlumberger engineers. The PSD is used to infer the directions of the acceleration channels with respect to the surface sub.*

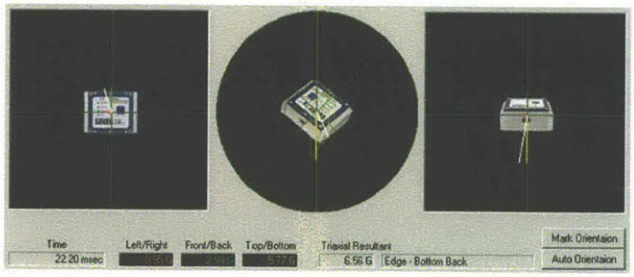

Figure C-5: *SaverXware accelerometer. Notice that the* yellow *channel is measured* Top to Bottom *with respect to the accelerometer where positive is considered downward, and the* green *and* red *channels are measured* Front to Back *and* Left to Right *respectively. Also note that crossing the* green *coordinate into the* yellow *coordinate, the* red *coordinate forms a right-handed coordinate system. (i.e.* (green,yellow,red) *is right handed)*

As seen in figure C-4, the *yellow* direction is labeled as aligned with the *radial* direction, the *green* direction is labeled as aligned with the *tangential* direction, and the *red* direction is labeled as aligned with the *axial* direction. Since the actual sign of the values does not effect the magnitude calculations, the *yellow* and *green* directions can be assumed positive when compared to a typical cylindrical coordinate system, (r, θ, z). Noticing in figure C-5 that the the *(green,yellow,red)* coordinate system is right-handed, the *red* direction must then be positive into the page with respect to the sub cross-section. The inferred coordinates are shown in figure C-6.

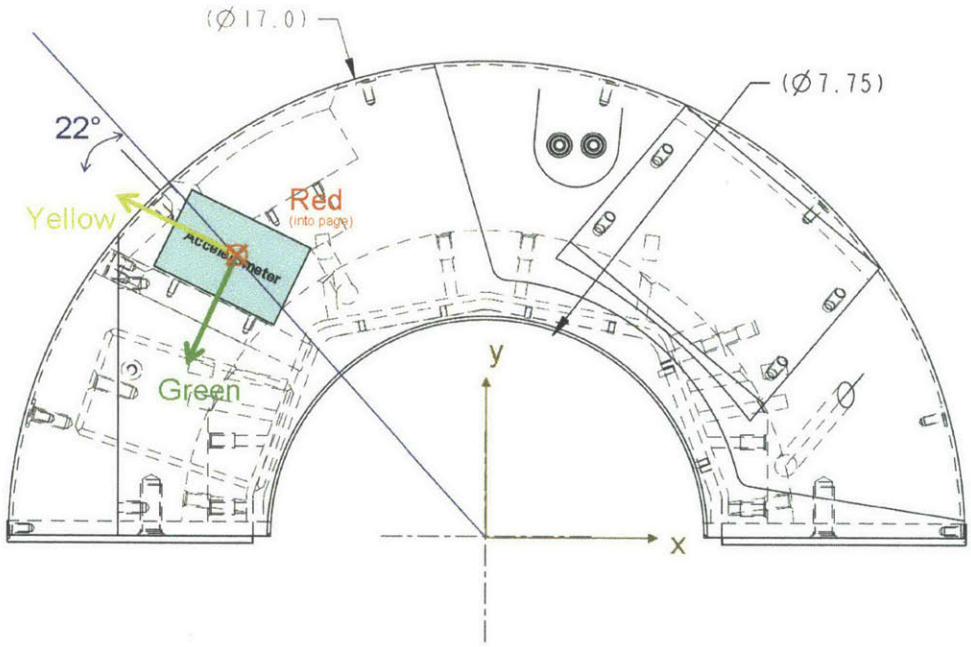

Figure C-6: *Cross-section of the WPD-repeater tool and accelerometer with the inferred accelerometer coordinates, and imposed* (x, y) *coordinates shown. Note, the axes of the accelerometer are not aligned with the standard cylindrical coordinate axes. The accelerometer's axes are all assumed to pass through the center of the accelerometer (assumption assumed valid based on figure C-5) then a line is drawn from the pipe center through the center of the accelerometer, and the angle between the* yellow *axis and the line is measured with a protractor.*

C.2 Rotation of raw data to standard cylindrical coordinates

As can be seen in figure C-6 the axes for the accelerometers are not actually aligned with typical cylindrical coordinates. To help standardize the analysis, the data is transformed into typical (r, θ, z) coordinates. To transform the data, the origins of all three accelerometer axes are assumed to be in the center of the accelerometer. This assumption is assumed valid based on the given representation of the accelerometer (figure C-5). Then, assuming the sub cross-section is drawn to scale, a reference line is electronically drawn in power point from the marked pipe center through the center of the accelerometer. The reference angle is then measured by hand with a protractor. Under these assumptions, the reference angle from the *yellow* direction to the r direction is measured as approximately 22°. Thus, using the standard transformation of coordinates formula,

$$x' = x\cos(\phi) + y\sin(\phi) \tag{C.1}$$

$$y' = -x\sin(\phi) + y\cos(\phi) \tag{C.2}$$

where in this case, x' is the radial coordinate r, x is the *yellow* coordinate, y' is the tangential coordinate θ, y is the *green* coordinate, and the rotation angle ϕ is the negative of the reference angle $-22°$; the radial, tangential, and axial accelerations are given by,

$$A_r = A_{yellow}\cos(-22°) + A_{green}\sin(-22°) \tag{C.3}$$

$$A_\theta = -A_{yellow}\sin(-22°) + A_{green}\cos(-22°) \tag{C.4}$$

$$A_z = A_{red} \tag{C.5}$$

The data is transformed and plotted using Matlab (appendix A.2), and the transformed data is shown in figure C-7.

The visual average magnitude of acceleration is on the order of $3 - 4G$ for the ra-

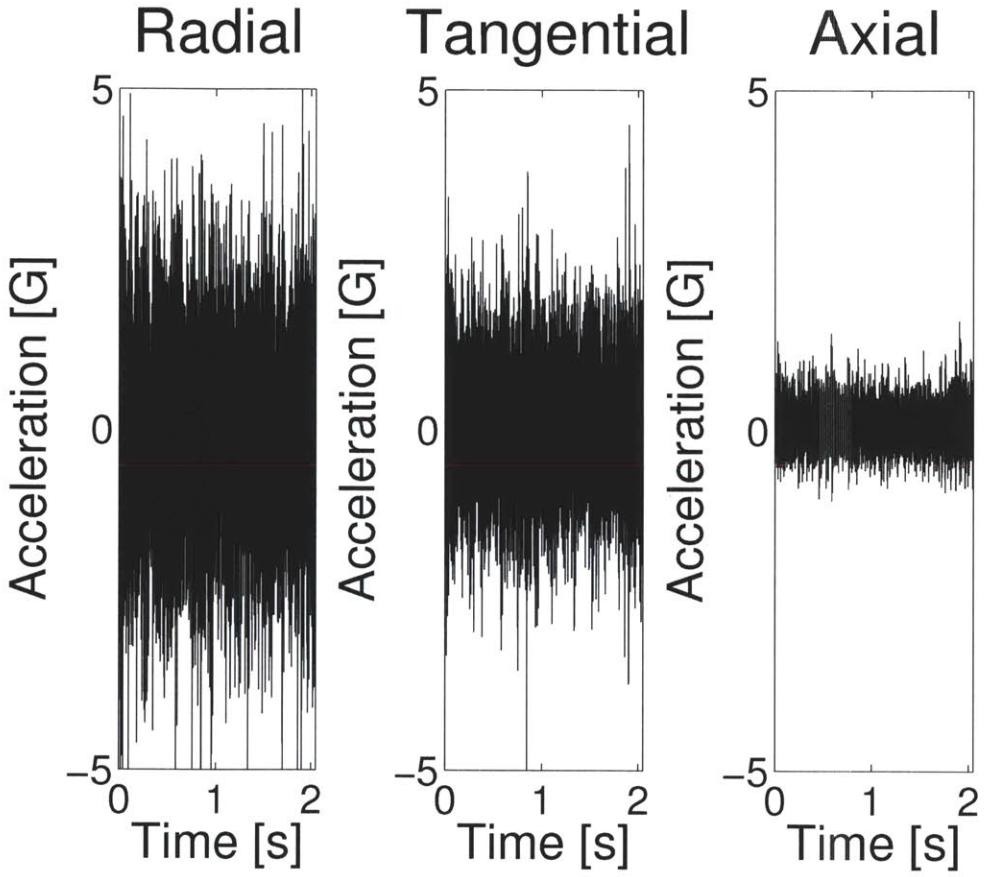

Figure C-7: *Rotated accelerations. Each plot contains five trials and the plots are scaled equally to allow easy comparison of magnitudes*

dial component, $2.5G$ for the tangential component, and $1G$ for the axial component. Ideally, the the tangential acceleration would be the largest component of acceleration since the existing prototype device is designed to harvest primarily tangential accelerations. However, a fourier transform of data is needed to compare the two components on a frequency basis.

Bibliography

[1] www.magnet4less.com NB030 magnet specs (http://www.magnet4less.com/product_info.php?cPath=1_5&products_id=33), 2009.

[2] S.R. Anton and H.A. Sodano. A review of power harvesting using piezoelectric materials (2003–2006). *Smart Materials and Structures*, 16:R1, 2007.

[3] DP Arnold. Review of Microscale Magnetic Power Generation. *Magnetics, IEEE Transactions on*, 43(11):3940–3951, 2007.

[4] Micheal Athans and Peter L. Falb. *Optimal control: an introduction to the theory and its applications.* New York: Dover Publications, 2007.

[5] V. Berbyuk and J. Sodhani. Towards modelling and design of magnetostrictive electric generators. *Computers & Structures*, 86(3-5):307–313, 2008.

[6] Raymond Canale P. Chapra, Steven C. *Numerical methods for engineers.* McGraw-Hill New York, 4 edition, 1989.

[7] Henry Edwards and David Penney. *Differential Equations and Boundary Value Problems, Computing and Modeling.* Pearson, 2004.

[8] P. Glynne-Jones, MJ Tudor, SP Beeby, and NM White. An electromagnetic, vibration-powered generator for intelligent sensor systems. *Sensors & Actuators: A. Physical*, 110(1-3):344–349, 2004.

[9] P. Glynne-Jones and NM White. Self-powered systems, a review of energy sources. *Sensor Review*, 21(2):91–97, 2001.

[10] E. Halvorsen. Energy harvesters driven by broadband random vibrations. *Microelectromechanical Systems, Journal of*, 17(5):1061–1071, 2008.

[11] E. Halvorsen, L.C.J. Blystad, S. Husa, and E. Westby. Simulation of electromechanical systems driven by large random vibrations. In *Perspective Technologies and Methods in MEMS Design, 2007. MEMSTECH 2007. International Conference on*, pages 117–122. IEEE, 2007.

[12] J. Huang, R.C. O'Handley, and D. Bono. High efficiency vibration energy harvester, January 10 2006. US Patent 6,984,902.

[13] Daniel J. Inman. *Engineering Vibrations.* Prentice Hall, 2 edition, 2001.

[14] Roësset José Manuel Kausel, Eduardo. Advanced Structural Dynamics, 2001.

[15] H. Kulah and K. Najafi. An electromagnetic micro power generator for low-frequency environmental vibrations. *Micro Electro Mechanical Systems, 2004. 17th IEEE International Conference on.(MEMS)*, pages 237–240, 2004.

[16] K. Lingaiah. *Machine Design Databook.* McGraw-Hill, 2 edition, 2003.

[17] S. Meninger, J.O. Mur-Miranda, R. Amirtharajah, A. Chandrakasan, and J.H. Lang. Vibration-to-electric energy conversion. *Very Large Scale Integration (VLSI) Systems, IEEE Transactions on*, 9(1):64–76, 2001.

[18] PD Mitcheson, TC Green, EM Yeatman, and AS Holmes. Architectures for vibration-driven micropower generators. *Microelectromechanical Systems, Journal of*, 13(3):429–440, 2004.

[19] PD Mitcheson, EK Reilly, T. Toh, PK Wright, and EM Yeatman. Performance limits of the three MEMS inertial energy generator transduction types. *Journal of Micromechanics and Microengineering*, 17:S211, 2007.

[20] S. Roundy. On the effectiveness of vibration-based energy harvesting. *Journal of Intelligent Material Systems and Structures*, 16(10):809, 2005.

[21] S. Roundy, P.K. Wright, and J. Rabaey. A study of low level vibrations as a power source for wireless sensor nodes. *Computer Communications*, 26(11):1131–1144, 2003.

[22] S. Roundy and Y. Zhang. Toward self-tuning adaptive vibration-based micro-generators. In *Proceedings of SPIE*, volume 5649, page 373, 2005.

[23] I. Sari, T. Balkan, and H. Kulah. A Wideband Electromagnetic Micro Power Generator for Wireless Microsystems. *Solid-State Sensors, Actuators and Microsystems Conference, 2007. TRANSDUCERS 2007. International*, pages 275–278, 2007.

[24] I. Sari, T. Balkan, and H. Kulah. An electromagnetic micro power generator for wideband environmental vibrations. *Sensors & Actuators: A. Physical*, 2007.

[25] A.H. Slocum, J.H. Lang, and A.Z. Trimble. Downhole vibration sensing by vibration energy harvesting. 2007.

[26] H.A. Sodano, D.J. Inman, and G. Park. A review of power harvesting from vibration using piezoelectric materials. *Shock and Vibration Digest*, 36(3):197–206, 2004.

[27] MSM Soliman, EM Abdel-Rahman, EF El-Saadany, and RR Mansour. A wide-band vibration-based energy harvester. *Journal of Micromechanics and Microengineering*, 18(11):115021, 2008.

[28] L. Wang and FG Yuan. Energy harvesting by magnetostrictive material (MsM) for powering wireless sensors in SHM. In *SPIE Smart Structures and Materials & NDE and Health Monitoring, 14th International Symposium (SSN07)*, pages 18–22. Citeseer, 2007.

[29] L. Wang and FG Yuan. Vibration energy harvesting by magnetostrictive material. *Smart Materials and Structures*, 17:045009, 2008.

[30] CB Williams and R.B. Yates. Analysis of a micro-electric generator for microsystems. *Sensors and Actuators A: Physical*, 52(1-3):8–11, 1996.

[31] EM Yeatman. Energy harvesting from motion using rotating and gyroscopic proof masses. *Proceedings of the Institution of Mechanical Engineers, Part C: Journal of Mechanical Engineering Science*, 222(1):27–36, 2008.

[32] M. Zahn. *Electromagnetic Field Theory: a problem solving approach.* Wiley, 1979.